Weak Ligand-Protein Interactions Studied Using Electrospray Ionization Mass Spectrometry

by

Erick Gabriel Baez Bolivar

A thesis submitted in partial fulfillment of the requirements for the degree of

Master of Science

Department of Chemistry
University of Alberta

© Erick Gabriel Baez Bolivar, 2021

Abstract

This thesis focuses on the development and application of electrospray ionization mass spectrometry (ESI-MS) based methods for the direct quantification and characterization of low affinity interactions between carbohydrates (glycans) and glycan binding proteins (GBPs) using nanoflow ESI emitters, from now on submicron emitters.

The affinities of most monovalent glycan–GBP complexes are typically weak (dissociation constant (K_d) >μM) and difficult to reliably measure with conventional assays; consequently, the glycan specificities of most GBPs are not well established. Here, we demonstrate how ESI-MS, implemented with submicron emitters with inner diameters of ~50 nm, allows for the facile quantification of low affinity glycan-GBP interactions. The small size of the droplets produced from these submicron emitters effectively eliminates the formation of non-specific glycan–GBP binding (false positives) during the ESI process up to ~mM glycan concentrations. Thus, interactions with affinities as low as ~5 mM can be measured directly from the mass spectrum. The general suppression of non-specific adducts (including non-volatile buffers and salts) achieved with these tips enables ESI-MS glycan affinity measurements to be performed on C-type lectins, a class of GBPs that bind glycans in a calcium dependent manner and are important regulators of immune response. At physiologically-relevant calcium ion concentrations (2 mM – 3 mM), the extent of Ca^{2+} non-specific adduct formation observed using the submicron emitters is dramatically suppressed, allowing glycan affinities, and the influence of Ca^{2+} thereon, to be measured. Moreover, we demonstrated how the use of submicron emitters and suppression of non-specific binding enable the quantification of labile (prone to in-source dissociation) glycan–GBP interactions.

On the other hand, the implementation of an enzyme-aided ESI-MS-based strategy for

the quantification of α2,3-Neu5Ac on PSA is described. The strategy takes advantage of time-resolved data collection by ESI-MS to calculate the relative abundances of asialo-PSA, monosialo-PSA and PSA during the reaction period. When reaction progress reaches a plateau, the relative abundance of asialo-PSA yields information about the content of α2,3-Neu5Ac-linked to PSA that was initially incorporated on the glycoprotein. Neuraminidase S (NeuS) was demonstrated to be an enzyme that specifically cleaves α2,3-linked Neu5Ac. The reliability of the method for the quantification of α2,3-Neu5Ac-linked to PSA was validated using an internal standard (Neu5Ac-$^{13}C_3$). Also, a purification method was developed for the extraction and concentration of PSA from blood serum. Yet, a limit of quantification (LOQ) experiment using female blood serum with no detectable PSA levels must be carried out to assess the PSA amount in real samples that this approach is capable of extracting and analyzing. This is a requirement to explore the application of this strategy for clinical purposes.

Preface

The research work presented in Chapter 2 of this thesis has been published as: Báez B., E. G.; Bui, D. T.; Kitova, E. N.; Han, L.; Zheng, R. B.; Luber, E. J.; Sayed, S. Y.; Mahal, L. K.; Klassen, J. S. Submicron Emitters Enable Reliable Quantification of Weak Protein-Glycan Interactions by ESI-MS. Anal. Chem. 2021, 93, 4231-4239. I was responsible for the design of the submicron emitters, data acquisition, data processing and manuscript preparation. Duong T. Bui performed the binding affinity measurements between calcium ions and DC-SIGN, and hGal-3C and lactose, data analysis for those experiments and assisted with the composition of the manuscript. Elena N. Kitova contributed to the data analysis for the quantification of the interaction between calcium ions and dendritic cell-specific intercellular adhesion molecule-3-grabbing non-integrin (DC-SIGN). Ling Han contributed to the data analysis for the quantification of the interaction between calcium ions and DC-SIGN, and ran the ITC experiment for the quantification of the interaction between Lysozyme and L1. Erik J. Luber executed the experiments to measure the internal diameter of the submicron emitters. Sayed Y. Sayed executed the experiments to measure the internal diameter of the submicron emitters. Lara K. Mahal assisted with the manuscript edits. John S. Klassen was the supervisory author.

Chapter 3 includes preliminary data of an on-going project. I was responsible for designing part of the experiments, co-executing experiments, data processing and manuscript prepartion. Duong T. Bui ran the N-glycan analysis. Zhixiong Li designed and performed the experiments to obtain the progress curves.

Chapter 4 collects the conclusions of the body of work discussed in Chapter 2 and Chapter 3.

Acknowledgement

I want to thank Prof. John S. Klassen for giving me the opportunity to form part of an excellent community of professionals. I definitely take with me his passion for contributing with science, the rigurosity with which he approaches each project and his willingness to lead by example. I would like to extend my gratitude to Dr. Elena N. Kitova, Dr. Heajin Park, Dr. Pavel I. Kitov and Dr. Ling Han for their technical advices. I am grateful for the time spent by Prof. Liang Li, Prof. Robert. E. Campbell, Prof. Matthew Macauley and Prof. James Harynuk communicating their passion in their research fields through their lectures.

I would also like to thank Prof. Christopher Cairo, Prof. James Harynuk, Prof. Liang Li, Prof. Jillian M. Buriak and Dr. Yoram Apelblat for their career advices, I really appreciate you took the time to go over my annual progress report and show willingness to help me out when needed. I also want to give special thanks to Ruixiang B. Zheng, Gareth Lambkin and Jing Zheng for their technical support and practical advices, always with joy. I want to acknowledge the financial support from the Department of Chemistry, University of Alberta.

I cannot leave out of this acknowledgement my dear friends Zhixiong Li and Linh Nguyen, they make the lab much more amenable. It was a great pleasure to work with you. Humor, curiosity and a relentless hard work ethic are things I will always bring with me. I also had the opportunity to work with excellent colleagues such as Jianing Li, Yilin Wang, Doung T. Bui, Erik. J. Luber, I wish you all the best in your careers.

Finally, I am thankful I could count with the friendship of Lorie L. Courtnage, she and her family opened their doors to me kindly and greatly contributed to make this possible. This achievement, which is part of my journey, would not have been possible without my family, they are and have always been a great motivation to me.

Table of Contents

Chapter 1 Characterization of Glycan-GBP Interactions Using Electrospray Ionization Mass spectrometry

1.1 Introduction 1

1.2 Electrospray Ionization (ESI) Mass Spectrometry 6

1.2.1 Electrospray ionization 6

1.2.2 MS instrumentation 10

1.2.2.1 Quadrupole 9

1.2.2.2 Orbitrap mass spectrometer 13

1.3 ESI-MS based assay 18

1.3.1 Direct ESI-MS assay 18

1.4 Potential pitfalls of ESI-MS assays 19

1.4.1 In-source dissociation 19

1.4.2 Non-uniform response factors 20

1.4.3 Non-specific binding 20

1.5 The Present Work 22

1.6 References 24

Chapter 2 Submicron Emitters Enable Reliable Quantification of Weak Protein-Glycan Interactions by ESI-MS

2.1 Introduction 33

2.2 Experimental 37

2.2.1 Materials 37

2.2.1.1 Carbohydrates 37

2.2.1.2 Proteins 38

2.2.1.3 Preparation of DC-SIGN CRD 38

2.2.2 Methods 39

2.2.2.1 Mass Spectrometry 39

2.2.2.2 Isothermal Titration Calorimetry 40
2.3 Analysis of ESI-MS binding data 40
2.3.1 Affinity measurements 40
2.3.1.1 Lyz-L1 40
2.3.1.2 P_2^{Saga}-L2 41
2.3.1.3 CRD-Ca^{2+} 42
2.3.1.4 CRD-L3 43
2.3.1.5 hGal-3C-L4 43
2.3.2 Correction for non-specific binding 44
2.4 Results and Discussion 45
2.4.1 Submicron emitters: dimensions and performance 45
2.4.2 L1-Lyz 47
2.4.3 P_2^{Saga}-L2 53
2.4.4 DC-SIGN CRD 57
2.4.4.1 Ca^{2+} binding to DC-SIGN CRD 58
2.4.4.2 L3-CRD 64
2.4.5 Quantifying labile GBP–glycan complexes 67
2.5 Conclusions 71
2.6 References 73

Chapter 3 Time-resolved neuraminidase-aided ESI approach for the relative quantification of α2,3-N-acetylneuraminic acid on PSA

3.1 Introduction 78
3.2 Experimental 84
3.2.1 Materials 84
3.2.1.1 Carbohydrates 84
3.2.1.2 Protein 84

3.2.1.3 (2,3/2,6)-Neu5Ac-linked to PSA 85

3.2.1.4 Removal of N-glycans from PSA 85

3.2.1.5 Extraction of PSA from blood serum 86

3.2.2 Methods 86

3.2.2.1 Mass spectrometry 86

3.2.2.2 Preparation of (2,3/2,6)-Neu5Ac-linked to PSA 87

3.2.2.3 Specificity testing 87

3.2.2.4 N-glycan analysis 88

3.2.2.5 Extraction of PSA from blood serum 88

3.3 Data analysis 89

3.3.1 Progress curves for specificity testing 89

3.3.2 Relative abundances of N-glycans from PSA by HILIC-fluorescence 90

3.3.3 Quantification of α2,3-Neu5Ac on standard PSA using IS 90

3.4 Results and Discussion 91

3.4.1 Specificity of NeuS for α2,3-linked Neu5Ac 91

3.4.2 Glycoforms of PSA (N-glycan analysis) 96

3.4.3 Quantification of the ratio of α2,3-Neu5Ac to α2,6-Neu5Ac on standard PSA 98

3.4.4 Extraction of PSA from blood serum 101

3.5 Conclusions 106

3.6 References 107

Chapter 4 Conclusions

4.1 Conclusions 113

List of References 115

List of Tables

Table 2.1. Summary of types and sizes of submicron emitters reported in literature..... 70

Table 2.2. Summary of dissociation constants (K_d) of GBP-glycan interactions measured by ESI-MS performed using submicron emitters.. 70

Table 3.1. tPSA levels related to medical conditions regarding Prostate Cancer (PCa). This information was extracted from Ref. 10..... 103

Table 3.2. Specificity for α2,3-Neu5Ac-linked PSA of NanB..... 103

Table 3.3. Relative abundance of N-glycan by HILIC-Fluorescence..... 104

Table 3.4. Glycoforms from N-glycans on PSA found by N-glycan analysis. Compositions are given as H_N_S_F_Su: H (Hex, 162.1406 Da), N (HexNAc, 203.1925 Da), S (Sia, 291.2546 Da), F (Fuc, 146.1412 Da) and Su (Sulfur, 32.065 Da). 105

List of Figures

Figure 1.1 Schematic representation of the process of ESI in positive ion mode, adapted from Ref 54.. 7

Figure 1.2 Example of a stationary Taylor cone, adapted from Ref 58.. 9

Figure 1.3 Mechanisms of ion formation in ESI: Ion Evaporation Model (IEM); Charge Residue Model (CRM); Chain Ejection Model (CEM); adapted from Ref 54.. 9

Figure 1.4 Schematic diagram of a cylindrical quadrupole, adapted from Ref 64.. 10

Figure 1.5 The stability diagram of a quadrupole analyzer, adapted from Ref 65.. 10

Figure 1.6 Cartoon representation of an orbitrap mass analyzer, adapted from Ref 66.... 13

Figure 1.7 Orbitrap mass analyzer, adapted from Ref 66.. 13

Figure 1.8 Orbitrap mass analyzer, detection of image current, adapted from Ref 66.. ... 15

Figure 1.9 Representation of the cyclic motions, adapted from Ref 67. 15

Figure 1.10 Schematic diagram of the Thermo Fisher Q Exactive quadrupole-orbitrap mass spectrometer, adapted from Reference 67. 17

Figure 2.1. Structures of the glycan ligands (**L1** – **L4**) used in the present study.. 37

Figure 2.2. Representative HIM images acquired for (a, b) standard and (c, d) submicron emitters. The double headed arrow indicates approximately the position and the diameter of the orifice of the submicron emitters..... 45

Figure 2.3. Titration curve for Lyz (0.18 mM) and **L1** in aqueous ammonium acetate solution (200 mM, pH 7.2 and 25 °C) obtained using ITC 46

Figure 2.4. Representative ESI mass spectra acquired in positive ion mode for aqueous ammonium acetate solutions (200 mM, pH 7.2) of Lyz (5 μM), P_{ref} (1 μM) and **L1** (10 μM, 25 μM, 75 μM, and 150 μM) using (a) submicron and (b) standard emitters. (c) ESI mass spectra acquired for aqueous ammonium acetate solutions (200 mM, pH 7.2) of Lyz (10 μM), **L1** (20 μM) and non-volatile PBS buffer at concentrations of 0.1X, 0.5X, 0.7X and 1X (where 1X PBS corresponds to 137 mM NaCl, 2.7 mM KCl, 10 mM Na_2HPO_4 and 1.8 mM KH_2PO_4). The signal-to-noise ratio (S/N) of the highest intensity signals measured in panels (a) and (b) for the solutions containing 150 μM **L1** are $2x10^4$ and $3x10^3$, respectively. The S/N for the highest intensity peak measured in panel (c) at 0.1X and 1X PBS are 900 and 8, respectively 47

Figure 2.5. Representative ESI mass spectra acquired in positive ion mode for aqueous

ammonium acetate solutions (200 mM, pH 7.2) of Lyz (10 μM), P_{ref} (1 μM) and **L1** at 10 μM; 25 μM; 75 μM; 150 μM, using (a) standard and (b) submicron emitters.. 48

Figure 2.6. Distribution of **L1** bound to Lyz measured by ESI-MS performed in positive ion mode on aqueous ammonium acetate solutions (200 mM, pH 7.2) of Lyz (10 μM), P_{ref} (1 μM) at 10 μM; 25 μM; 75 μM; 150 μM, using (a) standard and (b) submicron emitters The blue bars represent distributions determined directly from the mass spectra; the red bars are the distributions after correction for non-specific binding. The error bars correspond to one standard deviation..... 50

Figure 2.7. Plots of fraction (*F*) of ligand-bound Lyz versus initial **L1** concentration measured for aqueous ammonium acetate solutions (200 mM, pH 7.2) of Lyz (10 μM), P_{ref} (1 μM) and **L1** (10 μM, 15 μM, 20 μM, 25 μM, 50 μM, 75 μM, 100 μM, 125 μM and 150 μM) by ESI-MS performed using (a) submicron and (b) standard nanoESI emitters. The mass spectra acquired using the standard emitters were corrected for non-specific binding using the P_{ref} method (the corrected distributions for $[\mathbf{L1}]_0$ of 10 μM, 25 μM, 75 μM, and 150 μM are shown in Figure 2.6a). The error bars correspond to one standard deviation..... 51

Figure 2.8. Representative ESI-MS spectra acquired in positive ion mode with a standard nanoESI emitter for a 200 mM aqueous ammonium acetate solution (pH 7.2) of Lyz (10 μM) and **L1** (20 μM) in the (a) absence and (b) presence of 1X PBS.. 52

Figure 2.9. Plot of affinity (K_d) of **L1** for Lyz versus PBS concentration. Affinities were measured by ESI-MS performed on aqueous ammonium acetate solutions (200 mM, pH 7.2) of Lyz (10 μM) and **L1** (20 μM) in the presence of PBS (0.1X, 0.5X, 0.7X and 1X), using submicron emitters. Also shown is the K_d measured in the absence of PBS (calculated from data shown in Figure 2.7a). The error bars correspond to one standard deviation.. 53

Figure 2.10. Representative mass spectra acquired in positive ion mode in aqueous ammonium acetate solutions (200 mM, pH 7.4) of P_2^{Saga} (3 μM) and **L2** at 50 μM, 300 μM and 750 μM using (a) submicron and (b) standard emitters..... 55

Figure 2.11. Representative ESI mass spectra acquired in positive ion mode for aqueous ammonium acetate solutions (200 mM, pH 7.4) of P_2^{Saga} (3 μM), P_{ref} (1 μM) and **L2** at

50 μM; 300 μM and 750 μM, using (a) submicron and (b) standard emitters. 56

Figure 2.12. Plots of fraction (*Fs*) of P_2^{Saga} binding sites bound to **L2** versus initial ligand concentration measured by ESI-MS performed on aqueous ammonium acetate solutions (200 mM, pH 7.4) of P_2^{Saga} (3 μM) and **L2** (50 μM, 150 μM, 200 μM, 300 μM, 450 μM, 600 μM, 750 μM) using submicron (red circles) and standard emitters (blue circles). The values acquired with the standard emitters were taken from reference 6 and were corrected for non-specific binding using the P_{ref} method. The error bars correspond to one standard deviation..... 57

Figure 2.13. Representative ESI mass spectra acquired in positive ion mode for aqueous ammonium acetate solutions (200 mM, pH 7.4) of DC-SIGN CRD (3 μM), P_{ref} (2 μM) and $Ca(CH_3COO)_2$ at (a) 0 mM, (b) 0.1 mM, (c) 1 mM, (d) 2 mM and (e) 2.5 mM using submicron tips. Expanded regions of the mass spectra, corresponding to the 8+ charge states of the P_{ref} and CRD ions, are shown in the centre and right panels, respectively.. 59

Figure 2.14. Distributions of Ca^{2+} bound to DC-SIGN CRD measured by ESI-MS performed with submicron emitters on aqueous ammonium acetate solutions (200 mM, pH 7.4) of CRD (3 μM), P_{ref} (2 μM) and $Ca(CH_3COO)_2$ at 0.1 mM; 1.0 mM; 2.0 mM; and 2.5 mM. The corresponding mass spectra are shown in Figure 2.13. The blue bars represent distributions determined directly from the mass spectra; the red bars are the distributions after correction for non-specific binding. The error bars correspond to one standard deviation..... 60

Figure 2.15. Representative ESI mass spectrum acquired with a standard emitter in positive ion mode for an aqueous ammonium acetate solution (200 mM, pH 7.4) of CRD (3 μM), P_{ref} (1.5 μM) and $Ca(CH_3COO)_2$ (2.5 mM). Insets show expanded regions corresponding to the 8+ charge state P_{ref} and CRD ions..... 61

Figure 2.16. Ca^{2+} binding to DC-SIGN CRD. (a) Plot of concentration-dependent fraction (*F*s) of CRD calcium-bound binding sites measured by ESI-MS for aqueous ammonium acetate solutions (200 mM, pH 7.4) of CRD (3 μM) and Ca^{2+} (0.1 – 2.5 mM). Solid curve ($K_{d,intrin}$ of 1.0 mM) represents best fit obtained using Eq. 4. (b) Plot of concentration-dependent fractional abundances of free and Ca^{2+}-bound CRD species measured by ESI-MS (0 Ca^{2+} - red; 1 Ca^{2+} CRD - blue; 2 Ca^{2+} CRD - yellow; 3 Ca^{2+}

CRD - green). The solid curves are the theoretical values expected for three equivalent and independent binding sites and $K_{d,intrin}$ of 1.0 mM. (c) Fractional abundances of free and Ca^{2+}-bound CRD species measured by ESI-MS (blue) and calculated assuming three equivalent and independent binding sites with $K_{d,intrin}$ of 1.0 mM (red). (d) Plot of concentration-dependent fractional abundances of free and Ca^{2+}-bound CRD species measured by ESI-MS. The solid curves are the theoretical values expected for three equivalent (0.84 mM) but dependent binding sites (6 (α) and 0.25 (β)). Error bars correspond to one standard deviation.. 63

Figure 2.17. Representative ESI mass spectra acquired in positive ion mode for aqueous ammonium acetate solutions (200 mM, pH 7.4) of DC-SIGN CRD (1 μM), **L3** (500 μM), P_{ref} (6 μM) and $Ca(CH_3COO)_2$ at (a) 0 mM, (b) 1.0 mM, (c) 2.0 mM, (d) 2.5 mM $Ca(CH_3COO)_2$. (e)-(h) Expanded regions of the mass spectra ((a)-(d)) corresponding to the 8+ charge states of free and **L3**-bound CRD……..65

Figure 2.18. Distributions of Ca^{2+} bound to DC-SIGN CRD-**L3** measured by ESI-MS performed with submicron emitters on aqueous ammonium acetate solutions (200 mM, pH 7.4) of CRD (1 μM), P_{ref} (6 μM), **L3** (500 μM) and $Ca(CH_3COO)_2$ at (a) 1.0 mM, (b) 2.0 mM, (c) 2.5 mM. (a)-(c) distribution of Ca^{2+} bound to CRD; (d)-(f) distribution of Ca^{2+} bound to CRD-**L3**. Blue bars are the distribution before correction for non-specific binding. Red bars are the distribution after correction for non-specific binding. The error bars correspond to one standard deviation. Relative abundances were calculated from the spectra shown in Figure 2.17.. 66

Figure 2.19. Plots of fraction (*F*) of ligand (**L3**)-bound versus initial **L3** concentration measured by ESI-MS performed with submicron emitters on aqueous ammonium acetate solutions (200 mM, pH 7.4) of CRD (1 μM), **L3** (100 - 500 μM) and $Ca(CH_3COO)_2$ (1.0 mM (purple), 2.0 mM (green) and 2.5 mM (blue)). The error bars correspond to one standard deviation.. 67

Figure 2.20. Representative ESI mass spectra acquired with submicron emitters in positive ion mode for aqueous ammonium acetate solutions (200 mM, pH 7.4) of hGal-3C (2 μM), P_{ref} (1.5 μM) and **L4** at (a) 100 μM, (b) 400 μM and (c) 1000 μM.. 68

Figure 2.21. Plot of fraction of ligand (L4)-bound hGal-3C measured by ESI-MS in positive ion mode for 200 mM aqueous ammonium acetate solutions (pH 7.4, 25 ºC) of hGal-3C (2

μM) and L4 (20 μM – 1.0 mM). The red solid circles are the fractional abundances determined directly by ESI-MS; the red solid curve is the best fit of Eq. 16 to these data. The red dashed curve is the expected values calculated using the Kd obtained from the best fit of Eq. 16. 69

Figure 3.1. Schematic representation of an electrochemiluminescence system (ELECSYS) for the quantification of tPSA. The same scheme is used for the quantification of fPSA, but anti-fPSA mAbs are used instead... 79

Figure 3.2. Isomers of Neu5Ac bound to galactose (Gal) or N-acetylgalactosamine (GalNAc) in N-glycans on PSA... 82

Figure 3.3. Structures of the glycans used in the present study.. 85

Figure 3.4. Enzymatic product of NeuS, R represents a glycoconjugate. The chair conformation is adopted in the active site of the enzyme... 92

Figure 3.5. Representative ESI mass spectra of a solution of 20 μM $UniP_{proxy}$, 10 μM CS_{6SL}^{S1}, 10 μM CS_{3SLNAc}^{S2} and 5 μM 2,3-Neu5Ac-linked to PSA in presence of NeuS and 200 mM ammonium acetate at pH 7 and 25 ºC. The spectra were taken at different time points: a) 0-3 min; b) 29-30 min; c) 59-60 min; 239-240 min.... 93

Figure 3.6. Representative ESI mass spectra of a solution of 20 μM $UniP_{proxy}$, 10 μM CS_{6SL}^{S1}, 10 μM CS_{3SLNAc}^{S2} and 5 μM 2,6-Neu5Ac-linked PSA in presence of NeuS and 200 mM ammonium acetate at pH 7 and 25 ºC. The spectra were taken at different time points: a) 0-3 min; b) 29-30 min; c) 59-60 min; 239-240 min.... 95

Figure 3.7. Fractional abundance of PSA_{asialo} from 2,3-Neu5Ac-linked to PSA (black curve) or 2,6-Neu5Ac-linked to PSA (red curve) after treatment with NeuS. Also, the fractional abundances of lactose (green curve) from 6SL and N-acetyllactosamine (orange curve) from 3SLNAc were included. Raw data was taken from Figure 3.5 and Figure 3.6.... 96

Figure 3.8 Deconvoluted chromatogram of N-glycans from PSA a) before treatment with NeuS and; b) after treatment with NeuS..... 97

Figure 3.9 Deconvoluted spectrum of a solution of 5 μM PSA in 200 mM ammonium acetate at pH 7 and 25 ºC. The peaks marked with an asterisk represent the sodium adducts of the ion peak of the glycoform shown at the left of the asterisk. The raw data was deconvoluted using Thermo Scientific Biopharma Finder.. 98

Figure 3.10 Representative ESI mass spectra of a solution of 2 µM PSA and 2.5 µM Neu5Ac-$^{13}C_3$ (**IS**) in presence NeuS into 200 mM ammonium acetate at pH 7 and 25 ºC.. 99

Figure 3.11 a) Progression curves of PSA_{asialo} (red dots) and Neu5Ac (blue dots). b) Fractional abundance of Neu5Ac from N-glycans on PSA and PSA_{asialo}, respectively, from a solution of 2 µM PSA, 2.5 µM Neu5Ac-$^{13}C_3$ (**IS**) in presence of NeuS into 200 mM ammonium acetate at pH 7 and 25 ºC. The experiment was formed using n=3 replicates. 100

Figure 3.12 Representative mass spectra for a solution of a) an aliquot of blood serum from a healthy individual; b) an aliquot of blood serum spiked with PSA to have a final concentration of 10 µM PSA 5 µM PSA, into 200 mM ammonium acetate at pH 7 and 25 ºC. 102

List of Abbreviations

Ab	Abundance of gas-phase ions
AC	Alternating current
CE	Capillary electrophoresis
CEM	Chain injection model
CID	Collision-induced dissociation
CRM	Charged residue model
DC	Direct current
Du	Duty cycle
ER	Endoplasmic reticulum
ESI	Electrospray ionization
FAC-FD	Frontal affinity chromatography using fluorescence detection
GBP	Glycan binding protein
GP	Glycoprotein
HCD	Higher energy collisional dissociation
HILIC	Hydrophilic interaction liquid chromatography
hK3	Human kallikrein 3
HPLC	High-performance liquid chromatography
IAA	Iodoacetamide
IEM	Ion evaporation model
ITC	Isothermal titration calorimetry
K_d	Dissociation constant
L	Ligand
LC	Liquid Chromatography
LIF	Laser-induced fluorescence
m/z	Mass-to-charge ratio
MS	Mass spectrometry

MW	Molecular weight
Neu5Ac	N-acetylneuraminic acid
ND	Not detected
P	Protein
PGC	Porous graphitized carbon chromatography
P_{ref}	Reference protein
PSA	Prostate specific antigen
PTMs	Post-translation modifications
R	Abundance ratio
Res	Resolution
RF	Radio frequency
RF	Response factor
RFU	Relative fluorescence unit
RP	Reversed phase
SRM	Selected Reaction Monitoring
scFv	Single chain variable fragment
SEC	Size exclusion chromatography
SPR	Surface plasmon resonance
SRIG	Stacked ring ion guides
UHMR	Ultra-high mass range

Chapter 1

Characterization of Glycan-GBP Interactions Using Electrospray Ionization Mass spectrometry

1.1 Introduction

Glycans, together with proteins, lipids, and nucleic acids, are one of the four major building blocks in living systems.[1] The heterogeneity of glycans arises primarily from the diversity of monosaccharide structures, sequence and linkage. Glycans form a comprehensive group of biopolymers ranging from monosaccharides to high-molecular weight carbohydrates (polysaccharides) such as starch and cellulose in plants and glycogen in animals.[2] Glycan biosynthesis is exquisitely responsive to the cellular environment because it is not template driven. It depends on multiple interactions resulting from gene expression,[3] substrate availability,[4] cellular environment[5] and the underlying protein structure.[6,7] Glycans also form covalent bonds with other structural entities such as lipids and proteins to make glycolipids and glycoproteins, respectively. This is well-known as glycosylation. Classical types of glycosylation are N- and O-linked (on proteins), glycosphingolipids (on cell-membrane sphingosine), glycosaminoglycans (GAGs) (protein-bound and free) and glycosylphosphatidylinositol (GPI) anchors. The type of glycosylation that is presented at a given glycosylation site is heterogeneous, giving rise in some cases to many glycoforms.[3] Glycans play critical biological roles in modulating structural and functional properties of attached protein and lipids, mediating intrinsic and extrinsic recognition (including signaling, clearance, intercellular and pathogen adhesion) and are involved in many pathophysiological processes.[8] Glycans, naturally existing as monosaccharides, oligosaccharides (short carbohydrate chains), polysaccharides and glycoconjugates (conjugated to lipids and proteins) are mostly found on the cell surface and extracellular matrix (ECM), and also in various organelles such as Golgi, Endoplasmic Reticulum (ER), lysosome, cytosol, and nuclei.[9]

Conjugation of glycans on the surface of proteins has been found to alter the solubility[10], stability[11] and conformation of nascent proteins.[12] Glycans attached to proteins directly participate in numerous physiological and pathological processes through recognition of glycan-binding proteins (GBPs), which mediate various functions including cell-cell communication, host-pathogen and ligand-receptor interactions, signal transduction, macromolecules transport,

and immune response.[9,12,13] Alterations in protein glycosylation are associated with many diseases and can serve as a biomarker and as a contributor to cancer.[14,15,16] Additionally, stability, efficacy and immunogenicity of therapeutic proteins (i.e. antibodies, Fc-fusion proteins) are known to be affected by the glycosylation status, which impacts their pharmacodynamics and pharmacokinetics.[17,18,19] Due to the significant biological roles of glycans conjugated to proteins, a number of analytical methods have been developed to characterize glycoprotein interactions and elucidate the influences of glycans on their binding specificity and affinity.

Isothermal titration calorimetry (ITC) is one of the most widely used techniques to probe protein-carbohydrate and protein-glycoprotein interactions by measuring the change in temperature of a sample cell in comparison with a reference cell due to heat released or absorbed during binding interaction. The output is a plot of heat released or absorbed per second (μcal/s) vs time (min), while the titration curve is obtained by plotting the change of enthalpy (Kcal/mol of ligand) vs molar ratio ([L]/[P]), where L and P are ligand and protein, respectively. The technique also provides thermodynamic information of protein interactions.[20,21] Binding affinity, K_d, binding enthalpy, ΔH, and the binding stoichiometry can be accurately determined from a single experiment. The change of Gibbs free energy of binding, ΔG, can be calculated from K_d and ΔH, and the entropy of binding ΔS can be subsequently obtained. While it is relatively easy to perform, conventional ITC generally requires large amounts of sample (~1 mg of protein) and is a low throughput technique (2-3 hours per titration).[22] The advent of modern ITC, such as Nano ITC (TA instruments) and ITC_{200} (Microcal), has greatly reduced sample consumption by three times and improved throughput (30-40 min per titration), but higher protein concentration (two folds) is needed, which can lead to protein aggregation.[22,23]

Surface Plasmon Resonance (SPR) is another widespread approach for characterizing biomolecular interactions.[24] This technique relies on monitoring the variation of the angle of reflectivity of the incident light induced by binding events in close proximity to a metal layer (typically gold or silver). The variation of the angle of reflectivity is directly proportional to strength of the interaction; the angle is converted into resonance unit (RU) which is then plotted vs time (min) at different concentrations of the analytes, this is called a sensorgram. The titration curve is obtained by plotting the RU at the plateau of each curve vs analyte concentration.

Langmuir binding isotherm is used as a non-linear fitting model for the experimental data.[24] The main advantage of this technique is that the kinetics of association (k_{on}) and dissociation (k_{off}) can be directly calculated from the sensorgram. Thermodynamic parameters, such as ΔG, can be directly calculated from K_d, while ΔH and ΔS can be obtained by performing experiments at different temperatures. In these experiments, ln(K_d) is plotted vs the inverse of the temperature (1/T), the slope represents ΔH and the intercept ΔS. This graph is well-known as Van't Hoff plot. Although SPR offers high sensitivity and relatively low sample consumption (~ng), immobilization of one of the interacting species through coupling (i.e. amine coupling, thiol coupling, aldehyde coupling) might potentially alter the nature of the interactions and ligand affinity.[24,25,26] It is also limited by the diffusion of the analyte from the bulk solution to the surface (mass transport), especially for binding with fast kinetics ($k_{on} > 10^6$ M^{-1} s^{-1} and $k_{off} > 10^{-1}$ M^{-1} s^{-1}).[25,26]

Quartz crystal microbalance (QCM) is another surface sensing method that also monitors changes in mass adsorbed on a surface in real time. The heart of QCM technology is a quartz crystal oscillator, a piezoelectric material.[27] The crystal oscillates at a specific frequency when an appropriate voltage is applied through metal electrodes directly attached to the quartz disc. The frequency of oscillation (*f*) is sensitive to the addition or removal of small amounts of mass at the sensor surface.[28] QCM with dissipation (QCM-D), an extended version of the technique, allows for applications of this technology in liquid media.[29,30] The titration curve is similar to SPR, except that the change of frequency at the plateau for each ligand concentration is plotted vs receptor concentration.[31] In contrast with SPR which is considered an optical or "non-hydrated" technique, QCM-D is referred to as acoustic or "hydrated" technique.[28] In practice, this means that in SPR the protein film (e.g. hydration shell) is essentially not included in the mass determination.[30] Instead, QCM-D senses both the macromolecules and the solvent to measure macromolecular reorganization and conformational changes due to changes in water content.[30] A limitation of this technique is the use of higher sample cell volumes in comparison with SPR, this might introduce mass effects for binding with fast kinetics.[28]

Analytical ultracentrifugation (AUC) is a method based on mass and gravity, where sedimentation is used to analyze the protein behavior in a series of ligand concentrations to

calculate binding affinities. Two experiments are usually designed to extract information from this technique. Sedimentation velocity (SV) measures the rate at which molecules move in response to centrifugal force, providing hydrodynamics about size and shape, as well binding affinities. Whereas for sedimentation equilibrium (SE), the final equilibrium distribution is examined, providing association constants and stoichiometry.[28,32,33] AUC uses ultracentrifuges for high-speed centrifugation, typically ranging from 200000g to 1000000g. The machine uses optic sensors to monitor protein sedimentation over time,[28] the complex (ligand-protein) has a larger mass than free species in solutions, therefore, it sediments faster. A two-sector cell is filled with buffer (as a reference) and with the sample cell containing the ligand-protein mixture. Sedimentation starts upon high-speed centrifugation and the detector keeps monitoring it during the course of the experiment, typically 16 h.[28] In an SV experiment, binding affinities can be calculated using a titration curve where average-weight sedimentation coefficient is plotted vs molar ratio.[33] The main limitations of this technique are the larger amount of sample required (e.g. mg of protein), the expensive equipment and the high expertise require to analyze the data.[28,34]

Radioligand binding assay is a very sensitive method that allows the measurement of affinities in the mM range. Currently, radioligand binding assays are mainly used for membrane-bound receptors.[35,36] There are three experimental types of radioligand binding assays; competitive binding assay, saturation assay, and kinetic binding assay.[37] Competitive assays analyze the equilibrium binding at a fixed concentration of the radioligand and in the presence of different concentrations of an unlabeled competitor. In contrast, in a saturation experiment, a fixed concentration of the receptor is incubated with increasing concentrations of the radioligand to calculate the dissociation constant (K_d). Kinetic assays are used to determine receptor/ligand specific association and dissociation constants, from which a K_d can be derived.[37] The main drawback of this technique is the use of radioactive material, which besides being hazardous requires a specialized facility and licensing.[28]

NMR spectroscopy is a well-known technique for studying intermolecular interactions in the mM range.[38,39] Protein-ligand complexes are studied using the so-called protein-observed and ligand-observed NMR approaches, in which the NMR parameters of the free and bound

molecules are compared.[40,41] In protein-observed methods, a spectrum of the receptor is acquired and the ligand is titrated. This provides information about the receptor residues involved in the direct interaction with the ligand, allowing for the mapping of the ligand binding site. The major drawbacks of these protein-observed methods are the experimental time (e.g. 40 min) and the need for highly stable and soluble receptor proteins. Hence, these methods are limited to proteins with low molecular mass (~30-50 kD) due to solubility issues with high MW proteins in aqueous solutions. Moreover, these methods require protein isotope-labeling strategies and sequence resonance assignments.[40,41] Conversely, in ligand-observed methods, a spectrum of the ligand is acquired and the receptor protein is added. In contrast with protein-observed methods, these experiments offer more sensitivity with larger proteins and require less protein sample without labeling. Ligand-observed methods can be used for the detection of specific interactions and the measurement of protein-ligand affinities, and they can also provide useful structural information on the receptor-ligand complex.[28]

Hydrogen deuterium exchange mass spectrometry (HDX-MS) can provide insights into protein dynamics, protein folding, protein-protein interactions, and protein-small molecule (ligand) interactions. HDX-MS measures changes in mass linked with the deuterium exchange between amide hydrogens of the protein backbone and its surrounding solvent.[42] An HDX-MS experiment is divided into three main steps; deuterium incorporation, spatial localization of deuterium incorporation/exchange, and data analysis. Deuterium labeling can be carried out in a simple exchange reaction, where deuterium is incorporated through incubation of the protein with deuterated buffer. To study ligand-protein interactions, the protein of interest is incubated with the ligand(s) and the hydrogen/deuterium exchange can be spatially resolved using different techniques (e.g. bottom-up and top down HDX-MS approaches).[42,43,44] The K_d can be calculated using a plot of the percentage deuterium found at different concentration of the ligand vs the molar ratio.[28] This method requires low amounts of sample (nM to μM concentration of ligand), and it can be used to study potential conformational changes upon ligand binding and to identify the binding site.[44] However, data analysis and interpretation require expertise.[42,43]

Electrospray ionization mass spectrometry (ESI-MS) represents a powerful tool for identification and quantification of protein-ligand, protein-carbohydrate and other non-covalent

interactions in vitro.[45,46,47,48,49] It relies on detecting noncovalent interactions transferred from solution to the gas-phase through the ESI process without labelling or immobilization.[46] Binding stoichiometry can be established and multiple binding equilibria as well as K_d values in the range of nm-μM range can be determined simultaneously.[49] Typically, less than a minute is needed for acquiring a mass spectrum with less than fmol of sample consumption per analysis. Moreover, this assay can be applied to the screening of carbohydrate libraries[48,50] against proteins and characterization of glycan-mediated interactions between GBP and glycoproteins.[51] Most importantly, binding affinities measured by ESI-MS are in good agreement with values obtained by other binding methods.[52,53] However, as reliable detection and measurements are based on the underlying assumption that protein-complex ions detected in the gas-phase represent their solution states, limitations also exist in ESI-MS assays. Before presenting the work in this thesis, an overview of basic principles of ESI, followed by the MS instrumentation, and potential limitations of ESI, are given below.

1.2 Electrospray Ionization (ESI) Mass Spectrometry

1.2.1 Electrospray ionization

ESI is a soft (with little or no fragmentation) ionization technique where ions are transferred from solution to the gas-phase at atmospheric pressure. It enables the detection of non-volatile biomolecules (such as peptides, proteins and polymers) with low sample consumption (typically 1-10 μM) and expands the mass range by the formation of multiply charged ions, which also enhances the dissociation efficiency in tandem MS.[54]

In a conventional ESI device a metal capillary, a glass-metal coated capillary (generally gold) or a glass capillary is used to carry an electrolyte solution with the analyte.[55] In case of a glass capillary, a platinum wire is inserted into the capillary with the analyte solution. A high electric potential around ±0.5-3 kV is applied to the solution, the mass spectrometer and the capillary can interchangeably be the cathode or anode, depending if positive or negative ion mode is operating.[49,55] For the purpose of this chapter, the principle of ESI will be explained considering positive ion mode which is the most common mode for peptides and proteins ionization in ESI (see Fig. 1.1). The mass spectrometer is the cathode while the capillary is the anode. Under an electric field of ~10^6 V/m [56], charges are separated in the analyte solution, the

capillary has a tip with diameter between 1-5 μm where the solution can escape due to the influence of the electric force. At the tip of the capillary a cone is formed due to the electric field strength, which is commonly known as Taylor cone[57,58], the increase of the surface due to cone formation is resisted by the surface tension of the liquid (see Figure 1.2). As soon as the electric force surmounts the surface tension of the solution, a fine jet emerges from the cone tip. The surface of the jet is charged with an excess of positive charges. The repulsion between the charges on the jet causes the jet to break up into small charged droplets. Shrinkage of the droplets initially of micrometer in diameter occurs as a result of solvent evaporation. As the surface area/volume ratio of the droplets increases, Rayleigh limit Q_{Ry} (shown in Eq.1.1), where electrostatic repulsion is balanced by the surface tension, is reached.[54,55] At or around 10-20% below the Rayleigh limit, surface tension is overcome by Coulombic repulsion, and these droplets become parent droplets and eject numerous smaller droplets (offspring droplets) carrying off 2-5% of their mass and 5-20% of their charge during each cycle of this process, until radii are decreased to a few nanometers.

$$Z_R = \frac{8\pi}{e}\sqrt{\varepsilon_0 \gamma R_d^3} \qquad \text{Eq, 1.1}$$

where Z_R is the charge on the droplet, ε_0 is the vacuum permittivity, γ is the surface tension of solvent, and R_d is the radius of the droplet.

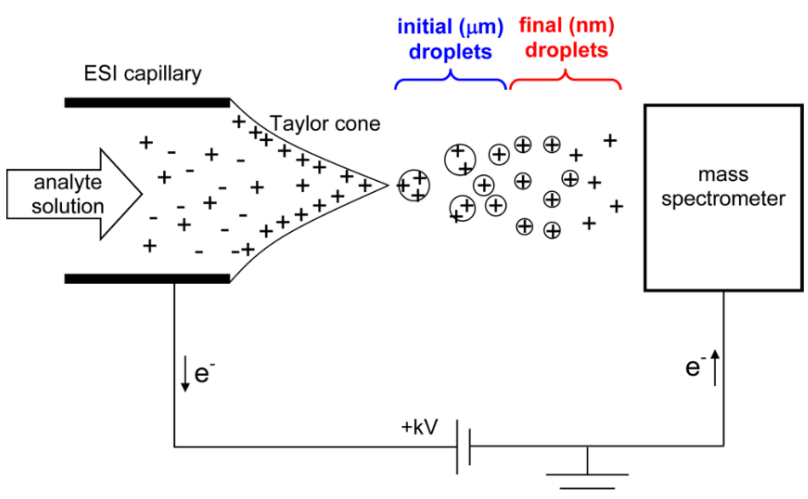

Figure 1.1 Schematic representation of the process of ESI in positive ion mode, adapted from Ref 54.

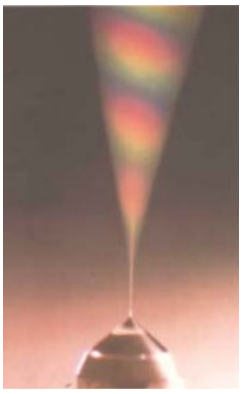

Figure 1.2 Example of a stationary Taylor cone, adapted from Ref 58.

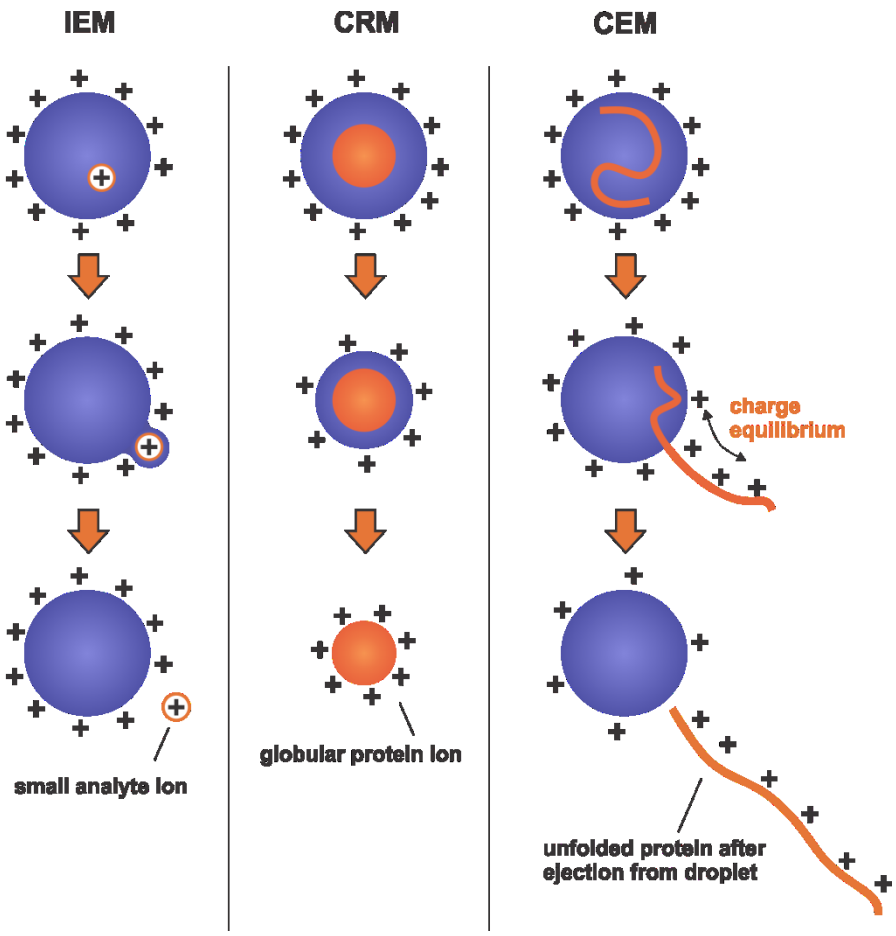

Figure 1.3 Mechanisms of ion formation in ESI: Ion Evaporation Model (IEM); Charge Residue Model (CRM); Chain Ejection Model (CEM); adapted from Ref 54.

Three mechanisms (as shown in Figure 1.3) have been proposed to illustrate the mechanisms of analyte ionization in ESI. First, the ion evaporation model (IEM) explains the ionization of ionic species in the analyte solution such metal ions (e.g. Na^+, K^+, Ca^{2+}). When droplets shrink to around 10 nm in diameter by solvent evaporation and fission due to electrostatic repulsion, a strong electric field compensates for the ionic solvation energies. As a result solvated ions are ejected directly from the surface of the droplets.[59,60] Secondly, the charged residue model (CRM) explains the ionization of biomolecules in their native conformation. As solvent evaporates and undergoes successive fission cycles until the last hydration shell evaporates, the charges in the surface of the droplet are transferred to the analyte. The transfer of charges will depend on the gas phase basicity of the analyte. For example, proteins in general will be easily protonated because they have basic residues with relatively high gas-phase basicities.[55] This explains the relatively high charged state of analytes ionized under this mechanism in comparison with IEM where the ions are ejected before droplet evaporation. Protonation state of analyte in this process, independent of the physicochemical properties of the ion, is determined by the Rayleigh stability limit of droplets which is related to their surface area (the nature of the solvent). Comparison of calculated charge states using the Rayleigh equation and experimental charge states of globular proteins observed in ESI further supports the CRM theory for large globular species.[54,55] Third, unfolded proteins, resulted from denaturation (e.g. elevated temperature, pH changes, disulfide disruption), mutation or absence of cofactor, typically exhibit higher charge distribution than natively folded proteins.[54] Chain ejection model (CEM) has been proposed to account for this behavior, which was demonstrated by molecular dynamics (MD) simulations.[61,62] In this model, the interior hydrophobic residues of proteins, exposed to the hydrophilic solvent due to protein unfolding, are gradually expelled and experience proton equilibration with the highly charged droplets, and are finally ejected as highly charged unfolded gas phase ions before droplet evaporation.[54,63]

1.2.2 MS instrumentation

1.2.2.1 Quadrupole

Quadrupole mass analyzer comprises four parallel rod electrodes with hyperbolic or circular cross-sections extending in the z direction. Ions focused at the entrance of the quadrupole experience a time-dependent (direct current (DC)) and a time-independent (alternating current (AC)) potential applied on the rods and are attracted or repulsed periodically. For a quadrupole mass analyzer the potential distribution Φ at time *t* can be described by Eq. 1.2.

$$\phi_{(x,y)} = [U + V\cos(\omega t)]\frac{x^2 - y^2}{2r_{0^2}} \qquad \text{Eq, 1.2}$$

where ϕ is the potential distribution, *x* and y are coordinates along the x and y axis, *U* and *V* are the magnitudes of a DC and a radiofrequency (RF), ω is the angular frequency, and r_o is the distance from the center (z axis) to the inner surface of an electrode. Electrodes along the X axis are held at potentials of the same amplitude but opposite in sign as the electrodes along the Y axis (see Figure 1.4).[64]

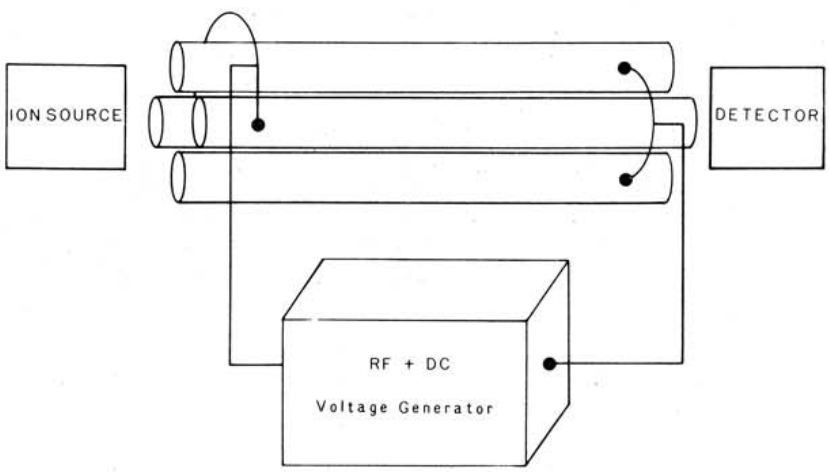

Figure 1.4 Schematic diagrams of cross-sections of a cylindrical quadrupole, adapted from Ref 64.

According to Newton's law of *F=ma*, trajectory of any ion inside the quadrupole can be described as:

$$F_x = -\frac{ex}{r_0^2}[U + V\cos(\omega t)] \qquad \text{Eq, 1.3}$$

$$F_y = \frac{ey}{r_0^2}[U + V\cos(\omega t)] \qquad \text{Eq, 1.4}$$

$$F_z = 0 \qquad \text{Eq, 1.5}$$

$$\frac{d^2x}{dt^2} + \frac{ex}{mr_0^2}[U + V\cos(\omega t)] = 0 \qquad \text{Eq, 1.6}$$

$$\frac{d^2y}{dt^2} + \frac{ey}{mr_0^2}[U + V\cos(\omega t)] = 0 \qquad \text{Eq, 1.7}$$

$$\frac{d^2z}{dt^2} = 0 \qquad \text{Eq, 1.8}$$

where m is the mass of the ion in kg, z is the charge state, e is the elementary charge ($1.602e^{-19}$ C). The solutions to these differential equations would give a complete description of the trajectory of any ion in terms of each ion's initial conditions. The solution to Eq. 1.8 is trivial; it describes that the position and velocity of an ion along the z axis remains unaffected by any potential applied to the electrode structure. Notice that the use of electrodes of hyperbolic cross section leads to equations of motion that contain no cross-coordinate terms. Therefore, the motion of the particle remains independent along each of the three coordinate axes. Now, if we define the parameters "a" and "q" using Eq. 1.9 and Eq. 1.10, and rearrange Eq. 1.6 and Eq. 1.7

using Mathieu's differential equation, Eq. 1.11 can be used to describe the trajectory of an ion in the quadrupole mass analyzer.

$$a = \frac{4eU}{mr_0^2\omega^2} \qquad \text{Eq, 1.9}$$

$$q = \frac{2eV}{mr_0^2\omega^2} \qquad \text{Eq, 1.10}$$

$$\frac{d^2u}{d\xi^2} + [a_u + 2q_u\cos(2\xi)]u = 0 \qquad \text{Eq, 1.11}$$

where $\xi = t/2$. Solutions to Eq. 1.11 can be obtained by plotting a and q, also known as the stability diagram (see Figure 1.5), which can be used to determine the stability of ions in a quadrupole at different *m/z*. Practically, the ratio of a to q, or $2U/V$, is always held constant so that only certain ions with restricted *m/z* can traverse the quadrupole, while the others hit the rods, being neutralized and pumped away.[64] By decreasing the slope ($2U/V$) of a straight line with an intercept at zero (also known as the mass scan line), the band pass region (represented by the width, Δq) become wider, allowing an increasing *m/z* range pass through (increased sensitivity), while the resolution is reduced. Therefore, the quadrupole acts as a mass filter by variation of the magnitude of U and V while holding U/V constant.[64]

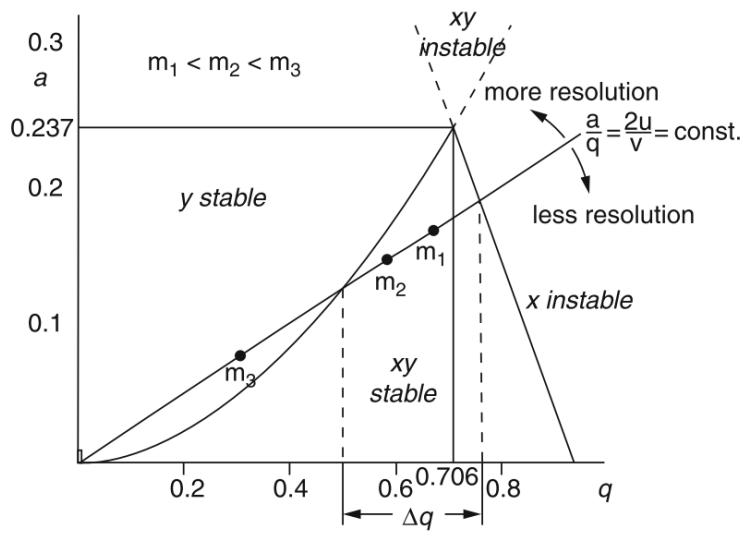

Figure 1.5 The stability diagram of a quadrupole analyzer, adapted from Ref 65.

The RF-only operation mode of the quadrupole can be achieved by setting *U* to zero (corresponding to the scan line equivalent to the *q* axis), and in this case, ions at a wide range of m/z are transmitted. The lowest *m/z* of ions with stable trajectories is determined by the right-hand *q*-intercept.[64] The reason is that *m* is inversely proportional to "q" and "a", see Eqs. 1.6 and 1.7 above.

1.2.2.2 Orbitrap mass spectrometer

A Q-Exactive hybrid quadrupole-orbitrap mass spectrometer (Thermo Fisher Scientific, Waltham, US), equipped with a nano ESI source was used in Chapters 2 and 3. The orbitrap mass analyzer consists essentially of three electrodes (see Figure 1.6). Outer electrodes have the shape of cups facing each other; a spindle-like central electrode holds the trap together and aligns it via dielectric end-spacers (see Figure 1.7). When the voltage is applied between the outer and the central electrodes, the resulting electric field is strictly linear along the axis of the central electrode (z) and thus oscillations along this direction will be purely harmonic. At the same time, the radial component of the field strongly attracts ions to the central electrode.[66]

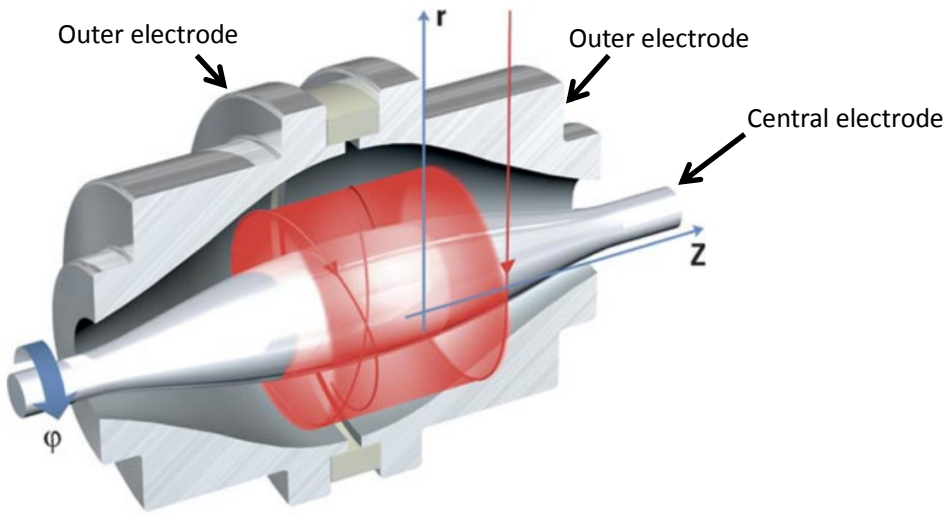

Figure 1.6 Cartoon representation of an orbitrap mass analyzer, adapted from Ref 66.

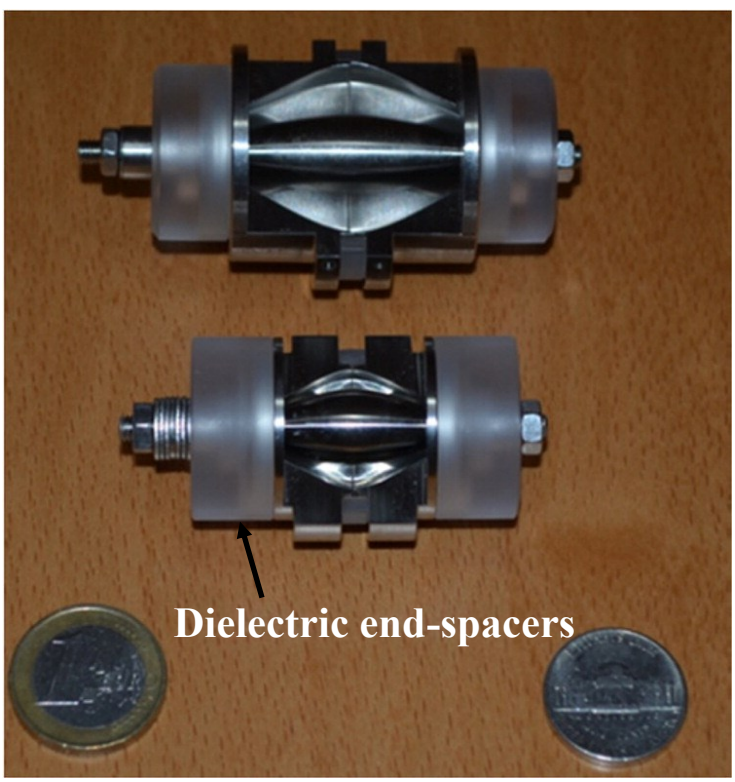

Figure 1.7 Orbitrap mass analyzer, adapted from Ref 66.

Ions are injected into the volume between the central and outer electrodes along a tangent through a specially machined slot with a compensation electrode (a "deflector") in one of the outer electrodes. With a voltage applied between the central and outer electrodes, a radial electric field bends the ion trajectory toward the central electrode while tangential velocity creates an opposing centrifugal force. With a correct choice of parameters, the ions remain on a nearly circular spiral inside the trap. At the same time, the axial electric field (in the z axis) caused by the special conical shape of electrodes pushes ions toward the widest part of the trap initiating harmonic axial oscillations. Outer electrodes are then used as receiver plates for image current detection of these axial oscillations. The digitized image current in the time domain is Fourier-transformed into the frequency domain in the same way as Fourier Transformed Ion Cyclotron Resonance (FTICR) and then converted into a mass spectrum (see Figure 1.8).[66]

When ions start their motions at the correct energy and radius, stable trajectories are formed which combine three cyclic motions (see Figure 1.9). Rotational motion around the central electrode with a frequency of rotation ω_φ (see Eq. 1.12), radial motion with a frequency ω_r (see Eq. 1.13), and axial oscillations along the central electrode with a frequency ω (see Eq. 1.14).[67]

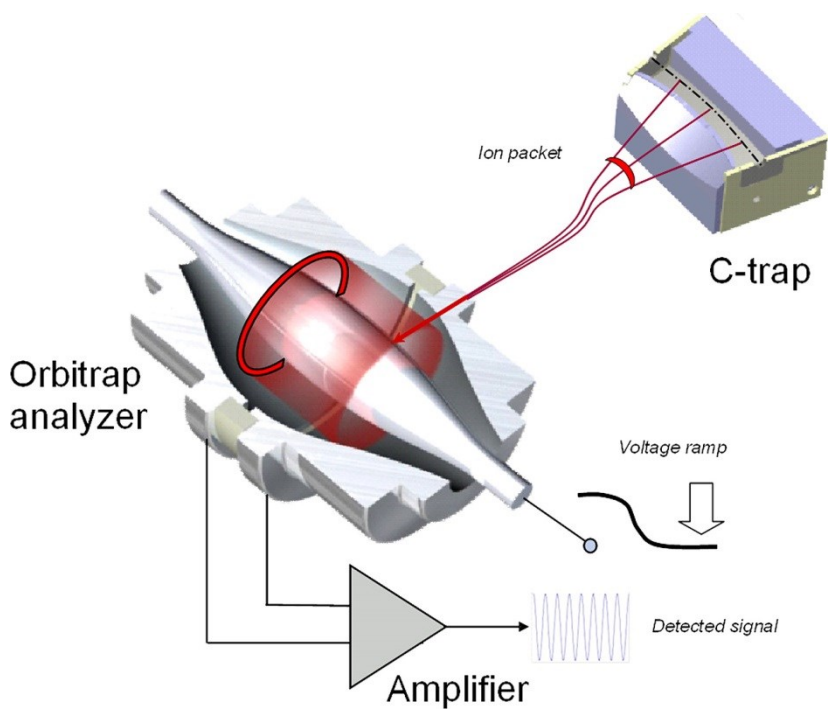

Figure 1.8 Orbitrap mass analyzer, detection of image current, adapted from Ref 66.

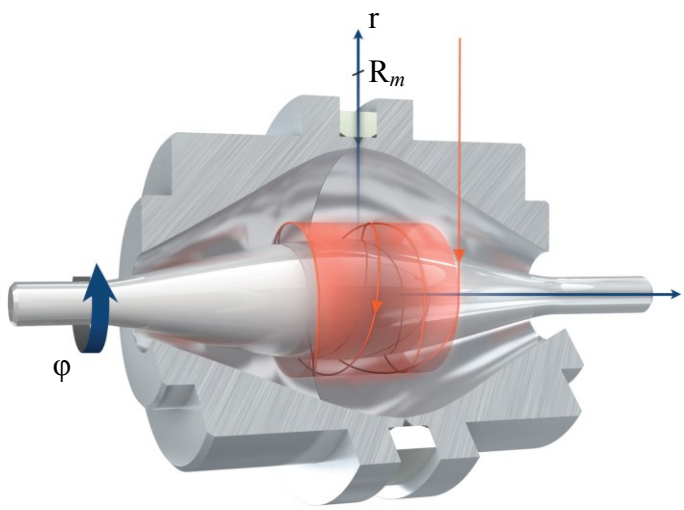

Figure 1.9 Representation of the cyclic motions, adapted from Ref 67.

$$\omega_{\varphi} = \frac{\omega}{\sqrt{2}}\sqrt{\left(\frac{R_m}{R}\right)^2 - 1} \qquad \text{Eq, 1.12}$$

$$\omega_{r} = \omega\sqrt{\left(\frac{R_m}{R}\right)^2 - 2} \qquad \text{Eq, 1.13}$$

$$\omega = \sqrt{k\left(\frac{e}{m/z}\right)} \qquad \text{Eq, 1.14}$$

where R is the initial radius of the spiral, R_m is the characteristic radius, k is the field curvature, e is the elementary charge ($1.602e^{-19}$ C). Rotational and radial frequencies show dependence of the initial radius R. The axial frequency, on the other hand, is completely independent of all initial velocities and the coordinates of the ions. Therefore, only the axial frequency can be used for determination of mass-to-charge ratios, m/z.[67] The resolving power (*Res*) is proportional to the

ratio of the detection time T_{det} to the period of main oscillations T as described in Eq. 1.15, while T is directly proportional to the square root of *m/z*, see Eq. 1.16. This allows the orbitrap mass analyzer to show relatively higher resolving power at high *m/z* in comparison with FTICR where T is directly proportional to *m/z*. Therefore, for any FTICR and for any orbitrap device, there is a critical m/z_c below which the resolving power achieved for the same T is higher for FTICR but above which the orbitrap analyzer starts to show higher resolving power.[66] Also, the orbitrap mass analyzer can be coupled with separation techniques such as liquid chromatography, which is not possible at a commercial scale using an ICR mass analyzer. However, the orbitrap mass analyzer has some opportunity areas. First, the detection of low-abundance species might be hampered by the presence of other species with relatively much higher abundance. Typically, charge is accumulated by allowing ions of a wide range of m/z to flow into the C-trap for storage. As a result, each mass peak is represented by a number of charges proportional to its abundance and that disadvantages low-abundance peaks.[66] Another limitation is presented by the speed of data acquisition, generally lower than 4 spectra per second can be collected when high resolution is desired. This can be a limitation when Selected Reaction Monitoring (SRM) experiments are performed to cover hundreds of analytes per analytical run, which is common situation in the analysis of metabolomics in food and residue analysis in environmental chemistry.[66,67]

$$Res \sim \frac{T_{\mathrm{det}}}{T} \qquad \text{Eq, 1.15}$$

$$T \sim \sqrt{m/z} \qquad \text{Eq, 1.16}$$

For a successful image current detection, an ultra-high vacuum (typically ~$2e^{-10}$ mbar) is required to reduce the collisions with residual gas, which can result in loss of the coherence of ion packages and potential ion fragmentation. Besides, another prerequisite for the successful image current detection is the proper ion injection. A curved RF-only gas filled multipole, C trap, serves as an external ion storage device prior to the injection, where ions are collected through collisions with nitrogen gas. Ions are ejected from the C-trap through the gap between the inner

electrodes by applying fast high-voltage electric pulses (~ hundreds of nanoseconds), and subsequently converge on the entrance of the Orbitrap (see Figure 1.10).[67]

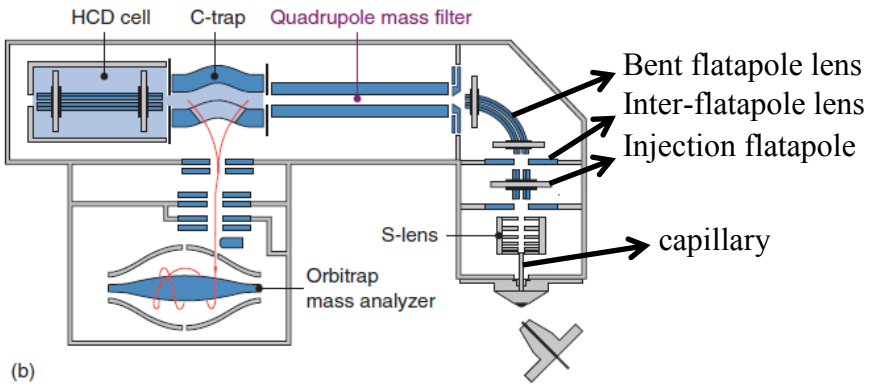

Figure 1.10 Schematic diagram of the Thermo Fisher Q Exactive quadrupole-orbitrap mass spectrometer, adapted from Reference 67.

Shown in Figure 1.10 is a schematic diagram of the Thermo Fisher Q Exactive quadrupole-orbitrap mass spectrometer used in Chapter 2. Gaseous ions generated from nanoESI at atmospheric pressure are drawn into the ion transfer capillary by decreasing pressure and transported to the RF-lens where they are captured and focused into an ion beam. Ions are then transmitted to the low pressure ion optics regions and enter the injection flatapole, where they are trapped, focused and desolvated by maintaining a negative potential on the injection flatapole lens and a positive potential on inter-flatapole lens. Subsequently, ejected ions are focused and guided through the bent flatapole by an axial DC field and a focusing RF field. Then, ions release their kinetic energy through collisions with gas and pass through the C-trap in an ion beam and detected in the Orbitrap mass analyzer. Ion fragmentation can be induced by employing the HCD (Higher energy collisional dissociation) cell, where introduction of gas and the acceleration of ions at the entrance of the cell can increase the efficiency of dissociation.[67]

1.3 ESI-MS based assay

1.3.1 Direct ESI-MS assay

Interactions between proteins and their ligands (including proteins, carbohydrates, lipids, nucleic acids, and small molecules) in solution can be quantified using the direct ESI-MS

assay.[46] For a protein (P) with a single binding site, a complex (PL) is formed with the addition of a ligand (L), and equilibrium is established in solution as:

$$\mathrm{P} + \mathrm{L} \rightleftharpoons \mathrm{PL} \qquad \text{Eq. 1.17}$$

Theoretically, the concentration of the species in solution can be represented by the ratio (R) of the total abundance (Ab) of the ion intensities of ligand-bound (PL) and free protein (P) in the gas-phase (as shown in Eq.1.18). Using the ratio of the species in the gas-phase (observed in the spectrum) and initial concentration of ligand and protein, the dissociation constant can be calculated (Eq. 1.19).

$$R = \frac{Ab(\mathrm{PL})}{Ab(\mathrm{P})} = \frac{[\mathrm{PL}]}{[\mathrm{P}]} \qquad \text{Eq. 1.18}$$

$$K_{\mathrm{d}} = \frac{[\mathrm{P}][\mathrm{L}]}{[\mathrm{PL}]} = \frac{[\mathrm{L}]_0}{R} - \frac{[\mathrm{P}]_0}{R+1} \qquad \text{Eq. 1.19}$$

1.4 Potential pitfalls of ESI-MS assays

Although detecting protein-ligand complexes by ESI-MS assays is relatively easy in terms of simplicity (without labelling or immobilization) and speed (typically less than a minute per analysis), reliability of the binding data needs to be examined. One of the prerequisites is that equilibrium abundances of species in solution must be maintained equally as those of corresponding ions during the ESI process and in gas-phase. These abundances can be affected by physical and chemical processes, which can ultimately lead to inaccurate K_{d} values and binding stoichiometry. Three common sources of errors in ESI-MS measurements and available strategies to tackle these problems are discussed below.[46]

1.4.1 In-source dissociation

Collision-induced dissociation of protein-ligand complexes during the introduction of the ions into the MS (ion sampling) reduces the abundance of PL relative to P, resulting in increased K_{d} values or even false negatives in binding measurements. The occurrence of in-source dissociation depends on the configuration of the ion source used, the choice of instrumental parameters and the size and gas-phase stability of the complex.[46] As an example, bigger the ligand lower the probability of the complex undergoing in-source dissociation because there are

more non-covalent interactions (e.g. hydrogen bonds) taking place in the interaction. Collisional heating of gaseous ions may occur at different stages of ion sampling, such as the heating capillary and skimmer region.[68,69,70] Usually, the occurrence of in-source dissociation can be identified from changes in the ratio of P/PL resulting from changes in ion source parameters, in particular voltage differences in region of high pressure (e.g. nozzle-skimmer voltages), that influences the internal energy of the ions. While low affinity interactions generally exhibit low gas-phase stabilities, some complexes formed by strong ionic bonding in solution are less stable in the gas-phase than those stabilized by hydrophobic interactions.[69,70,71,72]

Low temperature (e.g. sampling capillary), low potential across lens, and short accumulation times are essential for obtaining reliable K_d values for PL complexes susceptible to in-source dissociation. However, 'gentle' source conditions can be detrimental as well. Thus, a balance must be found in minimizing in-source dissociation and achieving adequate protein ion signal. In cases where gentle sampling conditions do not eliminate in-source dissociation, the employment of stabilizing agents may prove beneficial. For example, the addition of imidazole to solution (e.g. > 1 mM) has been shown to prevent gas-phase dissociation, including protein-carbohydrate, protein-fatty acid, and protein-small molecule complexes.[70,71,72] The origin of the stabilizing effects of imidazole is believed to be due, in part, to evaporating cooling resulting from the dissociation of non-specific imidazole adducts from the gaseous PL ions.[70] In cases where it is not possible to eliminate in-source dissociation, a competitive binding assay, such as the reference ligand ESI-MS method may be used.[69] In this approach the direct ESI-MS assay is used to monitor binding of a reference ligand to P in order to quantify the PL interaction. Two basic requirements are necessary for a suitable reference ligand, it binds competitively with P in solution with a known affinity and the PL complex is kinetically stable in the gas-phase.[46]

1.4.2 Non-uniform response factors

Abundances of P and PL detected by ESI-MS are correlated to their corresponding solution concentrations via response factors (*RF*s), which can be discriminated due to the ionization process, mass analyzer, detection efficiencies and in-source dissociation in the cases of labile complexes.[73] The ratio between the solution concentrations is given by Eq. 1.18.

$$\frac{[\mathrm{P}]}{[\mathrm{PL}]} = \frac{RF_{\mathrm{PL}}\,Ab(\mathrm{P})}{RF_{\mathrm{P}}\,Ab(\mathrm{PL})} = RF_{\mathrm{PL/P}}\,\frac{Ab(\mathrm{P})}{Ab(\mathrm{PL})} \qquad \text{Eq, 1.18}$$

where RF_{P} and RF_{PL} are response factors of P and PL. Determination of K_{d} values by direct ESI-MS assay is under the assumption that RF values are uniform (i.e. $RF_{P/\mathrm{PL}} \approx 1$), which is typically valid when P and PL have similar MW (i.e. $\mathrm{MW}_{\mathrm{PL\ compelx}}/\mathrm{MW}_{\mathrm{Protein}} \leq 110\%$).[74] However, in some cases where size and surface properties of P and PL are different (i.e. comparable size of L to P, presence of high MW solute), non-uniform response factors are expected.[75,76] Due to the difference in MWs of proteins used in this work and ligands (carbohydrates), non-uniform response factors are negligible in the present work.

1.4.3 Non-specific binding

False positives of the binding data can be produced by non-specific binding of free ligands to protein and protein-ligand complexes during the ESI process.[77,78] Consequently, the observation of gaseous ions corresponding to a particular PL complex does not establish the presence of that interaction in solution. The observation of multiple ligands bound to the target protein with a Poisson-like distribution might be a sign of occurrence of non-specific ligand binding due to the statistical nature of the phenomenom. Changes in the magnitude of K_{d} with changes in ligand concentration may also alert to the occurrence of non-specific ligand binding. The formation of non-specific PL complexes can be understood in the context of the charged residue model (CRM) discussed previously.[46] Briefly, initial ESI droplets undergo solvent evaporation until they reach the Rayleigh limit, at which point they undergo fission, releasing several small highly charged droplets. This process is repeated until the last hydration shell evaporates and the charges in the surface of the shell are transfer to the complex. If a small highly charged droplet contains more than one analyte molecule, non-specific intermolecular interactions can occur as the droplet evaporates to dryness, leading to the formation of non-specific complexes.[46]

The probability of a small droplet containing more than one analyte molecule increases with analyte concentration.[79] Therefore, a general strategy for minimizing the occurrence of non-specific ligand binding involves limiting the concentration of ligand. However, high ligand concentrations (> 0.05 mM) are typically require to detect weak (K_{d} ~ mM) PL interactions. In

such cases, non-specific interactions are often unavoidable. Non-specific interactions might also be more kinetically stable than those originating in solution (specific interactions).[80] As a result, it is generally not possible to eliminate non-specific interactions by heating the gaseous ions in the source.[46]

A number of methods have been developed to correct nonspecific interactions in ESI.[81,82] The reference protein method, involving the introduction of a non-interacting reference protein (P_{ref}) into the solution, is the most straightforward approach to quantitatively correct for the contribution of non-specific binding with the underlying assumption that in-source dissociation is absent and that the distribution of non-specific protein-ligand complexes is not influenced by the nature of proteins.[81,83] Notably, this method for correcting non-specific binding has been successfully applied to protein interactions with proteins, carbohydrates, divalent metal ions, amino acids and peptides.[45,81,83,84] Although the P_{ref} has been useful to correct for non-specific binding, it still introduces errors to the measurement. The development of a tool for the correction of non-specific binding without introduction of a P_{ref} is the goal of the present work.

1.5 The Present Work

Chapter 2 focuses on the measurement of weak binding affinities by ESI-MS using submicron emitter tips. These emitters significantly mitigate non-specific binding, allowing the measurement of weak glycan-GBP interactions directly from the spectrum without any further treatment. First, the usefulness of the submicron emitter tips was validated using a trisaccharide and lysozyme as a model system, including the measurement of their binding interaction in a reliable biological buffer. Secondly, the P dimer of the Saga strain (P_2^{Saga}) and the interaction with one of its ligand (another trisaccharide) was measured directly from the spectrum using the submicron emitter tips. The spectra were contrasted with data previously obtained and reported by this group using standard emitters.[85] Third, the binding interaction of DC-SIGN with one of its ligand (a tetrasaccharide) and its interaction with calcium ion at physiologically reliable concentration of calcium ion are measured using the submicron emitter tips, however, P_{ref} was needed in order to correct for non-specific binding with calcium ions. Finally, the binding interaction of human galectin 3C (hGal-3C) with lactose, which is prone to in-source ion dissociation, was measured to show an orthogonal application of the submicron emitter tips. This

application was possible because the submicron emitter tips allow the saturation of the protein binding site without affecting the quality of the spectrum. Therefore, the assignment of any loss of gaseous PL complex ions is unambiguously correlated with in-source ion dissociation.

In Chapter 3 we explore the analysis of α2,3-N-acetylneuraminic acid (Neu5Ac) on Prostate-Specific Antigen (PSA) using an enzymatic-aided native ESI-MS approach. PSA is a serine protease produced in the prostate,[86] it digests semenogelins to promote better motility of semen for fertilization purposes.[87] Levels in blood serum are low in healthy individuals, but the structure of the prostate changes during PCa development. Consequently, PSA is released into circulation, therefore, higher levels are detected in PCa patients.[86] Unfortunately, PSA is an organ-specific biomarker not a PCa-specific biomarker.[88-91] This brings misdiagnosis due to false-positive. Moreover, PSA does not have prognostic value for which overtreatment and unnecessary biopsies are major issues as well.[88,90,92] The ratio of α2,3- to α2,6-Neu5Ac on PSA has been reported to offer diagnostic and prognostic value for Prostate Cancer (PCa).[14,89,93] Up to date, most of the methods reported in the literature are ELISA or other related techniques (ELLA, ELECSYS)-based approaches, which provide simplicity, possibility of assay miniaturization and then point-of-care analysis, high sensitivity and minute sample volumes.[94] However, these technologies present drawbacks such as need for labeling, external standards, chemical pre-treatment of the sample, limited repertoire of glycan structural elements recognized by lectins and antibodies, antibody cross reactivity, and lectins with low affinity for carbohydrates.[90,94] Another approah is the relative quantification of carbohydrates on glycoproteins by N-glycan analysis, but it is not suitable for clinical settings. In contrast, relative quantification of glycans by native ESI-MS using enzymatic digestion is fast and requires little sample preparation as intact glycoprotein is analyzed in its native form.[95,96] We employ native ESI-MS for collecting time-resolved data of the enzymatic digestion of α2,3-linked Neu5Ac on PSA glycoforms to indirectly measure the ratio of α2,3- to α2,6-linked Neu5Ac. This approach does not require labeling nor external standard for quantification.

Chapter 4 comprises a summary of this thesis.

1.5 References

(1) Marth, J. D. A Unified Vision of the Building Blocks of Life. *Nat. Cell Biol.* **2008**, *10*, 1015.

(2) Mariño, K.; Bones, J.; Kattla, J. J.; Rudd, P. M. A Systematic Approach to Protein Glycosylation Analysis: A Path through the Maze. *Nat. Chem. Biol.* **2010**, *6*, 713–723.

(3) Pearce, O. M. T.; Läubli, H. Sialic Acids in Cancer Biology and Immunity. *Glycobiology* **2015**, *26*, 111–128.

(4) Tachibana, H.; Taniguchi, K.; Ushio, Y.; Teruya, K.; Osada, K.; Murakami, H. Changes of Monosaccharide Availability of Human Hybridoma Lead to Alteration of Biological Properties of Human Monoclonal Antibody. *Cytotechnology* **1994**, *16*, 151–157.

(5) Cells, C. H. O.; Borys, M. C.; Linze, D. I. H.; Papoutsakis, E. T. Culture PH Affects Expression Rates and Glycosylation of Recombinant Mouse Placental Lactogen Proteins by Chines Ovary Hamster (CHO) Cells. *Nat. Biotechnol.* **1993**, *11*, 720–724.

(6) Doores, K. J.; Bonomelli, C.; Harvey, D. J.; Vasiljevic, S.; Dwek, R. A.; Burton, D. R.; Crispin, M.; Scanlan, C. N. Envelope Glycans of Immunodeficiency Virions Are Almost

Entirely Oligomannose Antigens. *Proc. Natl. Acad. Sci. U. S. A.* **2010**, *107*, 13800–13805.

(7) Clark, M. C.; Baum, L. G. T Cells Modulate Glycans on CD43 and CD45 during Development and Activation, Signal Regulation, and Survival. *Ann. N. Y. Acad. Sci.* **2012**, *1253*, 58–67.

(8) Varki, A. Biological Roles of Glycans. *Glycobiology* **2017**, *27*, 3–49.

(9) Zhao, Y. Y.; Takahashi, M.; Gu, J. G.; Miyoshi, E.; Matsumoto, A.; Kitazume, S.; Taniguchi, N. Functional Roles of N-Glycans in Cell Signaling and Cell Adhesion in Cancer. *Cancer Science*. 2008, 1304–1310.

(10) Sola, R. J.; Griebenow, K. Effects of Glycosylate on the Stability of Protein Pharmaceuticals. *J. Pharm. Sci.* **2009**, *98*, 1223–1245.

(11) Lee, H. S.; Qi, Y.; Im, W. Effects of N-Glycosylation on Protein Conformation and Dynamics: Protein Data Bank Analysis and Molecular Dynamics Simulation Study. *Sci. Rep.* **2015**, *5*, 1–7.

(12) Varki, A.; Cummings, R. D.; Esko, J . D.; Stanley, P.; Hart, G. W.; Aebi, M.; Darvill, A. G.; Kinoshita, T.; Packer, N. H.; Prestegard, J. H.; Schnaar, R. L.; Seeberger, P. H. *Essentials of Glycobiology*, 3rd edition; Cold Spring Harbor Laboratory Press: Cold Spring Harbor (NY), 2017.

(13) Cummings, R. D.; Pierce, J. M. The Challenge and Promise of Glycomics. *Chem. Biol.* **2014**, *21* (1), 1–15.

(14) Llop, E.; Ferrer-Batallé, M.; Barrabés, S.; Guerrero, P. E.; Ramírez, M.; Saldova, R.; Rudd, P. M.; Aleixandre, R. N.; Comet, J.; de Llorens, R.; Peracaula, R. Improvement of Prostate Cancer Diagnosis by Detecting PSA Glycosylation-Specific Changes. *Theranostics* **2016**, *6*, 1190–1204.

(15) Rodriguez, E.; Boelaars, K.; Brown, K.; Li, R. J.; Kruijssen, L.; Bruijns, S. C.; Schetters, S. T.; Crommentuijn, M. H.; van der Horst, J.; van Vliet, S.; Kazemier, G.; Giovannetti, E.; Garcia-Vallejo, J.J.; van Kooyk, Y. Sialic Acids in Pancreatic Cancer Drive Tumour-Associated Macrophage Differentiation via Siglec-7 and Siglec-9. *Nat. Commun.* **2021**, *12*, 1270.

(16) Stowell, S. R.; Ju, T.; Cummings, R. D. Protein Glycosylation in Cancer. *Annu. Rev. Pathol.* **2015**, *10*, 473–510.

(17) Solá, R. J.; Griebenow, K. Glycosylation of Therapeutic Proteins: An Effective Strategy to

Optimize Efficacy. *BioDrugs* **2010**, *24*, 9–21.

(18) Liu, L. Antibody Glycosylation and Its Impact on the Pharmacokinetics and Pharmacodynamics of Monoclonal Antibodies and Fc-Fusion Proteins. *J. Pharm. Sci.* **2015**, *104*, 1866–1884.

(19) Boune, S.; Hu, P.; Epstein, A. L.; Khawli, L. A. Principles of N-Linked Glycosylation Variations of IgG-Based Therapeutics: Pharmacokinetic and Functional Considerations. *Antibodies* **2020**, *9*, 22.

(20) Liang, Y. Applications of Isothermal Titration Calorimetry in Protein Science. *Acta Biochim. Biophys. Sin. (Shanghai).* **2008**, *40*, 565–576.

(21) Dam, T. K.; Brewer, C. F. Thermodynamic Studies of Lectin−Carbohydrate Interactions by Isothermal Titration Calorimetry. *Chem. Rev.* **2002**, *102*, 387–430.

(22) Torres, F. E.; Recht, M. I.; Coyle, J. E.; Bruce, R. H.; Williams, G. Higher Throughput Calorimetry: Opportunities, Approaches and Challenges. *Curr. Opin. Struct. Biol*. 2010, *20*, 598–605.

(23) Rajarathnam, K.; Rösgen, J. Isothermal Titration Calorimetry of Membrane Proteins - Progress and Challenges. *Biochim. Biophys. Acta - Biomembr.* **2014**, *1838*, 69–77.

(24) De Crescenzo, G.; Boucher, C.; Durocher, Y.; Jolicoeur, M. Kinetic Characterization by Surface Plasmon Resonance-Based Biosensors: Principle and Emerging Trends. *Cell. Mol. Bioeng.* **2008**, *1*, 204–215.

(25) Myszka, D. G. Kinetic Analysis of Macromolecular Interactions Using Surface Plasmon Resonance Biosensors. *Curr. Opin. Biotechnol.* **1997**, *8*, 50–57.

(26) Morton, T. A.; Myszka, D. G. Kinetic Analysis of Macromolecular Interactions Using Surface Plasmon Resonance Biosensors. *Methods Enzymol.* **1998**, *295*, 268–282.

(27) Curie, P. Dilatation Électrique Du Quartz Pierre Curie To Cite This Version : HAL Id : Jpa-00238937. *J. Phys. Theor. Appl.* **1889**, *8*, 149–168.

(28) Sandoval, P. J.; Santiago, J. In Vitro Analytical Approaches to Study Plant Ligand-Receptor Interactions. *Plant Physiol.* **2020**, *182*, 1697–1712.

(29) Nomura, T.; Hattori, O. Determination of Micromolar Concentrations of Cyanide in Solution with a Piezoelectric Detector. *Anal. Chim. Acta* **1980**, *115*, 323–326.

(30) Dixon, M. C. Quartz Crystal Microbalance with Dissipation Monitoring: Enabling Real-Time Characterization of Biological Materials and Their Interactions. *J. Biomol. Tech.*

2008, *19*, 151–158.

(31) Vogt, S.; Kelkenberg, M.; Nöll, T.; Steinhoff, B.; Schönherr, H.; Merzendorfer, H.; Nöll, G. Rapid Determination of Binding Parameters of Chitin Binding Domains Using Chitin-Coated Quartz Crystal Microbalance Sensor Chips. *Analyst* **2018**, *143*, 5255–5263.

(32) Howlett, G. J.; Minton, A. P.; Rivas, G. Analytical Ultracentrifugation for the Study of Protein Association and Assembly. *Curr. Opin. Chem. Biol.* **2006**, *10*, 430–436.

(33) Schuck, P. Analytical Ultracentrifugation as a Tool for Studying Protein Interactions. *Biophys. Rev.* **2013**, *5*, 159–171.

(34) Edwards, G. B.; Muthurajan, U. M.; Bowerman, S.; Luger, K. Analytical Ultracentrifugation (AUC): An Overview of the Application of Fluorescence and Absorbance AUC to the Study of Biological Macromolecules. *Curr. Protoc. Mol. Biol.* **2020**, *133*, e131.

(35) Schaller, G. E.; Bleecker, A. B. Ethylene-Binding Sites Generated in Yeast Expressing the Arabidopsis ETR1. *Science* **1995**, *270*, 1809–1811.

(36) Hoare, S. R. J.; Usdin, T. B. Quantitative Cell Membrane-Based Radioligand Binding Assays for Parathyroid Hormone Receptors. *J. Pharmacol. Toxicol. Methods* **1999**, *41*, 83–90.

(37) Maguire, J. J.; Kuc, R. E.; Davenport, A. P. *Book: Methods in Molecular Biology, Receptor Binding Techniques by Davenport, A.P. (Ed). Chapther 3: Radioligand Binding Assays and Their Analysis. 31-78*; 2012; Vol. 897.

(38) Onizuka, T.; Shimizu, H.; Moriwaki, Y.; Nakano, T.; Kanai, S.; Shimada, I.; Takahashi, H. NMR Study of Ligand Release from Asialoglycoprotein Receptor under Solution Conditions in Early Endosomes. *FEBS J.* **2012**, *279*, 2645–2656.

(39) Valverde, P.; Delgado, S.; Martínez, J. D.; Vendeville, J. B.; Malassis, J.; Linclau, B.; Reichardt, N. C.; Cañada, F. J.; Jiménez-Barbero, J.; Ardá, A. Molecular Insights into DC-SIGN Binding to Self-Antigens: The Interaction with the Blood Group A/B Antigens. *ACS Chem. Biol.* **2019**, *14*, 1660–1671.

(40) Cala, O.; Guillière, F.; Krimm, I. NMR-Based Analysis of Protein-Ligand Interactions. *Anal. Bioanal. Chem.* **2014**, *406*, 943–956.

(41) Becker, W.; Bhattiprolu, K. C.; Gubensäk, N.; Zangger, K. Investigating Protein–Ligand Interactions by Solution Nuclear Magnetic Resonance Spectroscopy. *ChemPhysChem*

2018, *19*, 895–906.

(42) Masson, G. R.; Burke, J. E.; Ahn, N. G.; Anand, G. S.; Borchers, C.; Brier, S.; Bou-Assaf, G. M.; Engen, J. R.; Englander, S. W.; Faber, J.; *et al*. Recommendations for Performing, Interpreting and Reporting Hydrogen Deuterium Exchange Mass Spectrometry (HDX-MS) Experiments. *Nat. Methods* **2019**, *16*, 595–602.

(43) Masson, G. R.; Jenkins, M. L.; Burke, J. E. An Overview of Hydrogen Deuterium Exchange Mass Spectrometry (HDX-MS) in Drug Discovery. *Expert Opin. Drug Discov.* **2017**, *12*, 981–994.

(44) Zhang, J.; Kitova, E. N.; Li, J.; Eugenio, L.; Ng, K.; Klassen, J. S. Localizing Carbohydrate Binding Sites in Proteins Using Hydrogen/Deuterium Exchange Mass Spectrometry. *J. Am. Soc. Mass Spectrom.* **2016**, *27*, 83–90.

(45) Deng, L.; Sun, N.; Kitova, E. N.; Klassen, J. S. Direct Quantification of Protein-Metal Ion Affinities by Electrospray Ionization Mass Spectrometry. *Anal. Chem.* **2010**, *82*, 2170–2174.

(46) Kitova, E. N.; El-Hawiet, A.; Schnier, P. D.; Klassen, J. S. Reliable Determinations of Protein-Ligand Interactions by Direct ESI-MS Measurements. Are We There Yet? *J. Am. Soc. Mass Spectrom.* **2012**, *23*, 431–441.

(47) Han, L.; Tan, M.; Xia, M.; Kitova, E. N.; Jiang, X.; Klassen, J. S. Gangliosides Are Ligands for Human Noroviruses. *J. Am. Chem. Soc.* **2014**, *136*, 12631–12637.

(48) Han, L.; Shams-Ud-Doha, K.; Kitova, E. N.; Klassen, J. S. Screening Oligosaccharide Libraries against Lectins Using the Proxy Protein Electrospray Ionization Mass Spectrometry Assay. *Anal. Chem.* **2016**, *88*, 8224–8231.

(49) Shams-Ud-Doha, K.; Kitova, E. N.; Kitov, P. I.; St-Pierre, Y.; Klassen, J. S. Human Milk Oligosaccharide Specificities of Human Galectins. Comparison of Electrospray Ionization Mass Spectrometry and Glycan Microarray Screening Results. *Anal. Chem.* **2017**, *89*, 4914–4921.

(50) El-Hawiet, A.; Chen, Y.; Shams-Ud-Doha, K.; Kitova, E. N.; St-Pierre, Y.; Klassen, J. S. High-Throughput Label- and Immobilization-Free Screening of Human Milk Oligosaccharides Against Lectins. *Anal. Chem.* **2017**, *89*, 8713–8722.

(51) Wang, Y.; Park, H.; Lin, H.; Kitova, E. N.; Klassen, J. S. Multipronged ESI-MS Approach for Studying Glycan-Binding Protein Interactions with Glycoproteins. *Anal. Chem.* **2019**,

91, 2140–2147.

(52) Rademacher, C.; Shoemaker, G. K.; Kim, H. S.; Zheng, R. B.; Taha, H.; Liu, C.; Nacario, R. C.; Schriemer, D. C.; Klassen, J. S.; Peters, T.; et al. Ligand Specificity of CS-35, a Monoclonal Antibody That Recognizes Mycobacterial Lipoarabinomannan: A Model System for Oligofuranoside-Protein Recognition. *J. Am. Chem. Soc.* **2007**, *129*, 10489–10502.

(53) Yao, Y.; Shams-Ud-Doha, K.; Daneshfar, R.; Kitova, E. N.; Klassen, J. S. Quantifying Protein-Carbohydrate Interactions Using Liquid Sample Desorption Electrospray Ionization Mass Spectrometry. *J. Am. Soc. Mass Spectrom.* **2015**, *26*, 98–106.

(54) Konermann, L.; Ahadi, E.; Rodriguez, A. D.; Vahidi, S. Unraveling the Mechanism of Electrospray Ionization. *Anal. Chem.* **2013**, *85*, 2–9.

(55) Kebarle, P.; Verkcerk, U. H. Electrospray: From Ions in Solution to Ions in the Gas Phase, What We Know Now. *Mass Spectrom. Rev.* **2009**, *28*, 898–917.

(56) Loeb, L. B.; Kip, A. F.; Hudson, G. G.; Bennett, W. H. Pulses in Negative Point-to-Plane Corona. *Phys. Rev.* **1941**, *60*, 714–722.

(57) Taylor, G. I.; Mcewan, A. D. The Stability of a Horizontal Fluid Interface in a Vertical Electric Field. *J. Fluid Mech.* **1965**, *22*, 1–15.

(58) Fernández de la Mora, J. The Fluid Dynamics of Taylor Cones. *Annu. Rev. Fluid Mech.* **2007**, *39*, 217–243.

(59) Iribarne, J. V.; Thomson, B. A. On the Evaporation of Small Ions from Charged Droplets. *J. Chem. Phys.* **1976**, *64*, 2287–2294.

(60) Thomson, B. A.; Iribarne, J. V. Field Induced Ion Evaporation from Liquid Surfaces at Atmospheric Pressure. *J. Chem. Phys.* **1979**, *71*, 4451–4463.

(61) Konermann, L.; Ahadi, E.; Rodriguez, A. D.; Vahidi, S. Unraveling the Mechanism of Electrospray Ionization. *Anal. Chem.* **2013**, *85*, 2–9.

(62) Metwally, H.; Duez, Q.; Konermann, L. Chain Ejection Model for Electrospray Ionization of Unfolded Proteins: Evidence from Atomistic Simulations and Ion Mobility Spectrometry. *Anal. Chem.* **2018**, *90*, 10069–10077.

(63) Konermann, L.; Rodriguez, A. D.; Liu, J. On the Formation of Highly Charged Gaseous Ions from Unfolded Proteins by Electrospray Ionization. *Anal. Chem.* **2012**, *84*, 6798–6804.

(64) Miller, P. E.; Denton, M. B. The Quadrupole Mass Filter: Basic Operating Concepts. *J. Chem. Educ.* **1986**, *63*, 617.

(65) Gross, J. H. *Mass Spectrometry*; Springer International Publishing: Cham, 2017; Vol. 56.

(66) Zubarev, R. A.; Makarov, A. Orbitrap Mass Spectrometry. *Anal. Chem.* **2013**, *85*, 5288–5296.

(67) Hecht, E. S.; Scigelova, M.; Eliuk, S.; Makarov, A. *Fundamentals and Advances of Orbitrap Mass Spectrometry*; 2019.

(68) Wang, W.; Kitova, E. N.; Klassen, J. S. Influence of Solution and Gas Phase Processes on Protein-Carbohydrate Binding Affinities Determined by Nanoelectrospray Fourier Transform Ion Cyclotron Resonance Mass Spectrometry. *Anal. Chem.* **2003**, *75*, 4945–4955.

(69) El-Hawiet, A.; Kitova, E. N.; Liu, L.; Klassen, J. S. Quantifying Labile Protein-Ligand Interactions Using Electrospray Ionization Mass Spectrometry. *J. Am. Soc. Mass Spectrom.* **2010**, *21*, 1893–1899.

(70) Sun, J.; Kitova, E. N.; Klassen, J. S. Method for Stabilizing Protein-Ligand Complexes in Nanoelectrospray Ionization Mass Spectrometry. *Anal. Chem.* **2007**, *79*, 416–425.

(71) Liu, L.; Kitova, E. N.; Klassen, J. S. Quantifying Protein-Fatty Acid Interactions Using Electrospray Ionization Mass Spectrometry. *J. Am. Soc. Mass Spectrom.* **2011**, *22*, 310–318.

(72) Bagal, D.; Kitova, E. N.; Liu, L.; El-Hawiet, A.; Schnier, P. D.; Klassen, J. S. Gas Phase Stabilization of Noncovalent Protein Complexes Formed by Electrospray Ionization. *Anal. Chem.* **2009**, *81*, 7801–7806.

(73) Gabelica, V.; Galic, N.; Rosu, F.; Houssier, C.; De Pauw, E. Influence of Response Factors on Determining Equilibrium Association Constants of Non-Covalent Complexes by Electrospray Ionization Mass Spectrometry. *J. Mass Spectrom.* **2003**, *38*, 491–501.

(74) Kitova, E. N.; Kitov, P. I.; Paszkiewicz, E.; Kim, J.; Mulvey, G. L.; Armstrong, G. D.; Bundle, D. R.; Klassen, J. S. Affinities of Shiga Toxins 1 and 2 for Univalent and Oligovalent Pk-Trisaccharide Analogs Measured by Electrospray Ionization Mass Spectrometry. *Glycobiology* **2007**, *17*, 1127–1137.

(75) Chitta, R. K.; Rempel, D. L.; Gross, M. L. Determination of Affinity Constants and Response Factors of the Noncovalent Dimer of Gramicidin by Electrospray Ionization

Mass Spectrometry and Mathematical Modeling. *J. Am. Soc. Mass Spectrom.* **2005**, *16*, 1031–1038.

(76) Lin, H.; Kitova, E. N.; Klassen, J. S. Quantifying Protein-Ligand Interactions by Direct Electrospray Ionization-Ms Analysis: Evidence of Nonuniform Response Factors Induced by High Molecular Weight Molecules and Complexes. *Anal. Chem.* **2013**, *85*, 8919–8922.

(77) Hossain, B. M.; Konermann, L. Pulsed Hydrogen/Deuterium Exchange MS/MS for Studying the Relationship between Noncovalent Protein Complexes in Solution and in the Gas Phase after Electrospray Ionization. *Anal. Chem.* **2006**, *78*, 1613–1619.

(78) Wang, W.; Kitova, E. N.; Klassen, J. S. Nonspecific Protein-Carbohydrate Complexes Produced by Nanoelectrospray Ionization. Factors Influencing Their Formation and Stability. *Anal. Chem.* **2005**, *77*, 3060–3071.

(79) Wang, W.; Kitova, E. N.; Klassen, J. S. Nonspecific Protein-Carbohydrate Complexes Produced by Nanoelectrospray Ionization. Factors Influencing Their Formation and Stability. *Anal. Chem.* **2005**, *77*, 3060–3071.

(80) Wang, W.; Kitova, E. N.; Klassen, J. S. Bioactive Recognition Sites May Not Be Energetically Preferred in Protein-Carbohydrate Complexes in the Gas Phase. *J. Am. Chem. Soc.* **2003**, *125*, 13630–13631.

(81) Sun, J.; Kitova, E. N.; Wang, W.; Klassen, J. S. Method for Distinguishing Specific from Nonspecific Protein-Ligand Complexes in Nanoelectrospray Ionization Mass Spectrometry. *Anal. Chem.* **2006**, *78*, 3010–3018.

(82) Shimon, L.; Sharon, M.; Horovitz, A. A Method for Removing Effects of Nonspecific Binding on the Distribution of Binding Stoichiometries: Application to Mass Spectroscopy Data. *Biophys. J.* **2010**, *99*, 1645–1649.

(83) Sun, N.; Soya, N.; Kitova, E. N.; Klassen, J. S.; Ab, P. Nonspecific Interactions Between Proteins and Charged Biomolecules in Electrospray. *J. Am. Soc. Mass Spectrom.* **2010**, *21*, 472-481.

(84) Sun, J.; Kitova, E. N.; Sun, N.; Klassen, J. S. Method for Identifying Nonspecific Protein-Protein Interactions in Nanoelectrospray Ionization Mass Spectrometry. *Anal. Chem.* **2007**, *79*, 9301–9311.

(85) Han, L.; Zheng, R.; Richards, M. R.; Tan, M.; Kitova, E. N.; Jiang, X.; Klassen, J. S. Quantifying the Binding Stoichiometry and Affinity of Histo-Blood Group Antigen

Oligosaccharides for Human Noroviruses. *Glycobiology* **2018**, *28*, 488–498.

(86) Balk, S. P.; Ko, Y. J.; Bubley, G. J. Biology of Prostate-Specific Antigen. *J. Clin. Oncol.* **2003**, *21*, 383–391.

(87) Sotiropoulou, G.; Pampalakis, G.; Diamandis, E. P. Functional Roles of Human Kallikrein-Related Peptidases. *J. Biol. Chem.* **2009**, *284*, 32989–32994.

(88) O'Reilly, J.-A. Prostate Cancer Detection: Complexities and Strategies. *J. Cancer Treat. Diagnosis* **2017**, *2*, 18–25.

(89) Tabarés, G.; Radcliffe, C. M.; Barrabés, S.; Ramírez, M.; Aleixandre, N.; Hoesel, W.; Dwek, R. A.; Rudd, P. M.; Peracaula, R.; de Llorens, R. Different Glycan Structures in Prostate-Specific Antigen from Prostate Cancer Sera in Relation to Seminal Plasma PSA. *Glycobiology* **2006**, *16*, 132–145.

(90) Tkac, J.; Gajdosova, V.; Hroncekova, S.; Bertok, T.; Hires, M.; Jane, E.; Lorencova, L.; Kasak, P. Prostate-Specific Antigen Glycoprofiling as Diagnostic and Prognostic Biomarker of Prostate Cancer. *Interface Focus* **2019**, *9*.

(91) Lilja, H.; Ulmert, D.; Vickers, A. J. Prostate-Specific Antigen and Prostate Cancer: Prediction, Detection and Monitoring. *Nat. Rev. Cancer* **2008**, *8*, 268–278.

(92) Punnen, S.; Pavan, N.; Parekh, D. J. Finding the Wolf in Sheep's Clothing: The 4Kscore Is a Novel Blood Test That Can Accurately Identify the Risk of Aggressive Prostate Cancer. *Rev. Urol.* **2015**, *17*, 3–13.

(93) Peracaula, R.; Tabarés, G.; Royle, L.; Harvey, D. J.; Dwek, R. A.; Rudd, P. M.; de Llorens, R. Altered Glycosylation Pattern Allows the Distinction between Prostate-Specific Antigen (PSA) from Normal and Tumor Origins. *Glycobiology* **2003**, *13*, 457–470.

(94) Etxebarria, J.; Reichardt, N. C. Methods for the Absolute Quantification of N-Glycan Biomarkers. *Biochim. Biophys. Acta - Gen. Subj.* **2016**, *1860*, 1676–1687.

(95) Wohlschlager, T.; Scheffler, K.; Forstenlehner, I.C.; Skala, W.; Senn, S.; Damoc, E.; Holzmann, J.; Huber, C.G. Native mass spectrometry combined with enzymatic dissection unravels glycoform heterogeneity of biopharmaceuticals. *Nat. Commu.* **2018**, *9*, 1713.

(96) Banazadeh, A.; Veillon, L.; Wooding, K.M.; Zabet-moghaddam, M.; Mechref, Y. Recent advances in mass spectrometric analysis of glycoproteins. *Electrophoresis* **2017**, *38*, 162-189.

Chapter 2
Submicron Emitters Enable Reliable Quantification of Weak Protein-Glycan Interactions by ESI-MS

2.1 Introduction

Interactions between carbohydrates (glycans) and glycan-binding proteins (GBPs) play critical roles in a wide variety of physiological and pathophysiological processes, including immune system activation, autoimmune diseases and inflammation.[1] The discovery and characterization of glycan-GBP interactions is essential to unravelling the mechanisms controlling these processes. Despite their importance, the glycan specificities of most GBPs are not well established. Key challenges to the discovery and comprehensive mapping of functional glycan–GBP interactions include the large number of naturally occurring glycan structures, limited availability of these structures in purified form, the diversity of presentations (e.g. glycoproteins and glycosphingolipids), and the influence of chemical environment on binding.[1] Additionally, the affinities of many specific, functionally-relevant glycan–GBP interactions are

very weak in their monovalent form (dissociation constant (K_d) >μM) and are challenging to reliably quantify with conventional solution binding assays.[1,2]

Isothermal titration calorimetry (ITC) is generally regarded as method of choice for measuring the thermodynamic parameters of glycan–GBP binding. This in-solution assay does not require the immobilization or modification of the ligand or protein. However, obtaining meaningful thermochemical data for very weak interactions (K_d ~1 mM) is challenging, particularly for binding equilibria that exhibit small enthalpy changes, and requires relatively large amounts of material.[3] Saturation-transfer difference nuclear magnetic resonance (STD-NMR) spectroscopy is another in-solution technique for detecting glycan–GBP binding and measuring affinity.[4,5] Although, questions about the reliability of the method for measuring low affinity glycan–GBP interactions have recently emerged.[6] Surface-based binding assays, such as surface-plasmon resonance (SPR) spectroscopy (affinities determined from on- and off-kinetics) and enzyme-linked immunosorbent assays (measures half maximal inhibitory concentrations, IC50), wherein the glycan is immobilized on a surface, are commonly used to evaluate the strength of glycan–GBP complexes.[7,8] While sensitive enough to allow for the detection of weak interactions, these techniques suffer from limitations, most significantly artifacts associated with the chemical modification and immobilization of the glycan ligand, which may alter binding properties and, necessarily, influence the thermodynamic parameters measured.[3,9]

Over the last decade, electrospray ionization mass spectrometry (ESI-MS) has gained in popularity for measuring the binding stoichiometry and affinity of glycan–GBP interactions, as well as other classes of protein-ligand complexes.[3,6,10-12] The assay relies on the distribution of free and ligand-bound GBP that exists in solution being preserved during the ESI process, in the gas phase and through to MS detection (of the corresponding gaseous ions).[13] The reliability of ESI-MS for quantifying moderate-to-high affinity glycan–GBP interactions (K_d <10 μM) has been rigorously tested and the affinities generally agree well with values measured by ITC under similar solution conditions.[13,14] The ESI-MS assay has also been applied to very weak glycan interactions (K_d ~1 mM). In such applications, relatively high concentrations (typically >50 μM) of ligand are required to produce detectable levels of complex. These conditions lead to the appearance of false positives – ions of GBP bound to one or multiple glycan molecules that do

not originate from solution – in the mass spectrum. Signals corresponding to these so-called 'non-specific complexes' must be accounted for, quantitatively, in order to obtain a reliable measure of the glycan–GBP affinity from ESI-MS data.[15,16]

The formation of non-specific complexes can be understood within the context of the charged residue model of ESI. According to this mechanism, the original droplets produced by ESI undergo solvent evaporation until they approach the Rayleigh limit, at which point they undergo Coulombic fission and release small highly charged nanodroplets, from which gaseous ions are ultimately produced.[13,17] As nanodroplets containing two or more analytes (e.g. a free glycan and unbound GBP) evaporate to dryness, non-specific binding can occur, resulting in the formation of stable (detectable) glycan–GBP complexes (i.e., false positives). Detailed studies of the phenomenon of non-specific glycan binding to GBPs in ESI have shown this to be a statistical process, with the probability of non-specific binding increasing with glycan concentration, independent of the nature/structure of protein (in the absence of other perturbations).[15]

Several strategies to correct ESI mass spectra for the occurrence of non-specific glycan–GBP binding (as well as non-specific ligand-protein binding in general) have been developed.[18,19] The most widely-applied approach is the reference protein method, wherein a non-interacting reference protein (P_{ref}) is added to the solution and the measured distribution of glycans bound non-specifically to P_{ref} is used to quantitatively correct the distribution measured for the GBP.[18] When the number of glycan binding sites on GBP is known *a priori*, non-specific binding can also be corrected for using a mathematical approach developed by Sharon and coworkers, which treats all non-specific protein–ligand interactions arising during ESI as having a common K_d.[19] While these methods generally work well, they represent an additional source of error in affinity measurements and are difficult to reliably implement in cases where the protein binds different ligands simultaneously. Moreover, all such correction methods have the general requirement that the glycan–GBP complexes, specific and non-specific, do not undergo gas-phase dissociation during MS sampling (i.e., in-source dissociation).[16,18]

Rather than correct ESI mass spectra for non-specific binding after-the-fact, a more attractive approach is to minimize the formation of such interactions. In principle, this can be accomplished by reducing the size of the initial droplets produced by ESI, which in turn reduces the likelihood of unbound glycans being present in droplets containing free or glycan–bound GBP.[15] It is known that size of primary droplets produced by ESI depend on several factors, mainly on the solution flow rate, which can be controlled by the size of the capillary tip orifice, the spray voltage and current.[20-22] Normally, ESI-MS glycan–GBP binding measurements are performed using tapered glass capillaries (nanoESI tips), with orifice inner diameters (i.d.) of a few μm, which lead to solution flow rates in the nL min^{-1} range (i.e., nanoflow ESI).[20] Because solution flow rates in nanoESI are proportional to the emitter tip diameter[23,24] and it has been reported that the initial size of the droplets that produce gaseous ions is between 5% and 10% of the emitter diameter,[25] the initial droplet diameters produced from aqueous solutions with such tips are estimated to be in the tens to hundreds of nm.[13,20]

Recently, the performance of submicron (i.d. <1 μm) tips in ESI-MS studies has been investigated by multiple laboratories.[26-31] Although the actual sizes of the droplets produced with submicron emitters have not been measured, the small orifice size is expected to reduce the solution flow rate (compared to that of conventional nanoESI tips) which, in turn, will produce droplets with smaller diameters and, concomitantly, decrease the probability of non-specific binding.[15,23,24] Indeed, several studies employing submicron tips have shown a pronounced reduction in the formation of protein adducts involving non-volatile buffers (e.g. phosphate buffer saline (PBS)) and salts.[20,26,28-31] Notably, Donald and co-workers recently described their applicability for protein–ligand binding measurements performed using solutions containing non-volatile buffers (e.g. 50 mM NaCl and 20 mM Tris, 10 mM Na_2SO_4 and 10 mM HEPES).[31] However, not considered in their study was how the use of submicron tips influences the occurrence of non-specific ligand–protein binding and the impact on the quantification of weak interactions.

Here, we describe the significant advantages of submicron emitters, relative to standard tips, for direct ESI-MS measurements of low affinity glycan–GBP interactions. The superior performance of the submicron tips is demonstrated by the results of quantitative binding

measurements performed on model systems with a range of affinities and under various solution conditions. Importantly, the use of the submicron emitters almost completely eliminates the formation of non-specific glycan–GBP complexes at ligand concentrations approaching 1 mM. This allows the affinities of very weak interactions (as low as ~5 mM) to be directly measured from the mass spectrum. Moreover, the general suppression of non-specific adduct formation achieved with these tips enables glycan affinity measurements to be carried out in the presence of high concentrations of non-volatile buffers and salts (e.g., PBS and $Ca(CH_3COO)_2$). Exploiting this capability, we describe, for the first time, ESI-MS affinity measurements performed on C-type lectins, which are GBPs that bind glycans in a calcium-dependent manner, at physiologically-relevant Ca^{2+} concentrations. Finally, we show how the use of submicron emitters and the suppression of non-specific glycan binding enable the quantification of glycan–GBP complexes that are prone to in-source (gas-phase) dissociation.

2.2 Experimental

2.2.1 Materials

2.2.1.1 Carbohydrates

The structures of the carbohydrates used in this study are shown in Figure 2.1. β-D-GlcNAc-(1→4)-β-D-GlcNAc-(1→4)-D-GlcNAc (**L1**, MW 627.59 Da) was purchased from Dextra Science and Technology Centre (Reading, UK), β-D-Gal-(1→3)-[α-L-Fuc-(1→2)]-β-D-Gal-OC_2H_5 (**L2**, MW 516.49 Da) was a gift from Alberta Innovates Technology Futures (Alberta, Canada), α-D-Gal-(1→3)-[α-L-Fuc-(1→2)]-β-D-Gal-(1→4)-β-D-Glc-$O(CH_2)_6CH{=}CH_2$ (**L3**, MW 760.34 Da) was a gift from Professor Todd Lowary (University of Alberta), and β-D-Gal-(1→4)-D-Glc (**L4**, MW 342.3) was purchased from Sigma-Aldrich Canada (Oakville, Canada). Stock solutions of each glycan were prepared by dissolving a known mass in ultrafiltered water (Milli-Q Millipore, MA) to achieve a final concentration of ~1 mM (**L1** – **L3**) or ~10 mM (**L4**). All stock solutions were stored at -20 ˚C until needed.

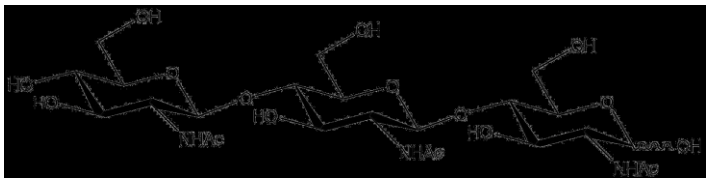

β-D-GlcNAc-(1→4)-β-D-GlcNAc-(1→4)-D-GlcNAc (**L1**)

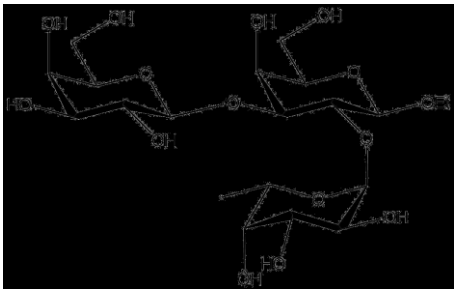

β-D-Gal-(1→3)-[α-L-Fuc-(1→2)]-β-D-Gal-OCH_2CH_3 (**L2**)

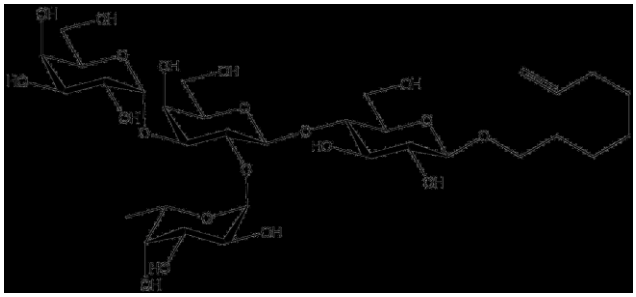

α-D-Gal-(1→3)-[α-L-Fuc-(1→2)]-β-D-Gal-(1→4)-β-D-Glc-$O(CH_2)_6CH{=}CH_2$ (**L3**)

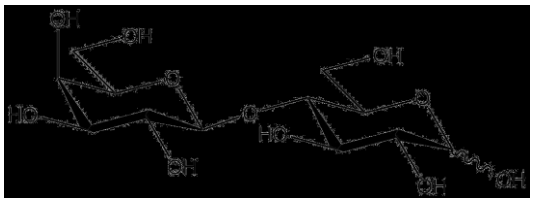

β-D-Gal-(1→4)-D-Glc **(L4)**

Figure 2.1. Structures of the glycan ligands (**L1** – **L4**) used in the present study.

2.2.1.2 Proteins

Human carbonic anhydrase I (HCA, MW 28,848 Da) and lysozyme from chicken egg white (Lyz, MW 14,310 Da) were purchased from Sigma-Aldrich Canada (Oakville, Canada). The P dimer of the Saga strain (P_2^{Saga}, MW 69,734 Da) was produced and purified as described elsewhere.[5] A single chain variable fragment (scFv, MW 26,539 Da) of the anti-*Salmonella O*-polysaccharide monoclonal antibody Se115-4 was prepared as described elsewhere.[6] The recombinant fragment of the C-terminus (residues 107-250) carbohydrate recognition domain of

human galectin 3 (hGal-3C, MW 16,327) was a gift from Professor Chris Cairo (University of Alberta). Protein stock solutions were dialyzed against 200 mM aqueous ammonium acetate pH 6.8 four times (4x) using an Amicon 0.5 mL microconcentrator with a MW cut-off of 3 kDa or 10 kDa (EMD Millipore, Billerica, MA) and stored at -20 ˚C until needed. A fragment of the dendritic cell-specific intercellular adhesion molecule-3-grabbing non-integrin (DC-SIGN) containing the carbohydrate recognition domain (CRD, residues 250-404, MW 17,794 Da) was prepared following a reported procedure that is briefly described in Supporting Information.[32] To prepare the stock solution, the CRD was dialyzed four times (4x) against 200 mM aqueous ammonium acetate pH 7.4 with EDTA and six times (6x) without EDTA using an Amicon 0.5 mL microconcentrator with a MW cut-off of 10 kDa and stored at -20 ˚C until needed. The concentration of each protein stock solution was estimated by UV absorption at 280 nm.

2.2.1.3 Preparation of DC-SIGN CRD

Briefly, DC-SIGN expression was carried out in lysogeny broth (LB) medium containing 100 μg mL^{-1} ampicillin. An overnight culture (100 ml) was started by inoculation from the frozen glycerol stock and grown with shaking at 37 °C. 40 mL of this culture was diluted into 2 liters of LB medium that was incubated at 37 °C with shaking until an A550 of around 0.7 was reached. Protein expression was induced by addition of isopropyl-β-D-thiogalactoside (final concentration, 0.5 mM) and cultures were incubated for a further 3 h at 37 °C with shaking, and the cells harvested by centrifuging at 6000 rpm in JLA8.1 rotor for 30 min at 4 °C. Cells were washed in 50 mM Tris-HCl, pH 7.8 (resuspension buffer), centrifuged at 8,000 rpm in JA-14 rotor for 15 min at 4 °C, re-suspended in 100 ml of cold resuspension buffer, and lysed by the cell disruptor at 20,000 psi. Triton X-100 (final concentration is 2%) was added into the lysis and incubated at 4 °C with stirring. The mixture was centrifuged at 8,000 rpm in JA-14 rotor for 15 min at 4 °C in order to remove the soluble and insoluble proteins. Inclusion bodies were washed with the resuspension buffer three times by centrifugation at 8,000 rpm in JA-14 rotor for 15 min at 4 °C and the pellet was solubilized in 50 ml of 8 M urea containing 100 mM Tris-HCl, pH 7.0, and 0.01% β-mercaptoethanol, by brief sonication followed by gentle rotation for overnight at 4 °C. The mixture was dialyzed against with refolding buffer (50 mM Tris-HCl, pH 7.8, containing 2 M urea, 25 mM $CaCl_2$, 0.5 M NaCl and 10% glycerol) and refolding buffer without urea and followed by the column binding buffer (50 mM Tris-HCl, pH 7.8, containing 25 mM

$CaCl_2$ and 0.5 M NaCl). After dialysis, insoluble precipitate was removed by centrifugation at 40,000 rpm in Ti45 rotor for 1 h at 4 °C and the supernatant was loaded onto a Man-Sepharose column (5 mL) pre-equilibrated with loading buffer. The column was washed with loading buffer (10 column volumes) and eluted with 4 column volumes of eluting buffer (25 mM Tris-HCl, pH 7.8 containing 0.5 M NaCl, and 2.5 mM EDTA). Fractions were dialyzed against MQ water three times and lyophilized and stored at -80 °C freezer.

2.2.2 Methods

2.2.2.1 Mass spectrometry

All ESI-MS binding measurements were performed in positive ion mode using a Q Exactive Orbitrap mass spectrometer (Thermo Fisher Scientific, U.K.) equipped with a modified nanoESI source. Standard and submicron emitters were produced from borosilicate capillary glass with filament (1.0 mm outside diameter (o.d.), 0.78 mm inner diameter (i.d.), 10 cm length and 1.2 mm o.d., 0.69 mm i.d., 10 cm length, respectively, Sutter Instruments, CA) using a P-1000 micropipette puller and a P-97 micropipette puller (Sutter Instruments, CA), respectively. The emitters were imaged using an Orion NanoFab Helium Ion Microscope (HIM; Zeiss, Germany) at the Fabrication and Characterization Centre (University of Alberta). To perform nanoESI, a platinum wire was inserted into the open end of the emitter, making contact with the solution, and a voltage of ~0.8 kV was applied. The Capillary temperature was 180 ˚C, S-lens RF level was 100, maximum inject time was 200 ms and each 10 microscans were combined into a single scan. The typical scan rate was 20 scan min^{-1} and approximately 100 scans were used for affinity measurements. Due to clogging of the emitters, fewer scans (typically between 20 and 40 scans) were used for binding measurements performed at high salt concentrations (e.g. 1X PBS). Data acquisition and pre-processing was performed using the Xcalibur software (version 4.1); ion abundances were extracted using in-house software (SWARM).[33]

2.2.2.2 Isothermal titration calorimetry

The ITC measurement was carried out using a VP-ITC (MicroCal Inc., Northampton, MA, USA). For each ITC experiment, the Lyz solution (0.18 mM) in the sample cell was titrated with a solution of **L1** (1.0 mM); both the protein and ligand were in aqueous ammonium acetate solutions (200 mM, pH 7.2, 25 °C).

2.3 Analysis of ESI-MS binding data

2.3.1 Affinity measurements

2.3.1.1 Lyz-L1

For a monovalent protein-ligand (PL) complex (Eq. 1), such as the Lyz-**L1** interaction, the affinity (K_d, Eq. 2) can be calculated from the ratio (R) of total abundance (Ab) of L-bound to free P ions (Eq. 3) measured by ESI-MS:

$$\mathrm{P} + \mathrm{L} \rightleftharpoons \tag{1}$$

$$K_\mathrm{d} = \frac{[\mathrm{P}][\mathrm{L}]}{[\mathrm{PL}]} = \frac{[\mathrm{L}]_0}{R} - \frac{[\mathrm{P}]_0}{R+1} \tag{2}$$

$$R = \frac{Ab(\mathrm{PL})}{Ab(\mathrm{P})} = \frac{[\mathrm{PL}]}{[\mathrm{P}]} \tag{3}$$

where $[\mathrm{P}]_0$ and $[\mathrm{L}]_0$ are initial concentrations of P and L, respectively.[13] The abundance ratio R measured by ESI-MS is taken to be equal to the equilibrium concentration ratio in the solution (Eq. 3). In principle, K_d can be calculated at a single concentration (of P and L). However, for low affinity interactions it is generally advisable to use a titration approach, wherein the initial protein concentration is fixed and the initial ligand concentration is varied. In this case the affinity can be determined by fitting Eq. 4 to a plot of fraction bound protein ($R/(R+1) \equiv F$) versus $[\mathrm{L}]_0$ (at constant $[\mathrm{P}]_0$):

$$F = \frac{[\mathrm{P}]_0 + [\mathrm{L}]_0 + K_\mathrm{d} - \sqrt{(K_\mathrm{d} - [\mathrm{L}]_0 + [\mathrm{P}]_0)^2 + 4K_\mathrm{d}[\mathrm{L}]_0}}{2[\mathrm{P}]_0} \tag{4}$$

2.3.1.2 P_2^{Saga}-L2

P_2^{Saga} possesses two equivalent and independent glycan binding sites. In this case, stepwise L binding can be described by Eqs. 5a and 5b:

$$\mathrm{P} + \mathrm{L} \rightleftharpoons \mathrm{PL} \tag{5a}$$

$$\mathrm{PL} + \mathrm{L} \rightleftharpoons \mathrm{PL_2} \tag{5b}$$

The corresponding equations of mass balance are:

$$[\mathrm{L}]_0 = [\mathrm{L}] + [\mathrm{PL}] + 2[\mathrm{PL_2}] \tag{5c}$$

$$[P]_0 = [P] + [PL] + [PL_2] \tag{5d}$$

For two independent binding sites,[6] the dissociation constants for sequential binding ($K_{d,1}$ and $K_{d,2}$, respectively) can be expressed by Eqs. 6a and 6b:

$$K_{d,1} = \frac{[P][L]}{[PL]} = \frac{[L]_0}{R_1} - \frac{[P]_0(R_1 + 2R_2)}{R_1(1 + R_1 + R_2)} = \frac{[L]_0 - 2Fs[P]_0}{R_1} \tag{6a}$$

$$K_{d,2} = \frac{[PL][L]}{[PL_2]} = \frac{R_1[L]_0}{R_2} - \frac{R_1[P]_0(R_1 + 2R_2)}{R_2(1 + R_1 + R_2)} = \frac{[L]_0 - 2Fs[P]_0}{R_2/R_1} \tag{6b}$$

where R_1 and R_2 are calculated from Eqs. 7a and 7b, respectively:

$$R_1 = \frac{Ab(PL)}{Ab(P)} = \frac{[PL]}{[P]} \tag{7a}$$

$$R_2 = \frac{Ab(PL_2)}{Ab(P)} = \frac{[PL_2]}{[P]} \tag{7b}$$

and the fraction of L-occupied binding sites (Fs) can be expressed by Eq. 8:

$$Fs = \frac{Ab(PL) + 2Ab(PL_2)}{2(Ab(P) + Ab(PL) + Ab(PL_2))} = \frac{[PL] + 2[PL_2]}{2([P] + [PL] + [PL_2])} = \frac{R_1 + 2R_2}{2(1 + R_1 + R_2)} \tag{8}$$

2.3.1.3 CRD-Ca^{2+}

DC-SIGN CRD possesses three Ca^{2+} binding sites and Ca^{2+} stepwise binding can be described by Eqs. 9a-c:

$$P + Ca^{2+} \rightleftharpoons PCa^{2+} \tag{9a}$$

$$PCa^{2+} + Ca^{2+} \rightleftharpoons P(Ca^{2+})_2 \tag{9b}$$

$$P(Ca^{2+})_2 + Ca^{2+} \rightleftharpoons P(Ca^{2+})_3 \tag{9c}$$

The corresponding equations of mass balance are:

$$[Ca^{2+}]_0 = [Ca^{2+}] + [PCa^{2+}] + 2[P(Ca^{2+})_2] + 3[P(Ca^{2+})_3] \tag{10a}$$

$$[P]_0 = [P] + [PCa^{2+}] + [P(Ca^{2+})_2] + [P(Ca^{2+})_3] \quad (10b)$$

where $[Ca^{2+}]_0$ is the initial concentration of calcium ions. The apparent dissociation constants ($K_{d,i}$) for sequential for the addition of Ca^{2+} (where the i = 1-3) can be expressed by Eqs. 11a-c:

$$K_{d,1} = \frac{[P][Ca^{2+}]}{[PCa^{2+}]} = \frac{[Ca^{2+}]_0 - 3Fs[P]_0}{R_1} \quad (11a)$$

$$K_{d,2} = \frac{[PCa^{2+}][Ca^{2+}]}{[P(Ca^{2+})_2]} = \frac{[Ca^{2+}]_0 - 3Fs[P]_0}{R_2/R_1} \quad (11b)$$

$$K_{d,3} = \frac{[P(Ca^{2+})_2][Ca^{2+}]}{[P(Ca^{2+})_3]} = \frac{[Ca^{2+}]_0 - 3Fs[P]_0}{R_3/R_2} \quad (11c)$$

where R_1, R_2 and R_3 ($\equiv R_i$) are the abundance ratios of the Ca^{2+}-bound protein ($P(Ca^{2+})_i$) to free P measured by ESI-MS, Eq. 12:

$$R_i = \frac{Ab(P(Ca^{2+})_i}{Ab(P)} = \frac{[P(Ca^{2+})_i]}{[P]} \quad (12)$$

and Fs in this case is described by Eq. 13:

$$Fs = \frac{\sum iR_i}{3(1+\sum R_i)} \quad (13)$$

If all three calcium binding sites are equivalent and independent, with an intrinsic (per binding site) dissociation constant of $K_{d,intrin}$, $K_{d,i}$ will be related by statistical coefficients as shown in Eq. 14:

$$3K_{d,1} = K_{d,2} = \frac{1}{3} K_{d,3} = K_{d,intrin} \quad (14)$$

If, instead, the binding sites are equivalent but dependent, such that sequential binding exhibits cooperativity (positive or negative), $K_{d,i}$ will be related as shown in Eq. 15:

$$3K_{d,1}=\frac{1}{\alpha}K_{d,2}=\frac{1}{3\beta}K_{d,3}=K_{d,intrin} \quad (15)$$

where α and β are the associated cooperativity factors.

2.3.1.4 CRD-L3

DC SIGN CRD possesses a single glycan binding site and the affinity can be found using Eq. 2 or Eq. 4. In this case, the signals corresponding to specifically bound Ca^{2+} and non-specific adducts (e.g., NH_4^+ and CH_3COO^-) observed for the free and ligand-bound CRD were included in the calculation of the abundance ratio *R* (Eq. 3).

2.3.1.5 hGal-3C-L4

In principle, the monovalent interaction between hGal-3C and **L4** can be quantified using Eq. 2 or Eq. 4. However, due to in-source dissociation of the complex, these calculations will lead to an overestimation of K_d. To account for the partial dissociation of the complex in the source, concentration-dependent *F* values can be analyzed using Eq. 16:

$$F=\frac{[L]_0+[P]_0+K_d-\sqrt{(K_d-[L]_0+[P]_0)^2+4K_d[L]_0}}{2[P]_0}(1-d_f) \quad (16)$$

where d_f is the fraction of the complex that undergoes dissociation in the ion source. The value of d_f is the difference between the theoretical maximum of *F* (1.0) and the maximum value established from fitting Eq. 16 to the experimental *F* values.

2.3.2 Correction for non-specific binding

Non-specific ligand binding, when present, was corrected for using the reference protein method.[18] This method involves the addition of a non-interacting reference protein (P_{ref}) to the solution. The underlying assumption is that the distributions of L bound non-specifically to P_{ref} and P are identical.[18] To perform the correction, the fractional abundance of P_{ref} bound non-specifically to q molecules of L (f_q, where $q \geq 0$) was calculated using Eq. 17:

$$f_q = \frac{Ab(P_{ref}L_q)}{\sum_q Ab(P_{ref}L_q)} \quad (17)$$

The true (in the absence of non-specific binding) abundances of free and ligand-bound P ($Ab(PL_i)$, where $i \geq 0$) are related to the apparent abundances ($Ab(PL_i)_{app}$) and f_q as shown in Eq. 18:

$$Ab(PL_i)_{app} = f_0 Ab(PL_i) + f_1 Ab(PL_{i-1}) + f_2 Ab(PL_{i-2}) + \ldots + f_q Ab(PL_{i-q}) \quad (18)$$

Rearrangement leads to the following expressions for the true abundances of P (Eq. 19a), PL (Eq. 19b) and, more generally, PL_i (Eq. 19c):

$$Ab(P) = Ab(P)_{app}/f_0 \quad (19a)$$

$$Ab(PL_1) = (Ab(PL_1)_{app} - f_1 Ab(P))/f_0 \quad (19b)$$

$$Ab(PL_i) = (Ab(PL_i)_{app} - f_1 Ab(PL_{i-1}) - f_2 Ab(PL_{i-2}) - \ldots - f_q Ab(PL_{i-q}))/f_0 \quad (19c)$$

2.4 Results and Discussion

2.4.1 Submicron emitters: dimensions and performance

The average i.d. of the standard nanoESI tips used in the present work, imaged by HIM, was 2.0 ± 0.1 μm. This is similar to that of emitters used previously by our laboratory for quantitative glycan–GBP binding measurements.[3,10,14] Analysis of HIM images acquired for submicron emitters suggests they have an average i.d. of 50 ± 10 nm, which places them among the smallest reported to date (Table 2.1).[20,26-28,31] The diameters of the initial droplets produced with these tips are estimated to be <5 nm, *vide supra*. Representative images of the standard and submicron tips are shown in Figure 2.2.

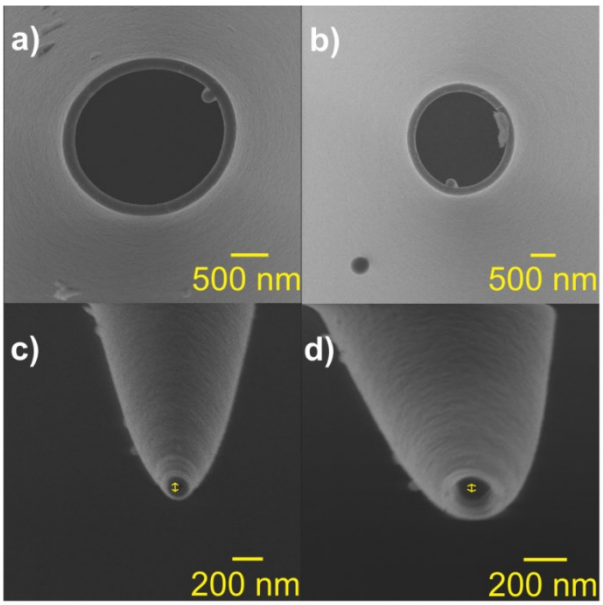

Figure 2.2. Representative HIM images acquired for (a, b) standard and (c, d) submicron emitters. The double headed arrow indicates approximately the position and the diameter of the orifice of the submicron emitters.

To evaluate the performance of the submicron tips for glycan–GBP binding, measurements were performed under a variety of solution conditions using two model systems: lysozyme (Lyz) binding to the trisaccharide **L1** and the sequential binding of the trisaccharide **L2** to the protruding domain (P-dimer) of the capsid protein of the Saga strain of human norovirus (P_2^{Saga}). The monovalent interaction between Lyz and **L1** has been quantified previously using a variety of biophysical methods, including ESI-MS.[14] While a range of affinities have been reported, the value of 6.8 ± 0.2 μM, measured by ITC in an aqueous ammonium acetate solution (200 mM, pH 7.2, 25 °C) in this study, was taken as the benchmark (Figure 2.3). The P_2^{Saga} is a homodimer with two equivalent and independent glycan binding sites.[6] The reported apparent affinities for the sequential binding of **L2** in aqueous ammonium acetate (300 mM, pH 7.0, 25 °C) are 1.85 ± 0.01 mM ($K_{d,1}$) and 6.25 ± 0.03 mM ($K_{d,2}$).[6]

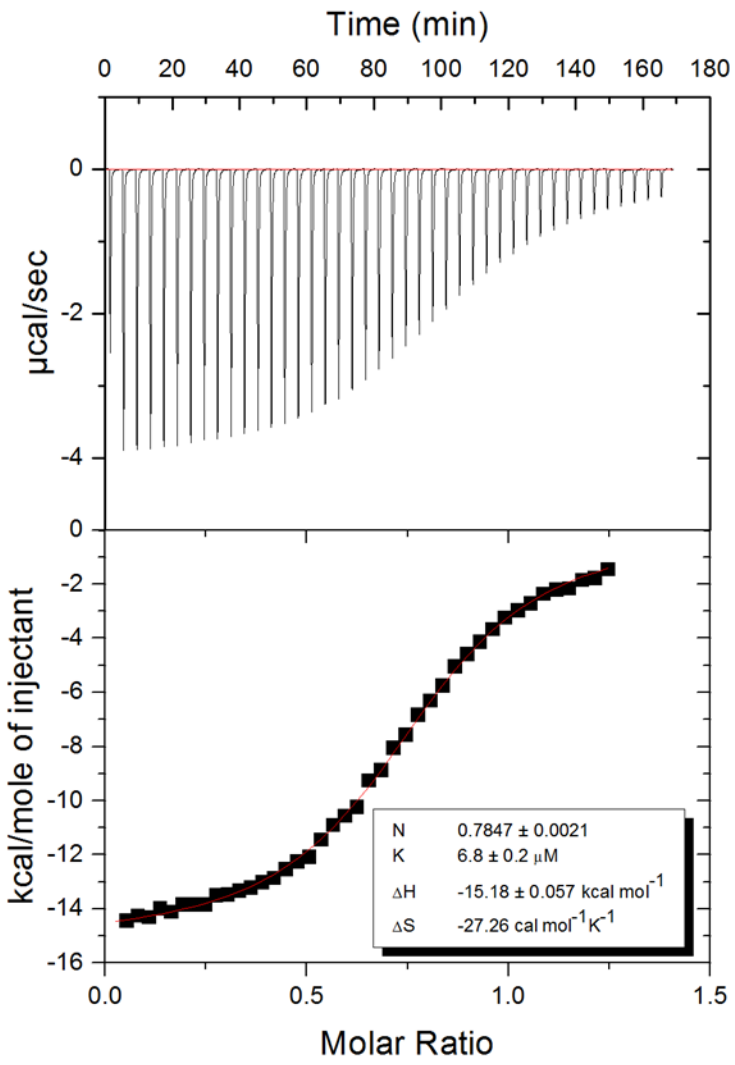

Figure 2.3. ITC thermogram measured for Lyz (0.18 mM) and **L1** at different concentrations up to 1 mM. The interaction was measured in an aqueous ammonium acetate solution (200 mM, pH 7.2 and 25 °C).

2.4.2 L1–Lyz

ESI-MS affinity measurements were performed using both submicron and standard tips on aqueous ammonium acetate solutions (200 mM, pH 7.2, 25 °C) of Lyz (5 µM) and **L1** at initial concentrations ranging from 10 µM to 150 µM. A reference protein (P_{ref}, 1 µM) was added to all solutions to monitor the occurrence of non-specific binding. Portions of the ESI mass

spectra containing Lyz and P_{ref} ions, measured at four different ligand concentrations (10 μM, 25 μM, 75 μM and 150 μM), are shown in Figure 2.4 and Figure 2.5, respectively.

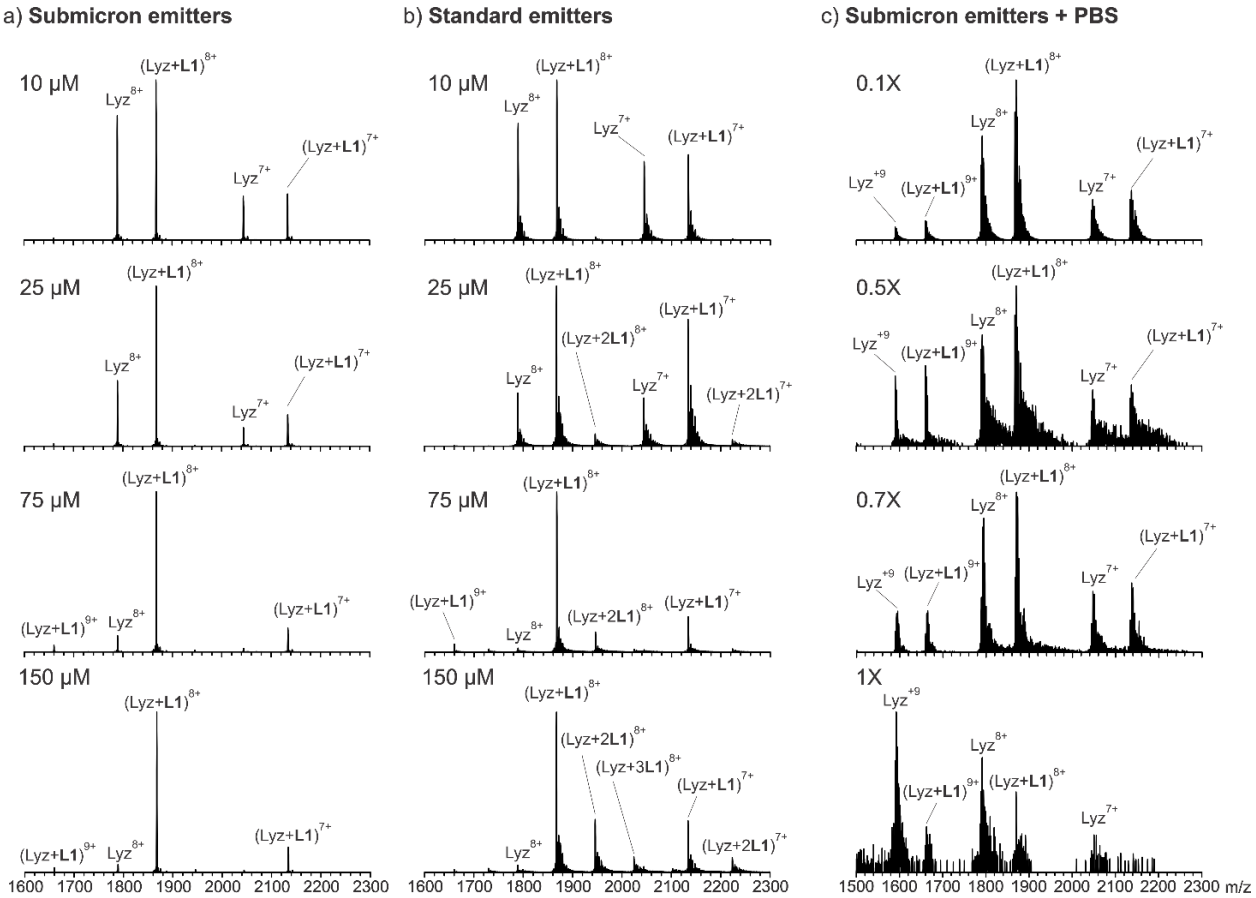

Figure 2.4. Representative ESI mass spectra acquired in positive ion mode for aqueous ammonium acetate solutions (200 mM, pH 7.2) of Lyz (5 μM), P_{ref} (1 μM) and **L1** (10 μM, 25 μM, 75 μM, and 150 μM) using (a) submicron and (b) standard emitters. (c) ESI mass spectra acquired for aqueous ammonium acetate solutions (200 mM, pH 7.2) of Lyz (10 μM), **L1** (20 μM) and non-volatile PBS buffer at concentrations of 0.1X, 0.5X, 0.7X and 1X (where 1X PBS corresponds to 137 mM NaCl, 2.7 mM KCl, 10 mM Na_2HPO_4 and 1.8 mM KH_2PO_4). The signal-to-noise ratio (S/N) of the highest intensity signals measured in panels (a) and (b) for the solutions containing 150 μM **L1** are $2x10^4$ and $3x10^3$, respectively. The S/N for the highest intensity peak measured in panel (c) at 0.1X and 1X PBS are 900 and 8, respectively.

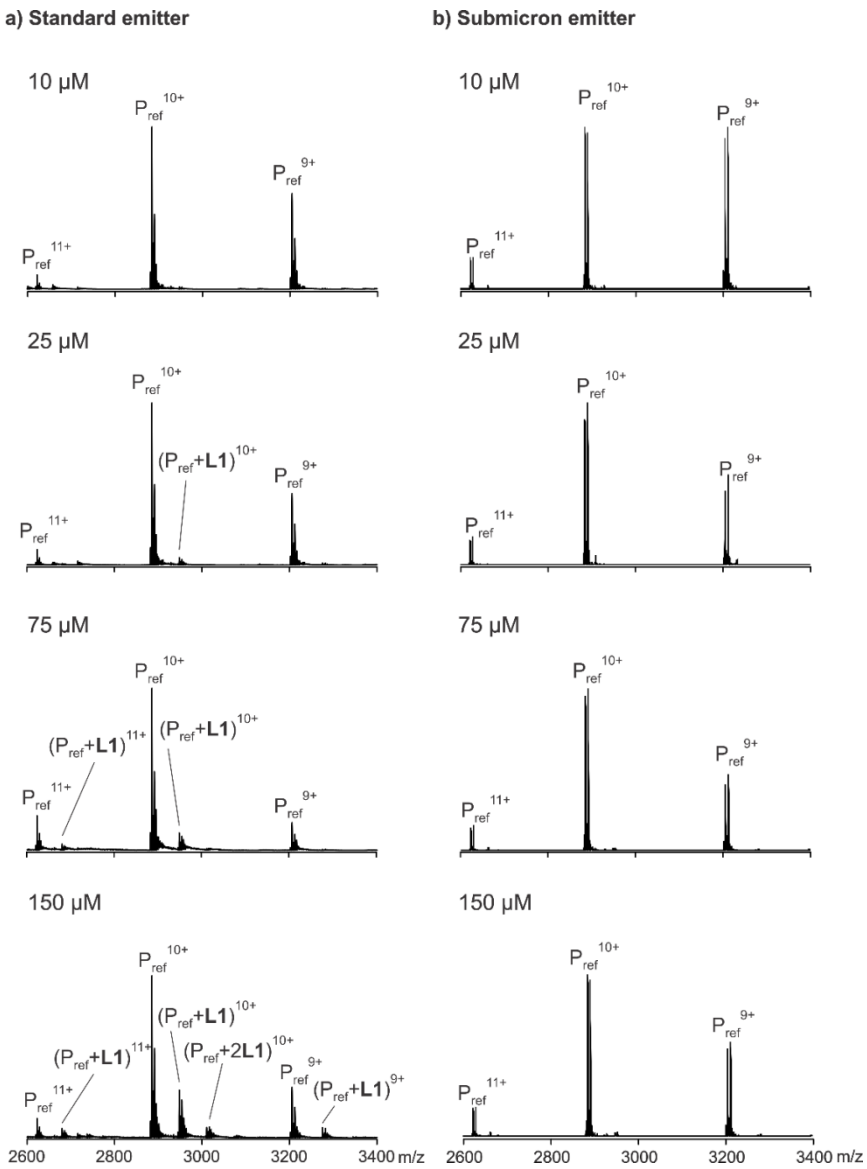

Figure 2.5. Representative ESI mass spectra acquired in positive ion mode for aqueous ammonium acetate solutions (200 mM, pH 7.2) of Lyz (10 μM), P_{ref} (1 μM) and **L1** at 10 μM; 25 μM; 75 μM; 150 μM, using (a) standard and (b) submicron emitters.

At the lowest **L1** concentrations tested (<25 μM), the relative abundances of free and **L1**-bound Lyz ions measured with standard and submicron tips are reasonably similar (*R* values agree within 20%) and there is no evidence of non-specific binding. However, at higher concentrations, non-specific **L1** binding is evident in the mass spectra acquired with standard tips. For example, at 25 μM, ions corresponding to (Lyz + 2**L1**) were detected (and account for

5% of the Lyz signal), while at >75 μM, (Lyz + 3**L1**) ions were observed. Non-specific **L1** binding to P_{ref} was also evident in the mass spectra measured for solutions with **L1** concentrations ≥25 μM (Figure 2.4). In contrast, in the mass spectra acquired with the submicron tips, (Lyz + 2**L1**) ions were either absent or, if detected, represented ≤2% of the Lyz signal, even at the highest concentration tested. Moreover, there was negligible signal corresponding to non-specific P_{ref}-**L1** complexes at all concentrations (Figure 2.5 and Figure 2.6). Analysis of concentration-dependence of the fraction of **L1**-bound Lyz established directly from the mass spectra acquired with the submicron tips (Figure 2.7a) yielded an affinity of 6.5 ± 0.9 μM (Table 2.2), which is in good agreement with the ITC value (6.8 ± 0.2 μM). Notably, following correction of the mass spectra acquired using standard tips for non-specific binding using the P_{ref} method (Figure 2.6a and Figure 2.7b), a similar K_d (6.9 ± 1.7 μM) was obtained (Table 2.2).

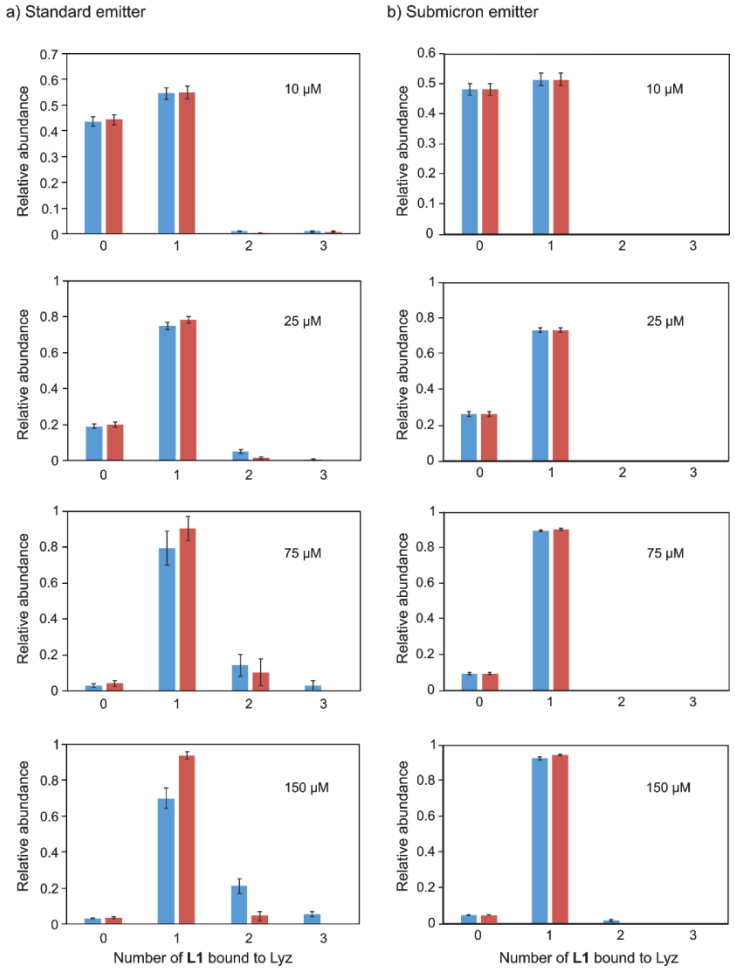

Figure 2.6. Distribution of **L1** bound to Lyz measured by ESI-MS performed in positive ion mode on aqueous ammonium acetate solutions (200 mM, pH 7.2) of Lyz (10 μM), P_{ref} (1 μM) at 10 μM; 25 μM; 75 μM; 150 μM, using (a) standard and (b) submicron emitters The blue bars represent distributions determined directly from the mass spectra; the red bars are the distributions after correction for non-specific binding. The error bars correspond to one standard deviation.

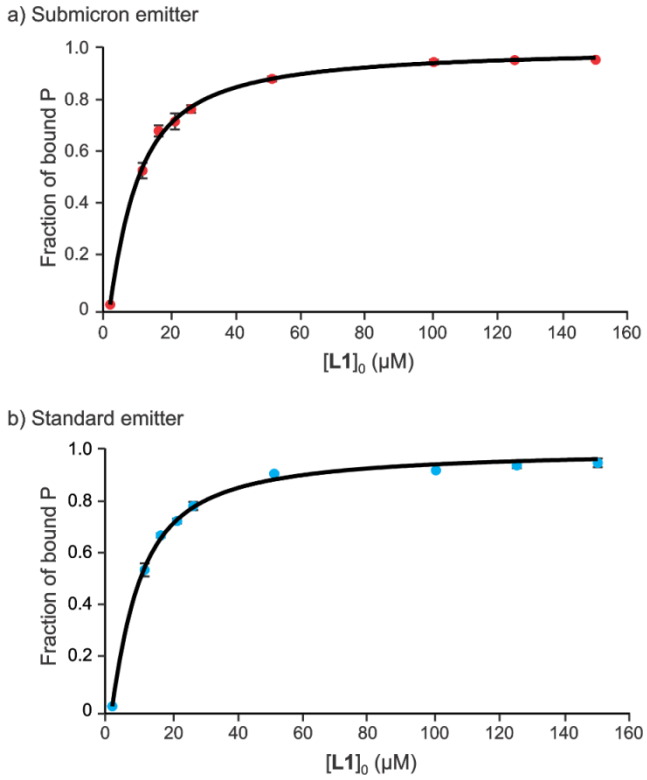

Figure 2.7. Plots of fraction (*F*) of ligand-bound Lyz versus initial **L1** concentration measured for aqueous ammonium acetate solutions (200 mM, pH 7.2) of Lyz (10 μM), P_{ref} (1 μM) and **L1** (10 μM, 15 μM, 20 μM, 25 μM, 50 μM, 75 μM, 100 μM, 125 μM and 150 μM) by ESI-MS performed using (a) submicron and (b) standard nanoESI emitters. The mass spectra acquired using the standard emitters were corrected for non-specific binding using the P_{ref} method (the corrected distributions for $[\mathbf{L1}]_0$ of 10 μM, 25 μM, 75 μM, and 150 μM are shown in Figure 2.6a). The error bars correspond to one standard deviation.

The absence of non-specific Lyz-**L1** binding observed with the submicron tips is consistent with the much smaller ESI droplets produced with these tips and the lower probability that offspring droplets contain free **L1** and Lyz or the specific (Lyz+**L1**) complex. This also explains the negligible levels of metal ion (Na^+ and K^+) adducts observed for the Lyz ions, compared to what is observed in the mass spectra acquired with standard tips (Figure 2.4). To further investigate the extent to which adducts of non-volatile salts can be eliminated using these submicron tips, binding measurements were performed on aqueous solutions (pH 7.2, 25 °C) of Lyz (10 μM) and **L1** (20 μM) containing 200 mM ammonium acetate and varying concentrations of PBS. As can be seen in Figure 4c, it is still possible to obtain high quality ESI mass spectra, even at 1X PBS (a buffer containing 137 mM NaCl, 2.7 mM KCl, 10 mM Na_2HPO_4 and 1.8 mM KH_2PO_4), with the submicron tips. In contrast, the mass spectrum acquired for this solution using a standard emitter exhibits broad, unresolved features such that it is impossible to identify the free and ligand-bound Lyz ions (Figure 2.8).

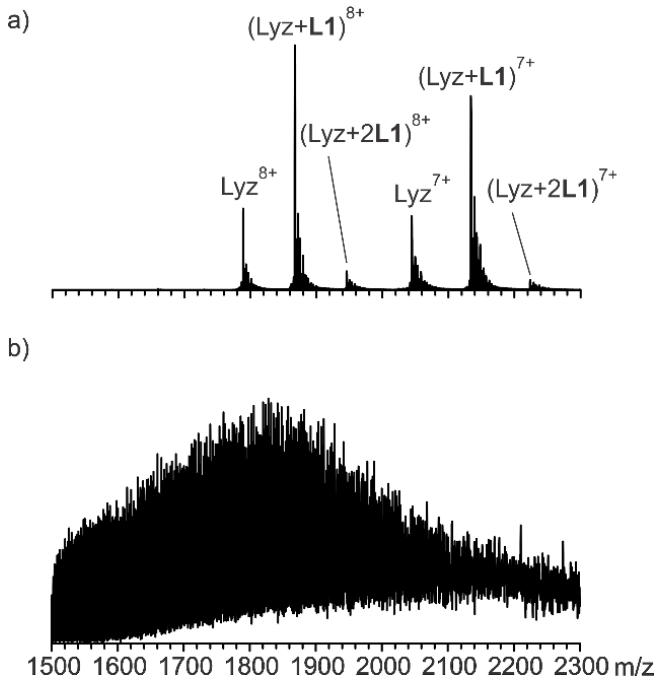

Figure 2.8. Representative ESI-MS spectra acquired in positive ion mode with a standard nanoESI emitter for a 200 mM aqueous ammonium acetate solution (pH 7.2) of Lyz (10 μM) and **L1** (20 μM) in the (a) absence and (b) presence of 1X PBS.

Interestingly, analysis of the relative abundances of free and **L1**-bound Lyz measured with the submicron emitters revealed that the affinity of the interaction decreases with increasing PBS concentration, reaching a value of 35 ± 4 μM at 1X PBS (Figure 2.9). This is in reasonable agreement with previously reported ITC value (24 ± 2 μM) measured in 1X PBS (pH 7.4, 25 °C).[14] The reason for the decrease in affinity with increasing PBS is not known. However, it is notable that a broadening of the Lyz and (Lyz+**L1**) complex charge state distributions (shift towards high charge state) is observed at the higher PBS concentrations (Figure 2.4c), suggesting that the buffer may promote Lyz conformational changes in solution, which weakens binding.

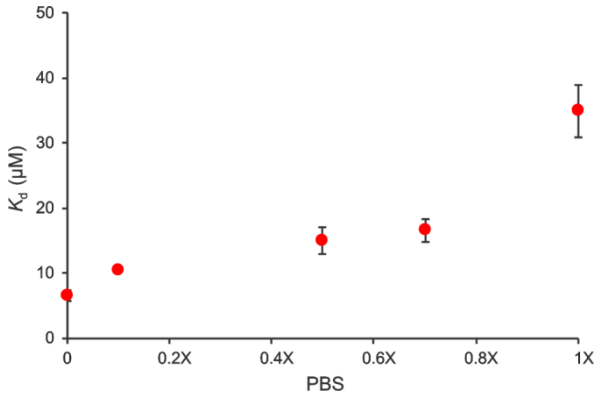

Figure 2.9. Plot of affinity (K_d) of **L1** for Lyz versus PBS concentration. Affinities were measured by ESI-MS performed on aqueous ammonium acetate solutions (200 mM, pH 7.2) of Lyz (10 μM) and **L1** (20 μM) in the presence of PBS (0.1X, 0.5X, 0.7X and 1X), using submicron emitters. Also shown is the K_d measured in the absence of PBS (calculated from data shown in Figure 2.7a). The error bars correspond to one standard deviation.

2.4.3 L2–P_2^{Saga}

The results obtained for the Lyz-**L1** interaction demonstrate that the current submicron tips are suitable for ESI-MS quantification of glycan–GBP interactions and effectively eliminate non-specific glycan binding at concentrations up to 150 μM. However, the (Lyz+**L1**) complex is relatively high affinity and, as noted above, significantly higher ligand concentrations (up to mM) are required to accurately establish the binding stoichiometry and affinity of low affinity interactions. To more rigorously assess the utility of these emitters for studying weak glycan–GBP binding, measurements were performed on the low affinity (mM) interactions of P_2^{Saga} with

L2. These weak interactions are extremely challenging to measure using conventional assays and, thus, are an excellent test of the power of ESI-MS implemented with submicron tips for reliably quantifying low affinity glycan–GBP interactions.

Binding measurements were performed using submicron tips on aqueous ammonium acetate solutions (200 mM, pH 7.4, 25 °C) of P_2^{Saga} (3 μM) and **L2** concentrations ranging from 50 μM to 750 μM (Figure 2.10a). Ions corresponding to the protonated free P_2^{Saga} dominated at all concentrations investigated. Signal corresponding to P_2^{Saga} bound to one **L2** was detected at ligand concentrations ≥50 μM; evidence of two bound **L2** was observed at ≥300 μM. Notably, signal associated with P_2^{Saga} bound to three **L2**, which necessarily arises from non-specific binding, was negligible, even at 750 μM. Moreover, non-specific binding of **L2** to P_{ref} was minor, ≤5% of the P_{ref} signal at the highest ligand concentration (Figure 2.11). In contrast, mass spectra acquired for the same solutions using standard ESI emitters show evidence of extensive non-specific binding to **L2** (Figure 2.10b). For example, at 300 μM, signal corresponding to P_2^{Saga} bound to three **L2** is evident, while at 750 μM, as many as six bound **L2** were detected. From the relative abundances of free and bound P_2^{Saga} measured directly from the mass spectra acquired with submicron tips, the average (over all concentrations) apparent affinities were determined as 1.89 ± 0.01 mM ($K_{d,1}$) and 3.70 ± 0.02 mM ($K_{d,2}$) (Table 2.2). These values are in reasonable agreement with those reported previously.[6] Moreover, the concentration-dependent fraction of occupied (with **L2**) P_2^{Saga} binding sites measured with the submicron emitters are similar to those obtained previously with standard emitters and using the P_{ref} method (Figure 2.12).[6]

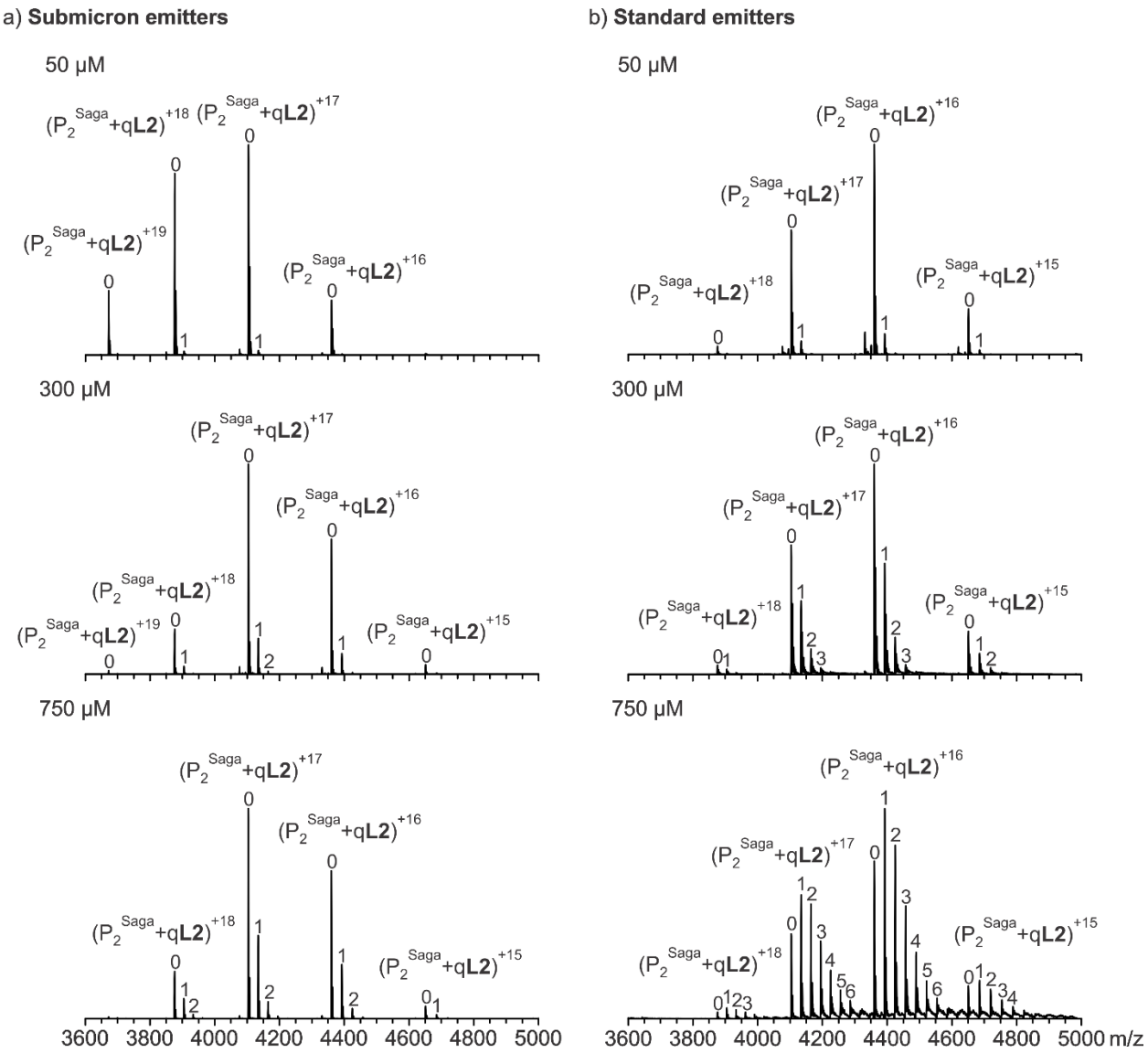

Figure 2.10. Representative mass spectra acquired in positive ion mode in aqueous ammonium acetate solutions (200 mM, pH 7.4) of P_2^{Saga} (3 μM) and **L2** at 50 μM, 300 μM and 750 μM using (a) submicron and (b) standard emitters.

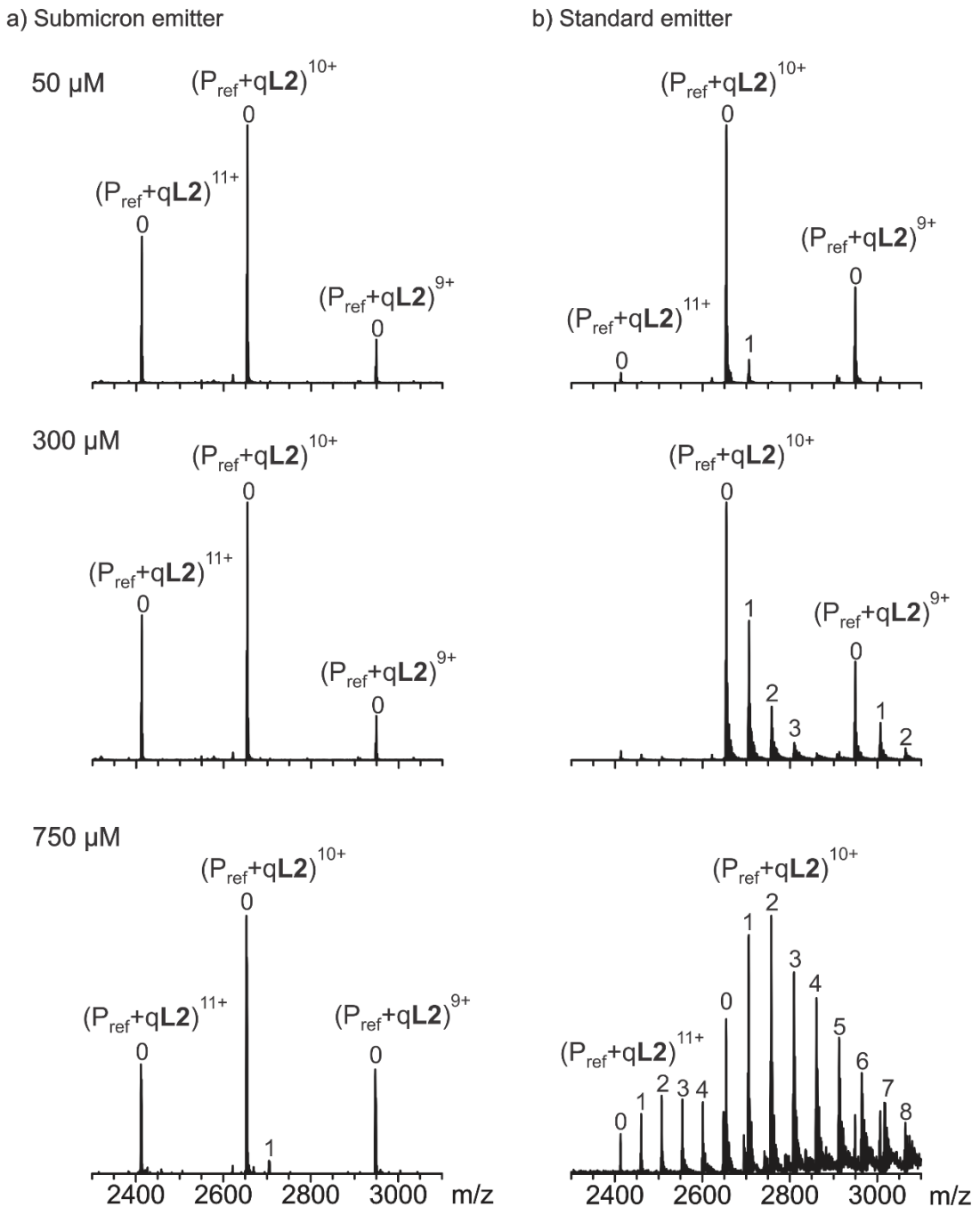

Figure 2.11. Representative ESI mass spectra acquired in positive ion mode for aqueous ammonium acetate solutions (200 mM, pH 7.4) of P_2^{Saga} (3 μM), P_{ref} (1 μM) and **L2** at 50 μM; 300 μM and 750 μM, using (a) submicron and (b) standard emitters.

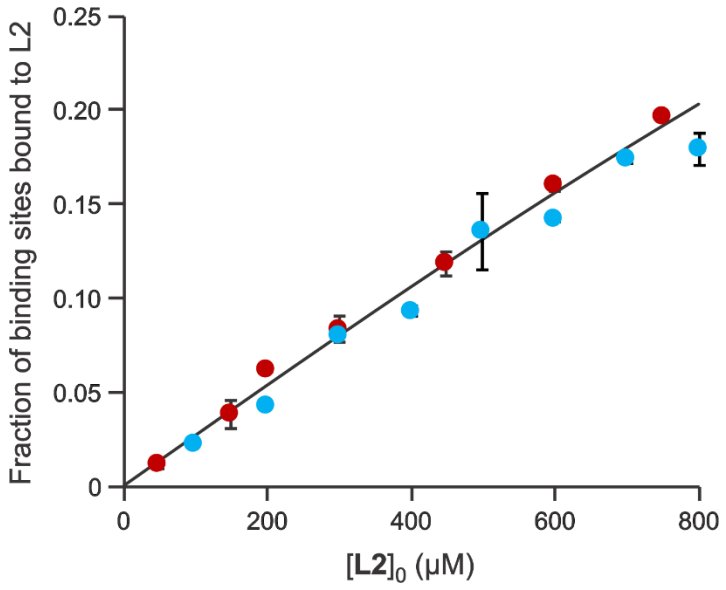

Figure 2.12. Plots of fraction (*Fs*) of P_2^{Saga} binding sites bound to **L2** versus initial ligand concentration measured by ESI-MS performed on aqueous ammonium acetate solutions (200 mM, pH 7.4) of P_2^{Saga} (3 μM) and **L2** (50 μM, 150 μM, 200 μM, 300 μM, 450 μM, 600 μM, 750 μM) using submicron (red circles) and standard emitters (blue circles). The values acquired with the standard emitters were taken from reference 6 and were corrected for non-specific binding using the P_{ref} method. The error bars correspond to one standard deviation.

2.4.4 DC-SIGN CRD

DC-SIGN, a type II transmembrane protein of dendritic cells (antigen presenting cells), plays an important role in the immune response. It is *N*-glycosylated at the Asn80 residue[34] and under native conditions it exists as a homotetramer.[35,36] The carbohydrate recognition domain (CRD) of DC-SIGN, which is non-glycosylated,[36] is reported to bind *N*-linked high mannose oligosaccharides, galactose and branched, fucosylated oligosaccharides, including some human milk oligosaccharides.[37] In all cases, binding is believed to occur in a Ca^{2+}-dependent manner, although the roles that Ca^{2+} plays in glycan binding have not been fully elucidated.[38,39] According to a reported crystal structure, the CRD can bind three Ca^{2+} (at sites Ca-1, Ca-2 and Ca-3).[38] Glycan binding occurs at Ca-2 and involves direct coordination of one of the glycan monosaccharides. To the best of our knowledge, details of the thermodynamics of Ca^{2+} binding to DC-SIGN (or DC-SIGN CRD) have not been reported. However, for DC-SIGNR (a DC-SIGN homologue that shares 77% amino acid sequence identity with DC-SIGN and is structurally

similar to DC-SIGN), Ca^{2+} binding to Ca-1 and Ca-3 is low affinity (compared to binding at Ca-2) in the absence of bound glycan.[40] There is limited quantitative glycan binding data for DC-SIGN CRD. However, the available data suggests that monovalent glycan interactions with DC-SIGN CRD are weak, ~mM. For example, based on the results of ITC measurements, CRD binds to the mannose mono- and disaccharide with K_d's of 3.5 and 0.9 mM, respectively.[41]

The low affinities typical of monovalent DC-SIGN CRD interactions with fucose- and mannose-containing ligands, combined with the requirement for high concentrations of Ca^{2+},[41,42] makes DC-SIGN CRD-glycan interactions an excellent test of the performance of submicron emitters for the study of glycan binding to C-type lectins. With this objective in mind, we first explored glycan-independent Ca^{2+} binding properties of the CRD at neutral pH. We then quantified the influence of Ca^{2+} on the CRD binding to **L3**, an alkyl glycoside of the B type VI tetrasaccharide, the affinity of which is reported to be 2.3 ± 0.6 mM for DC-SIGN CRD.[43]

2.4.4.1 Ca^{2+} binding to DC-SIGN CRD

ESI-MS measurements were performed using submicron tips on solutions of DC-SIGN CRD (3 μM in 200 mM ammonium acetate, pH 7.4, 25 °C) with varying concentrations of $Ca(CH_3COO)_2$ (up to 2.5 mM). A P_{ref} (2 μM) was added to monitor the formation of non-specific Ca^{2+} adducts. In the absence of $Ca(CH_3COO)_2$, the monomeric CRD was detected almost exclusively in its protonated form, with no evidence of bound Ca^{2+} (Figure 2.13). In the presence of $Ca(CH_3COO)_2$, Ca^{2+} binding was detected and the number of bound cations increased with concentration. At 1.0 mM, CRD was associated predominantly with a single Ca^{2+}; CRD bound to three Ca^{2+} was the dominant species observed at ≥2.0 mM. At the highest $Ca(CH_3COO)_2$ concentration tested (2.5 mM), up to six bound Ca^{2+} were detected, along with NH_4^+ and CH_3COO^- adducts. Notably, P_{ref} ions bound to as many as three Ca^{2+} were also detected, along with NH_4^+ and CH_3COO^- adducts (Figure 2.13), indicating that, at high $Ca(CH_3COO)_2$ concentrations, Ca^{2+} (and other ions in solution) bound non-specifically to CRD during ESI. As a result, the P_{ref} method was needed to correct the mass spectra. The relative abundances of free and Ca^{2+}-bound CRD, before and after correction, are shown in Figure 2.14. After taking into account non-specific binding, the CRD is found to bind predominantly to three Ca^{2+} at the highest concentration, which is consistent with the findings from crystallographic studies.[38-40]

Although the fractional abundances of CRD bound to 4 and 5 Ca^{2+} are non-zero, they are low (≤5% of the total CRD signal) and show little dependence on $Ca(CH_3COO)_2$ concentration above 1.0 mM). Therefore, it is likely that the non-zero fractional abundances of species reflect minor deficiencies in the P_{ref} correction method.[6]

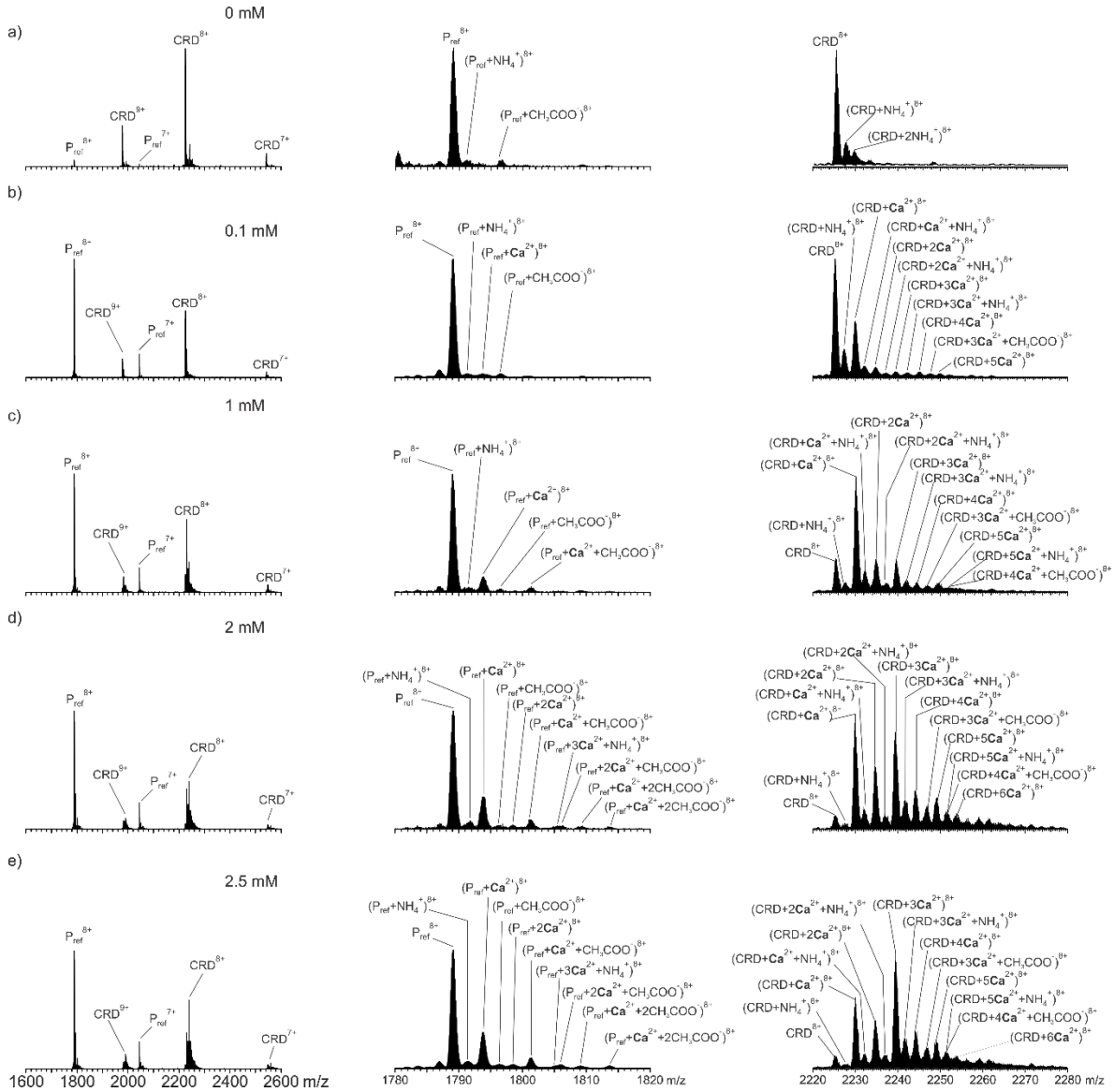

Figure 2.13. Representative ESI mass spectra acquired in positive ion mode for aqueous ammonium acetate solutions (200 mM, pH 7.4) of DC-SIGN CRD (3 μM), P_{ref} (2 μM) and $Ca(CH_3COO)_2$ at (a) 0 mM, (b) 0.1 mM, (c) 1 mM, (d) 2 mM and (e) 2.5 mM using submicron tips. Expanded regions of the mass spectra, corresponding to the 8+ charge states of the P_{ref} and CRD ions, are shown in the centre and right panels, respectively.

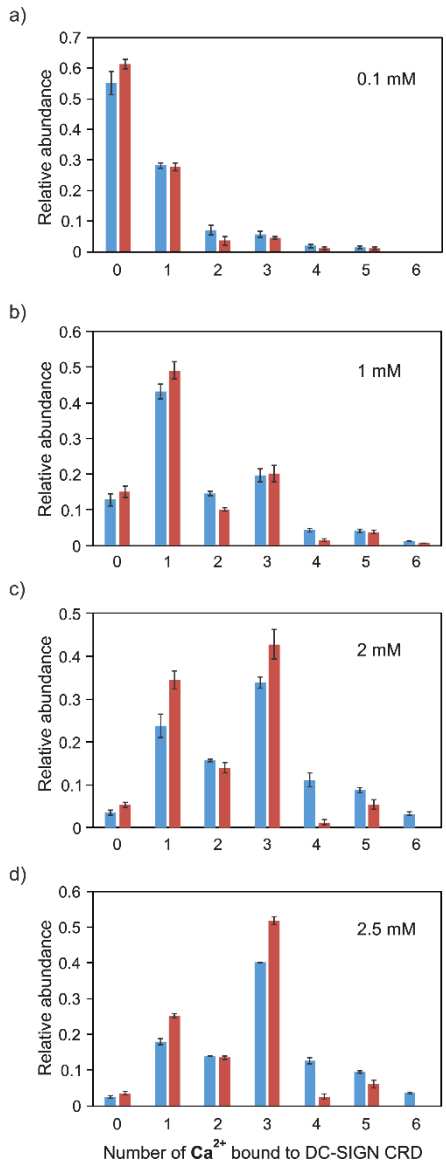

Figure 2.14. Distributions of Ca^{2+} bound to DC-SIGN CRD measured by ESI-MS performed with submicron emitters on aqueous ammonium acetate solutions (200 mM, pH 7.4) of CRD (3 μM), P_{ref} (2 μM) and $Ca(CH_3COO)_2$ at 0.1 mM; 1.0 mM; 2.0 mM; and 2.5 mM. The corresponding mass spectra are shown in Figure 2.13. The blue bars represent distributions determined directly from the mass spectra; the red bars are the distributions after correction for non-specific binding. The error bars correspond to one standard deviation.

While it was not possible to completely eliminate non-specific binding of Ca^{2+}, which has a high (droplet) surface activity, with the submicron tips, it is useful to contrast the quality of the

mass spectra measured at high $Ca(CH_3COO)_2$ concentration with these tips to mass spectra acquired under identical conditions using standard tips. As an example, at 2.5 mM $Ca(CH_3COO)_2$ non-specific binding is extensive with >10 bound Ca^{2+} observed for CRD and >7 for P_{ref} (Figure 2.15). Moreover, the distributions of non-specific adducts is very broad, with overlap between some of the CRD and P_{ref} ions, making the implementation of the P_{ref} method impractical.

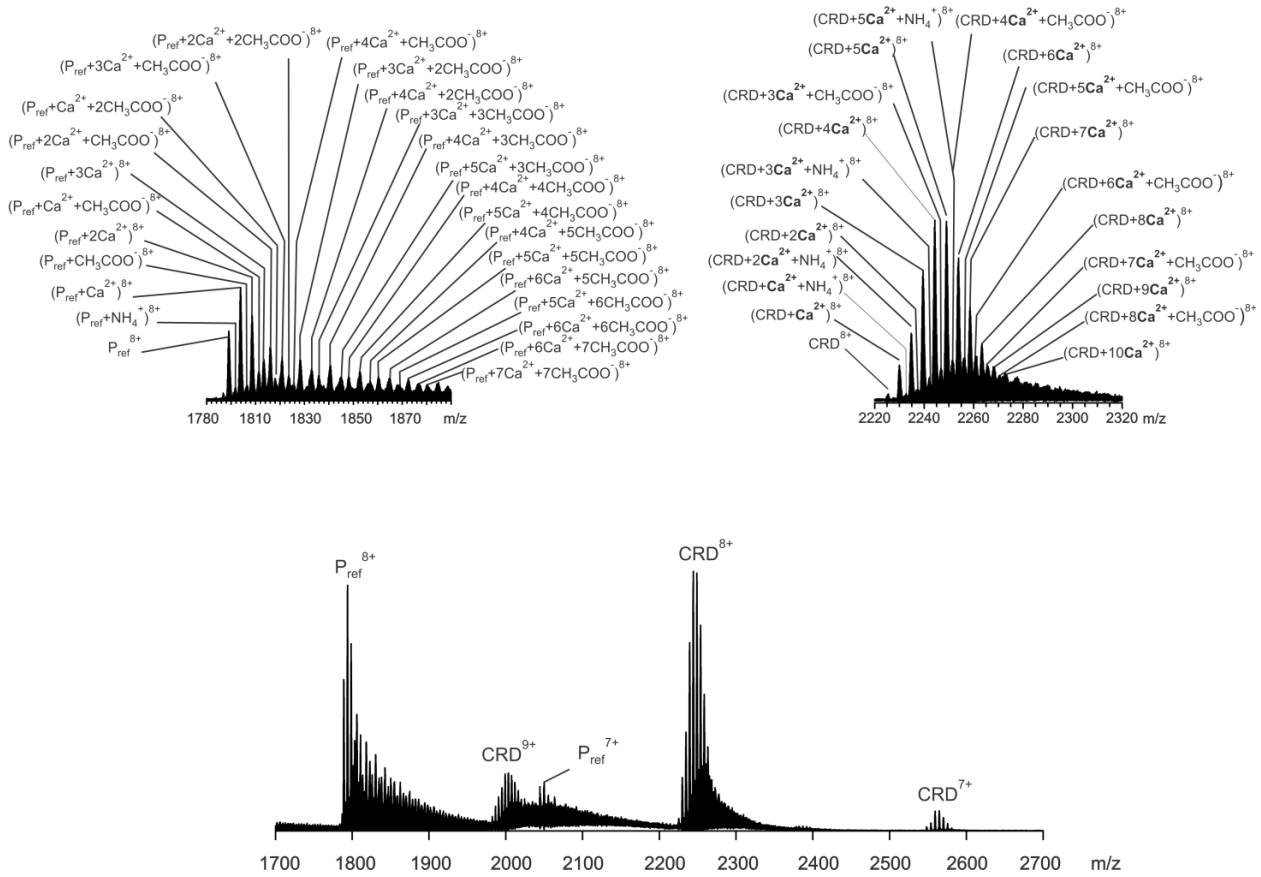

Figure 2.15. Representative ESI mass spectrum acquired with a standard emitter in positive ion mode for an aqueous ammonium acetate solution (200 mM, pH 7.4) of CRD (3 μM), P_{ref} (1.5 μM) and $Ca(CH_3COO)_2$ (2.5 mM). Insets show expanded regions corresponding to the 8+ charge state P_{ref} and CRD ions.

To assess the thermodynamics of Ca^{2+} binding to the three sites, we considered several binding models to account for the Ca^{2+} concentration dependence of the fractional abundances of the free and Ca^{2+}-bound CRD species (Figure 2.16). As a starting point, Eq. 4 was fit to the

fraction of bound binding sites (*Fs*) to obtain a rough estimate of the intrinsic (per binding site) dissociation constant ($K_{d,intrin}$), assuming equivalent and independent binding sites (Figure 2.16a). This analysis yielded a $K_{d,intrin}$ of 1.00 ± 0.08 mM. This value was then used (Eq. 14) to calculate the concentration-dependent fractional abundances of the CRD species. It can be seen that the theoretical curves do not describe the experimental fractions well (Figure 2.16b). Specifically, the fractional abundance of the 2nd bound Ca^{2+} is overestimated while the abundance of the 3rd Ca^{2+} is underestimated. These discrepancies are further illustrated in Figure 2.16c, where the experimental and theoretical fractional abundances are shown for $Ca(CH_3COO)_2$ concentrations of 0.1 mM, 1.0 mM and 2.5 mM. While the overestimation of the 2nd bound Ca^{2+} might be due to non-equivalence of the binding sites, the underestimation of the abundance of the 3rd bound Ca^{2+} can only be due positive cooperativity. To our knowledge, this is the first evidence of cooperative Ca^{2+} binding to DC SIGN.

We next considered a sequential binding model in which the binding sites are treated as equivalent but allows for cooperativity effects for the addition of the 2nd and 3rd Ca^{2+} (Eq. 15). Fitting this model to experimental data yielded a $K_{d,intrin}$ of 0.84 mM and negative and positive cooperativity factors of 6 (α) and 0.25 (β), respectively (Figure 2.16d). It must be emphasized that, although the model is able to closely describe the experimental data, the cooperativity factors were determined assuming that the three Ca^{2+} binding sites are thermodynamically equivalent. This is unlikely given the structural differences of the three sites.[36] Nevertheless, the present analysis unambiguously establishes that the sequential binding of Ca^{2+} to the CRD exhibits cooperativity.

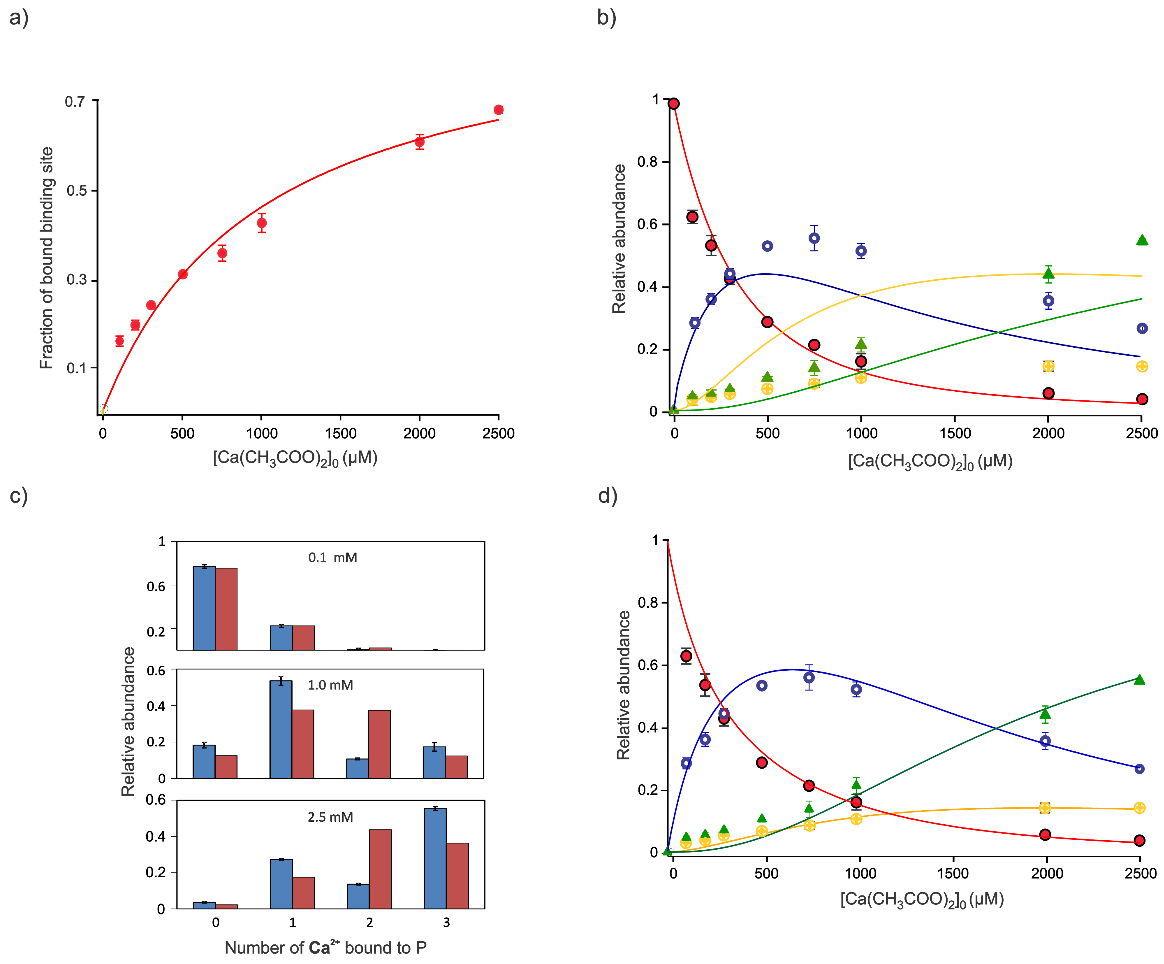

Figure 2.16. Ca^{2+} binding to DC-SIGN CRD. (a) Plot of concentration-dependent fraction (*F*s) of CRD calcium-bound binding sites measured by ESI-MS for aqueous ammonium acetate solutions (200 mM, pH 7.4) of CRD (3 μM) and Ca^{2+} (0.1 – 2.5 mM). Solid curve ($K_{d,intrin}$ of 1.0 mM) represents best fit obtained using Eq. 4. (b) Plot of concentration-dependent fractional abundances of free and Ca^{2+}-bound CRD species measured by ESI-MS (0 Ca^{2+} - red; 1 Ca^{2+} CRD - blue; 2 Ca^{2+} CRD - yellow; 3 Ca^{2+} CRD - green). The solid curves are the theoretical values expected for three equivalent and independent binding sites and $K_{d,intrin}$ of 1.0 mM. (c) Fractional abundances of free and Ca^{2+}-bound CRD species measured by ESI-MS (blue) and calculated assuming three equivalent and independent binding sites with $K_{d,intrin}$ of 1.0 mM (red). (d) Plot of concentration-dependent fractional abundances of free and Ca^{2+}-bound CRD species measured by ESI-MS. The solid curves are the theoretical values expected for three equivalent (0.84 mM) but dependent binding sites (6 (α) and 0.25 (β)). Error bars correspond to one standard deviation.

2.4.4.2 L3–CRD

Binding measurements were next performed on aqueous solutions (200 mM ammonium acetate, pH 7.4, 25 °C) of CRD (1 μM) and **L3** (from 100 μM to 500 μM) in the absence and presence of $Ca(CH_3COO)_2$, at concentrations ranging from 1 mM to 2.5 mM (Figure 2.17). In the absence of Ca^{2+}, little to no specific binding of **L3** to CRD was detected, even at 500 μM (Figure 2.17). This finding is consistent with Ca^{2+} being indispensable to glycan binding by DC SIGN.[38-43] In presence of $Ca(CH_3COO)_2$, **L3** binding to CRD was evident (Figure 2.17) and the relative abundance of the ligand-bound form increased with concentration, *vide infra*. Using the P_{ref} method, the mass spectra was corrected for non-specific Ca^{2+} binding and the resulting distributions are shown in Figure 2.18. Notably, the **L3** complex was found predominantly associated with CRD bound to three (3) Ca^{2+}. Taken on its own, this observation, which is consistent with reported crystallographic data, suggest that **L3** binds preferentially to CRD with fully-occupied Ca^{2+} binding sites.[38,39,43] However, at a given concentration of $Ca(CH_3COO)_2$, the distribution of Ca^{2+} bound to free CRD is found to more closely resemble that of **L3**-bound CRD than the equilibrium distribution observed in the absence of **L3** (Figure 2.14). This remarkable finding implies that glycan binding, in fact, enhances Ca^{2+} interaction with CRD. These results further indicate that the Ca^{2+} dissociation kinetics (from CRD) are slow compared to the **L3** on-off kinetics. However, **L3** binding is also found to exhibit a dependence on $Ca(CH_3COO)_2$ concentration. This is illustrated in Figure 2.19, where the ligand concentration dependence of the fraction of **L3**-bound CRD is shown for three different $Ca(CH_3COO)_2$ concentrations. From fitting (Eq. 4), the K_d (Table 2.2) was found to decrease from 9.4 ± 3.8 mM (1 mM Ca^{2+}) to 3.7 ± 0.8 mM (2.5 mM Ca^{2+}). Importantly, the affinity measured at 2.5 mM $Ca(CH_3COO)_2$ approaches the reported value (2.3 ± 0.6 mM), which was measured in 4 mM $CaCl_2$.[43]

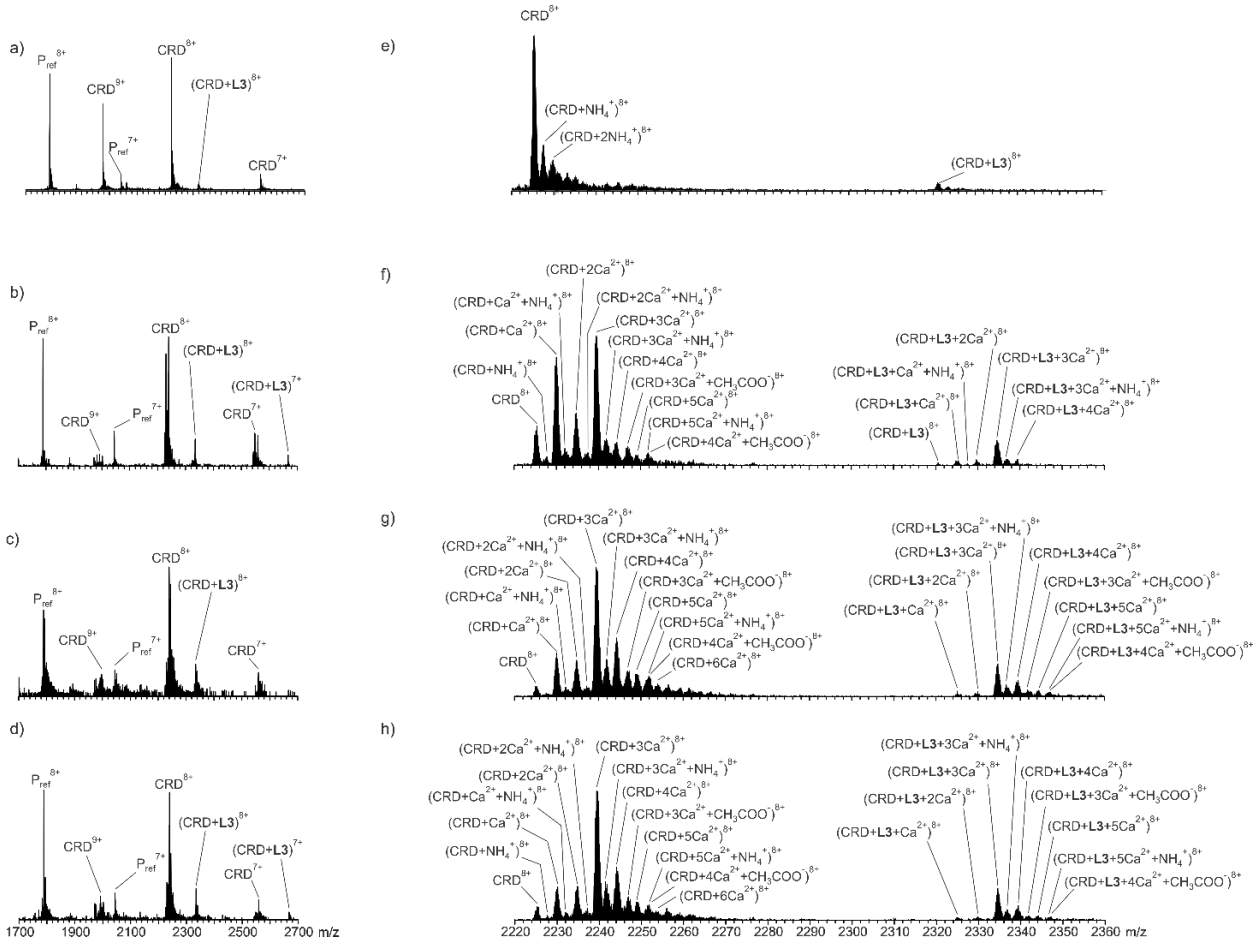

Figure 2.17. Representative ESI mass spectra acquired in positive ion mode for aqueous ammonium acetate solutions (200 mM, pH 7.4) of DC-SIGN CRD (1 μM), **L3** (500 μM), P_{ref} (6 μM) and $Ca(CH_3COO)_2$ at (a) 0 mM, (b) 1.0 mM, (c) 2.0 mM, (d) 2.5 mM $Ca(CH_3COO)_2$. (e)-(h) Expanded regions of the mass spectra ((a)-(d)) corresponding to the 8+ charge states of free and **L3**-bound CRD.

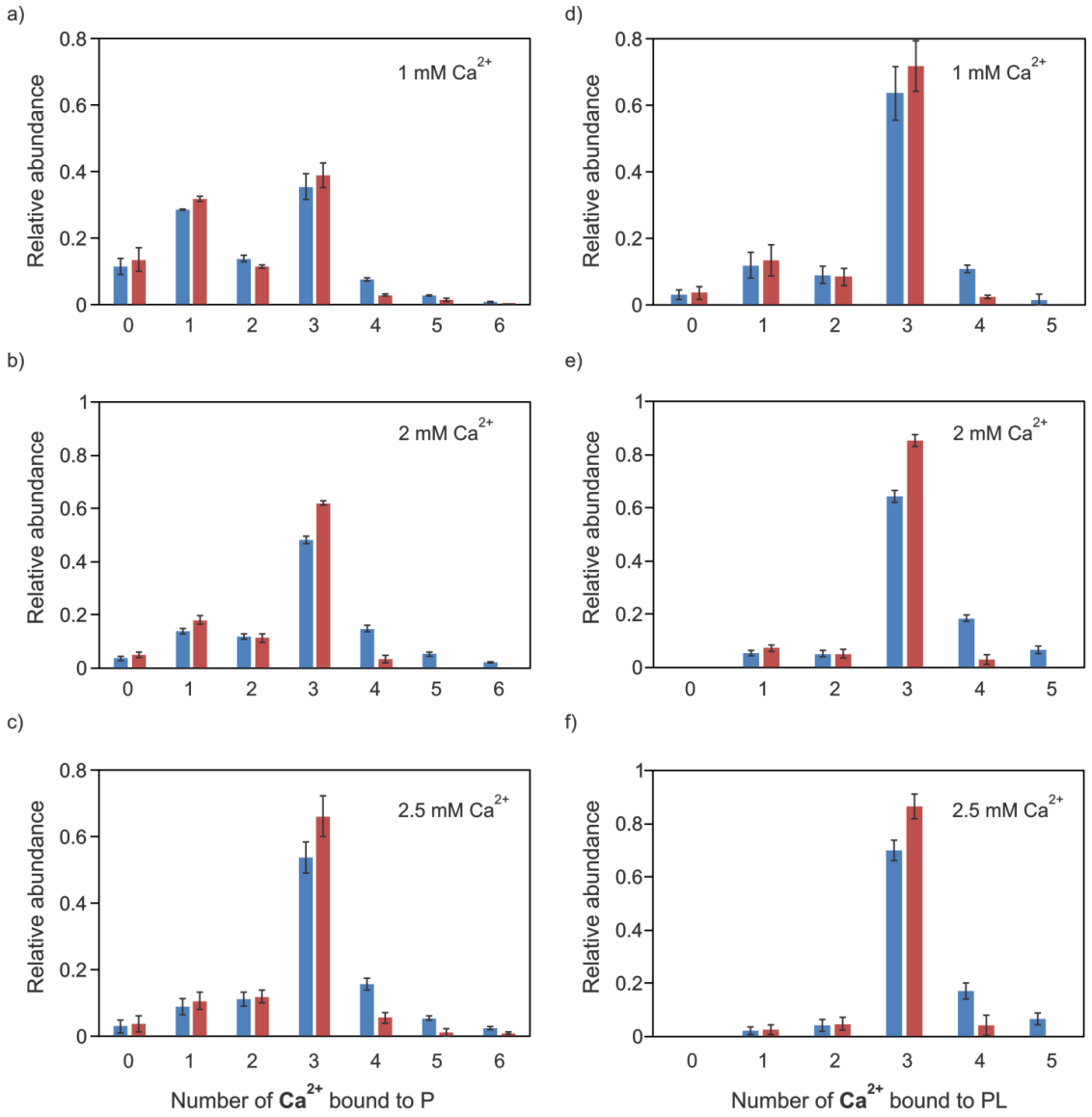

Figure 2.18. Distributions of Ca^{2+} bound to DC-SIGN CRD-**L3** measured by ESI-MS performed with submicron emitters on aqueous ammonium acetate solutions (200 mM, pH 7.4) of CRD (1 μM), P_{ref} (6 μM), **L3** (500 μM) and $Ca(CH_3COO)_2$ at (a) 1.0 mM, (b) 2.0 mM, (c) 2.5 mM. (a)-(c) distribution of Ca^{2+} bound to CRD; (d)-(f) distribution of Ca^{2+} bound to CRD-**L3**. Blue bars are the distribution before correction for non-specific binding. Red bars are the distribution after correction for non-specific binding. The error bars correspond to one standard deviation. Relative abundances were calculated from the spectra shown in Figure 2.17.

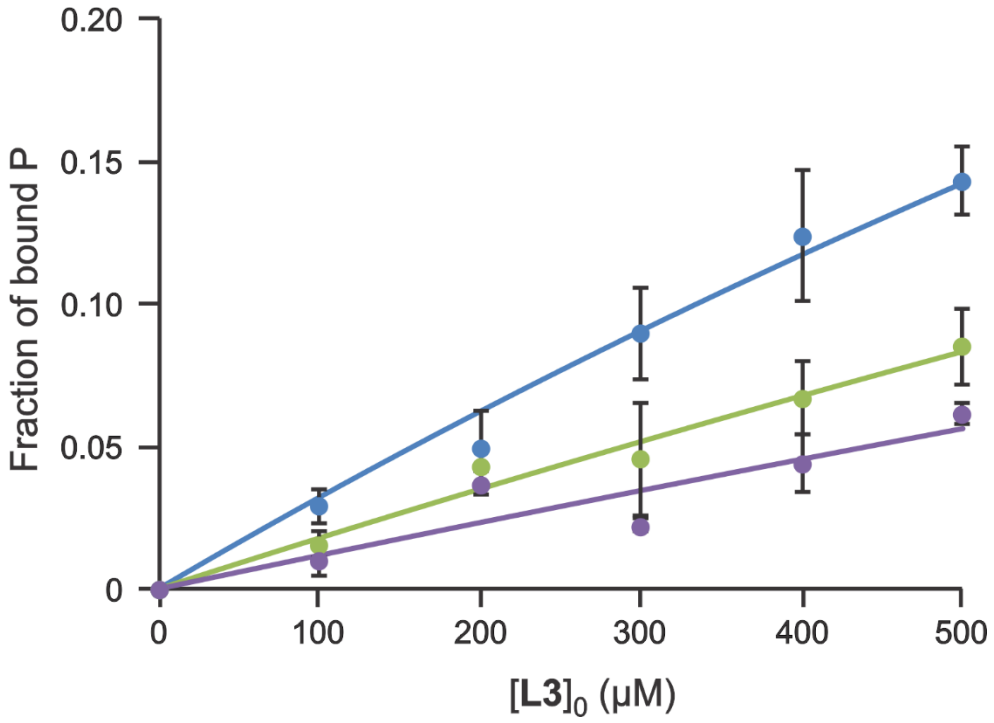

Figure 2.19. Plots of fraction (*F*) of ligand (**L3**)-bound versus initial **L3** concentration measured by ESI-MS performed with submicron emitters on aqueous ammonium acetate solutions (200 mM, pH 7.4) of CRD (1 μM), **L3** (100 - 500 μM) and $Ca(CH_3COO)_2$ (1.0 mM (purple), 2.0 mM (green) and 2.5 mM (blue)). The error bars correspond to one standard deviation.

2.4.5 Quantifying labile GBP–glycan complexes

The reduction in non-specific glycan binding achieved with the submicron emitters not only enables the quantification of low affinity glycan–GBP complexes by ESI-MS but also provides a straightforward solution to the challenge of quantifying labile (prone to in-source dissociation) interactions by allowing ESI-MS measurements to be performed at ligand concentrations that achieve near saturation of the binding site. Under these conditions, the fraction of ligand-bound GBP detected will reflect the extent to which the gaseous complex ions undergo dissociation in the ion source. By establishing the fraction of complex that survives, the affinity can be reliably determined.

The interaction between hGal-3C and lactose (**L4**) served as a model system to demonstrate the application of this approach to account for in-source ion dissociation. A K_d of

93.5 ± 9.1 μM, measured by ITC in PBS (pH 7.4, 25 °C), has been reported.[44] Binding measurements were performed with submicron emitters on aqueous ammonium acetate solutions (200 mM, pH 7.4) of hGal-3C (2 μM), P_{ref} (1.5 μM) and **L4** at concentrations ranging from 20 μM to 1.0 mM. At the highest ligand concentrations tested, non-specific association of **L4** to P_{ref} was negligible, <2% of P_{ref} signal (Figure 2.20). Shown in Figure 2.21 is the apparent fractional abundance of **L4**-bound hGal-3C versus initial ligand concentration and the best fit obtained using Eq. 16. Notably, the fraction of bound protein approaches a limiting value of ~0.37, indicating that almost two-thirds of the complex undergoes dissociation in the ion source (Figure 2.21). Fitting Eq. 16 to experimental data gives a K_d of 192 ± 36 μM, which is in reasonable agreement with the reported value,[44] and a d_f of 0.63 ± 0.02.

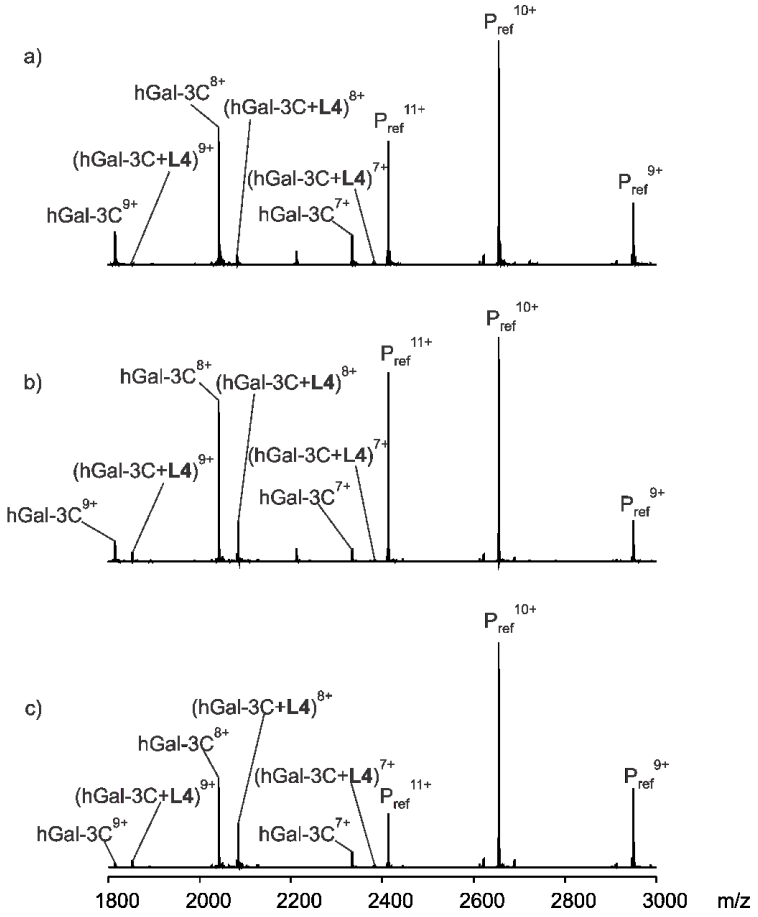

Figure 2.20. Representative ESI mass spectra acquired with submicron emitters in positive ion mode for aqueous ammonium acetate solutions (200 mM, pH 7.4) of hGal-3C (2 μM), P_{ref} (1.5 μM) and **L4** at (a) 100 μM, (b) 400 μM and (c) 1000 μM.

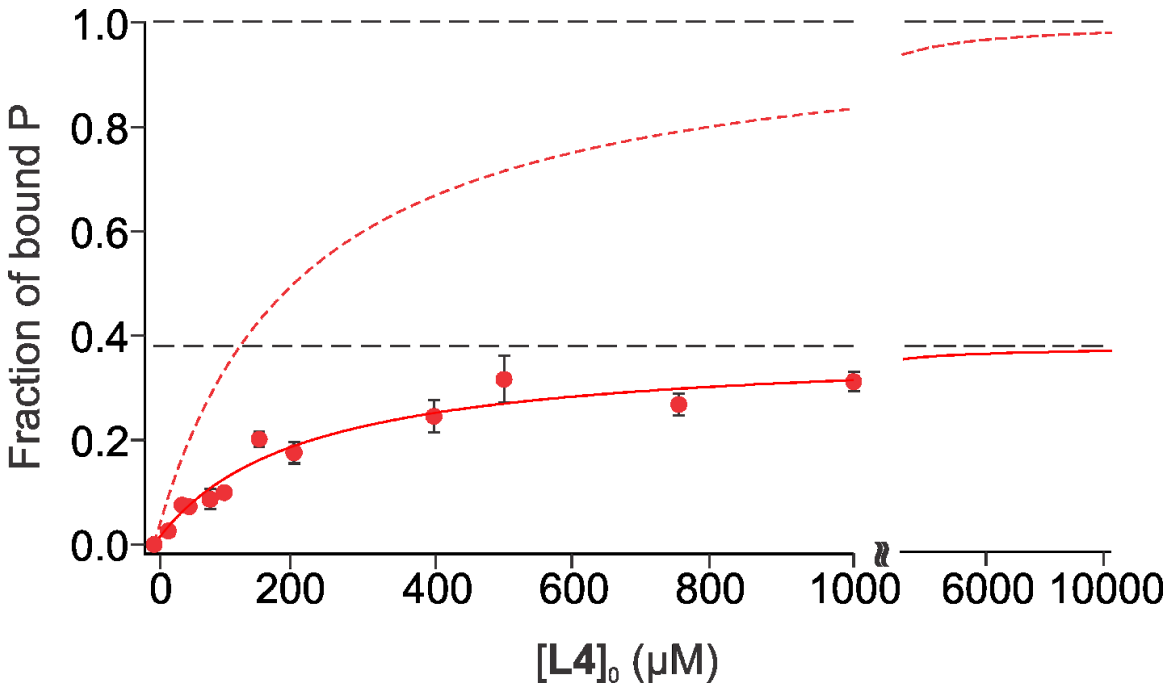

Figure 2.21. Plot of fraction of ligand (**L4**)-bound hGal-3C measured by ESI-MS in positive ion mode for 200 mM aqueous ammonium acetate solutions (pH 7.4, 25 ºC) of hGal-3C (2 μM) and **L4** (20 μM – 1.0 mM). The red solid circles are the fractional abundances determined directly by ESI-MS; the red solid curve is the best fit of Eq. 16 to these data. The red dashed curve is the expected values calculated using the K_d obtained from the best fit of Eq. 16.

Table 2.1. Summary of types and sizes of submicron emitters reported in literature.

I.D. (nm)	Material	Type-based capillary puller	Imaging technique	Reference
1000	BCG [a]	filament	Optical microscopy	S5
37-70	Quartz	laser	STEM [b]	S6
600	BCG [a]	filament	SEM [c]	S7
250	BCG [a]	filament	SEM [c]	S8
80-120	Quartz	laser	STEM [b]	S9
50	BCG [a]	filament	HIM [e]	Here

a. BCG ≡ borosilicate glass. b. STEM ≡ scanning transmission electron microscopy. c. SEM ≡ scanning electron microscopy. d. HIM ≡ helium ion microscopy.

Table 2.2. Summary of dissociation constants (K_d) of GBP-glycan interactions measured by ESI-MS performed using submicron emitters. [a]

GBP	Ligand	Current study (K_d, mM)	ITC/literature (K_d, mM)
Lyz	**L1**	0.0065 ± 0.0009 [a]	0.0068 ± 0.0002 [b]
P_2^{Saga}	**L2**	1.89 ± 0.01 ($K_{d,1}$) [c] 3.70 ± 0.02 ($K_{d,2}$) [c]	1.85 ± 0.01 ($K_{d,1}$) [d] 6.25 ± 0.03 ($K_{d,2}$) [d]
DC-SIGN CRD	**L3**	3.7 ± 0.8 (2.5 mM Ca^{2+}) [e] 6.2 ± 3.0 (2.0 mM Ca^{2+}) [e] 9.4 ± 3.8 (1.0 mM Ca^{2+}) [e]	2.3 ± 0.6 (4 mM Ca^{2+}) [f]
hGal-3C	**L4**	0.192 ± 0.036 [g]	0.093 ± 0.009 [h]

a. Measured in 200 mM aqueous ammonium acetate (pH 7.2, 25 ºC).
b. Measured in present study using ITC; performed in 200 mM aqueous ammonium acetate (pH 7.2, 25 ºC).
c. Measured in 200 mM aqueous ammonium acetate (pH 7.4, 25 ºC).
d. Value taken from reference 6; measurements performed in 300 aqueous mM ammonium acetate at pH 7.0 and 25 °C.
e. Measured in 200 mM aqueous ammonium acetate (pH 7.4, 25 ºC).

f. Value taken from reference 41; measurements performed in 20 mM Tris-d11, 150 mM NaCl, 4 mM $CaCl_2$, 2 mM DTT-d10 solution (pH 8, 37 °C).
g. Measured in 200 mM aqueous ammonium acetate (pH 7.4, 25 °C).
h. Value taken from reference 43; measurements performed in PBS solution (pH 7.4, 25 °C).

2.5 Conclusions

Interactions between glycans and GBPs mediate many biological processes important to human health and implicated in diseases and infections. However, because the affinities of monovalent glycan–GBP complexes are generally weak, the glycan binding properties of most GBPs are not well established. The results of this study highlight how ESI-MS, implemented with submicron emitters, enables the quantification of low and even ultra-low affinity glycan–GBP interactions. The small size of the droplets produced from the submicron emitters (i.d. ~50 nm) used in the current work (estimated to be ~5 nm) significantly reduces or completely eliminates the formation of non-specific glycan–GBP binding during the ESI process at high (~mM) glycan concentrations. Consequently, interactions with K_d as high as ~5 mM can be measured directly from the mass spectrum.

The general suppression of non-specific adducts achieved with these tips also allowed, for the first time, ESI-MS glycan affinity measurements to be performed on C-type lectins. At a physiologically-relevant calcium ion concentration, the extent of non-specific Ca^{2+} adduct formation was dramatically suppressed, allowing glycan affinities, and the influence of Ca^{2+} thereon, to be calculated from the mass spectrum (albeit with the aid of the reference protein method). Measurements performed on the CRD of DC-SIGN confirmed the presence of three Ca^{2+} binding sites and revealed that Ca^{2+} binding is cooperative in nature. Moreover, while binding was shown to be dependent on Ca^{2+}, glycan binding to CRD was shown to promote

saturation of Ca^{2+} binding sites. These novel insights into the interplay between ligand and Ca^{2+} binding to DC-SIGN showcase the tremendous potential of ESI-MS for elucidating the binding properties of C-type lectins, an important class of immune lectins. The suppression of non-specific glycan binding achieved with the submicron emitters also enables the quantification of labile (prone to in-source dissociation) glycan–GBP interactions by allowing ESI-MS measurements to be performed at ligand concentrations that achieve near saturation of the binding site in solution. Under these conditions, the limiting fractional occupancy directly informs on the extent of complex undergoing in-source dissociation.

Finally, it should be noted that, although the focus of the present study was glycan–GBP interactions, the findings of this work have relevance for other classes of low affinity and labile biomolecular complexes. In particular, we expect the use of submicron emitters to greatly facilitate the application of ESI-MS to many therapeutically relevant interactions, such as drug–protein complexes, and to fragment based library screening for drug lead discovery, which can't be performed directly using standard ESI emitters due to challenges associated with non-specific binding and in-source dissociation.[45]

2.6 References

(1) Varki, A. Biological Roles of Glycans. *Glycobiology* **2017**, *27*, 3–49.

(2) Li, J.; Fan, X.; Kitova, E. N.; Zou, C.; Cairo, C. W.; Eugenio, L.; Ng, K. K. S.; Xiong, Z. J.; Privé, G. G.; Klassen, J. S. Screening Glycolipids Against Proteins in Vitro Using Picodiscs and Catch-and-Release Electrospray Ionization-Mass Spectrometry. *Anal. Chem*. **2016**, *88*, 4742–4750.

(3) Shams-Ud-Doha, K.; Kitova, E. N.; Kitov, P. I.; St-Pierre, Y.; Klassen, J. S. Human Milk Oligosaccharide Specificities of Human Galectins. Comparison of Electrospray Ionization Mass Spectrometry and Glycan Microarray Screening Results. *Anal. Chem*. **2017**, *89*, 4914–4921.

(4) Fiege, B.; Rademacher, C.; Cartmell, J.; Kitov, P. I.; Parra, F.; Peters, T. Molecular Details of the Recognition of Blood Group Antigens by a Human Norovirus as Determined by STD NMR Spectroscopy. *Angew. Chemie - Int. Ed*. **2012**, *51*, 928–932.

(5) Mallagaray, A.; Lockhauserbäumer, J.; Hansman, G.; Uetrecht, C.; Peters, T. Attachment of Norovirus to Histo Blood Group Antigens: A Cooperative Multistep Process. *Angew. Chemie - Int. Ed*. **2015**, *54*, 12014–12019.

(6) Han, L.; Zheng, R.; Richards, M. R.; Tan, M.; Kitova, E. N.; Jiang, X.; Klassen, J. S. Quantifying the Binding Stoichiometry and Affinity of Histo-Blood Group Antigen Oligosaccharides for Human Noroviruses. *Glycobiology* **2018**, *28*, 488–498.

(7) Syedbasha, M.; Linnik, J.; Santer, D.; O'Shea, D.; Barakat, K.; Joyce, M.; Khanna, N.; Lorne Tyrrell, D.; Houghton, M.; Egli, A. An ELISA Based Binding and Competition Method to Rapidly Determine Ligand-Receptor Interactions. *J. Vis. Exp*. **2016**, *109*, 1–10.

(8) Safina, G. Application of Surface Plasmon Resonance for the Detection of Carbohydrates, Glycoconjugates, and Measurement of the Carbohydrate-Specific Interactions: A Comparison with Conventional Analytical Techniques. A Critical Review. *Anal. Chim. Acta* **2012**, *712*, 9–29.

(9) Helmerhorst, E.; Chandler, D. J.; Nussio, M.; Mamotte, C. D. Real-time and Label-free Bio-sensing of Molecular Interactions by Surface Plasmon Resonance: A Laboratory

Medicine Perspective. *Clin*. *Biochem*. *Rev*. **2012**, *33*, 161–173.

(10) Han, L.; Tan, M.; Xia, M.; Kitova, E. N.; Jiang, X.; Klassen, J. S. Gangliosides are Ligands for Human Noroviruses. *J*. *Am*. *Chem*. *Soc*. **2014**, *136*, 12631–12637.

(11) El-Hawiet, A.; Kitova, E. N.; Klassen, J. S. Quantifying Carbohydrate-Protein Interactions by Electrospray Ionization Mass Spectrometry Analysis. *Biochemistry* **2012**, *51*, 4244–4253.

(12) Wang, Y.; Park, H.; Lin, H.; Kitova, E. N.; Klassen, J. S. Multipronged ESI-MS Approach for Studying Glycan-Binding Protein Interactions with Glycoproteins. *Anal*. *Chem*. **2019**, *91*, 2140–2147.

(13) Wang, W.; Kitova, E. N.; Klassen, J. S. Influence of Solution and Gas Phase Processes on Protein-Carbohydrate Binding Affinities Determined by Nanoelectrospray Fourier Transform Ion Cyclotron Resonance Mass Spectrometry. *Anal*. *Chem*. **2003**, *75*, 4945–4955.

(14) Yao, Y.; Shams-ud-doha, K.; Daneshfar, R.; Kitova, E. N.; Klassen, J. S. Quantifying Protein-Carbohydrate Interactions using Liquid Sample Desorption Electrospray Ionization Mass Spectrometry. *J*. *Am*. *Soc*. *Mass Spectrom*. **2014**, *26*, 98–106.

(15) Wang, W.; Kitova, E. N.; Klassen, J. S. Nonspecific Protein-Carbohydrate Complexes Produced by Nanoelectrospray Ionization. Factors Influencing their Formation and Stability. *Anal*. *Chem*. **2005**, *77*, 3060–3071.

(16) Kitova, E. N.; El-Hawiet, A.; Schnier, P. D.; Klassen, J. S. Reliable Determinations of Protein-Ligand Interactions by Direct ESI-MS Measurements. Are We There Yet? *J*. *Am*. *Soc*. *Mass Spectrom*. **2012**, *23*, 431–441.

(17) Kebarle, P.; Verkcerk, U. H. Electrospray: From Ions in Solution to Ions in the Gas Phase, What We Know. *Mass Spectrom*. *Rev*. **2009**, *28*, 898–917.

(18) Sun, J.; Kitova, E. N.; Wang, W.; Klassen, J. S. Method for Distinguishing Specific from Nonspecific Protein-Ligand Complexes in Nanoelectrospray Ionization Mass Spectrometry. *Anal*. *Chem*. **2006**, *78*, 3010–3018.

(19) Shimon, L.; Sharon, M.; Horovitz, A. A Method for Removing Effects of Nonspecific Binding on the Distribution of Binding Stoichiometries: Application to Mass Spectroscopy Data. *Biophys*. *J*. **2010**, *99*, 1645–1649.

(20) Schmidt, A.; Karas, M.; Dülcks, T. Effect of Different Solution Flow Rates on Analyte Ion

Signals in nano-ESI MS, or: When does ESI turn into nano-ESI? *J. Am. Soc. Mass Spectrom*. **2003**, *14*, 492–500.

(21) Davidson, K. L.; Oberreit, D. R.; Hogan Jr., C. J.; Bush, M. F. Nonspecific Aggregation in Native Electrokinetic Nanoelectrospray Ionization. *Int. J. Mass Spectrom*. **2017**, *420*, 35–42.

(22) Hollerbach, A.; Logsdon, D.; Iyer, K.; Li, A.; Schaber, J. A.; Graham Cooks, R. Sizing sub-Diffraction Limit Electrosprayed Droplets by Structured Illumination Microscopy. *Analyst* **2018**, *143*, 232–240.

(23) Li, Y.; Cole, R. B. Shifts in Peptide and Protein Charge State Distributions with Varying Spray Tip Orifice Diameter in Nanoelectrospray Fourier Transform Ion Cyclotron Resonance Mass Spectrometry. *Anal. Chem*. **2003**, *75*, 5739–5746.

(24) Mortensen, D. N.; Williams, E. R. Ultrafast (1 ms) Mixing and Fast Protein Folding in Nanodrops Monitored by Mass Spectrometry. *J. Am. Chem. Soc*. **2016**, *138*, 3453–3460.

(25) Xia, Z.; Williams, E. R. Effect of Droplet Lifetime on Where Ions Are Formed in Electrospray Ionization. *Analyst* **2019**, *144*, 237–248.

(26) Yuill, E. M.; Sa, N.; Ray, S. J.; Hieftje, G. M.; Baker, L. A. Electrospray Ionization from Nanopipette Emitters with Tip Diameters of Less than 100 nm. *Anal. Chem*. **2013**, *85*, 8498–8502.

(27) Panczyk, E. M.; Gilbert, J. D.; Jagdale, G. S.; Stiving, A. Q.; Baker, L. A.; Wysocki, V. H. Ion Mobility and Surface Collisions: Submicrometer Capillaries Can Produce Native-like Protein Complexes. *Anal. Chem*. **2020**, *92*, 2460–2467.

(28) Susa, A. C.; Xia, Z.; Williams, E. R. Small Emitter Tips for Native Mass Spectrometry of Proteins and Protein Complexes from Nonvolatile Buffers That Mimic the Intracellular Environment. *Anal. Chem*. **2017**, *89*, 3116–3122.

(29) Susa, A. C.; Xia, Z.; Williams, E. R. Native Mass Spectrometry from Common Buffers with Salts That Mimic the Extracellular Environment. *Angew. Chemie - Int. Ed*. **2017**, *56*, 7912–7915.

(30) Susa, A. C.; Lippens, J. L.; Xia, Z.; Loo, J. A.; Campuzano, I. D. G.; Williams, E. R. Submicrometer Emitter ESI Tips for Native Mass Spectrometry of Membrane Proteins in Ionic and Nonionic Detergents. *J. Am. Soc. Mass Spectrom*. **2018**, *29*, 203–206.

(31) Nguyen, G. T. H.; Tran, T. N.; Podgorski, M. N.; Bell, S. G.; Supuran, C. T.; Donald, W.

A. Nanoscale Ion Emitters in Native Mass Spectrometry for Measuring Ligand-Protein Binding Affinities. *ACS Cent. Sci.* **2019**, *5*, 308–318.

(32) Mitchell, D. A.; Fadden, A. J.; Drickamer, K. A Novel Mechanism of Carbohydrate Recognition by the C-Type Lectins DC-SIGN and DC-SIGNR. *J. Biol. Chem.* **2001**, *276*, 28939–28945.

(33) Kitov, P. I.; Han, L.; Kitova, E. N.; Klassen, J. S. Sliding Window Adduct Removal Method (SWARM) for Enhanced Electrospray Ionization Mass Spectrometry Binding Data. *J. Am. Soc. Mass Spectrom*, **2019**, *30*, 1446–1454.

(34) Pöhlmann, S.; Baribaud, F.; Lee, B.; Leslie, G. J.; Sanchez, M. D.; Hiebenthal-Millow, K.; Münch, J.; Kirchhoff, F.; Doms, R. W. DC-SIGN Interactions with Human Immunodeficiency Virus Type 1 and 2 and Simian Immunodeficiency Virus. *J. Virol.* **2001**, *75*, 4664–4672.

(35) Van Kooyk, Y.; Geijtenbeek, T. B. H. Escape Mechanism for Pathogens. *Nat. Rev. Immunol.* **2003**, *3*, 697–709.

(36) Feinberg, H.; Guo, Y.; Mitchell, D. A.; Drickamer, K.; Weis, W. I. Extended Neck Regions Stabilize Tetramers of the Receptors DC-SIGN and DC-SIGNR. *J. Biol. Chem.* **2005**, *280*, 1327–1335.

(37) Noll, A. J.; Yu, Y.; Lasanajak, Y.; Duska-McEwen, G.; Buck, R. H.; Smith, D. F.; Cummings, R. D. Human DC-SIGN Binds Specific Human Milk Glycans. *Biochem. J.* **2016**, *473*, 1343–1353.

(38) Feinberg, H.; Mitchell, D. A.; Drickamer, K.; Weis, W. I. Structural Basis for Selective Recognition of Oligosaccharides by DC-SIGN and DC-SIGNR. *Science* **2001**, *294*, 2163–2166.

(39) Guo, Y.; Feinberg, H.; Conroy, E.; Mitchell, D. A.; Alvarez, R.; Blixt, O.; Taylor, M. E.; Weis, W. I.; Drickamer, K. Structural Basis for Distinct Ligand-Binding and Targeting Properties of the Receptors DC-SIGN and DC-SIGNR. *Nat. Struct. Mol. Biol.* **2004**, *11*, 591–598.

(40) Snyder, G. A.; Colonna, M.; Sun, P. D. The Structure of DC-SIGNR with a Portion of Its Repeat Domain Lends Insights to Modeling of the Receptor Tetramer. *J. Mol. Biol.* **2005**, *347*, 979–989.

(41) Holla, A.; Skerra, A. Comparative Analysis Reveals Selective Recognition of Glycans by

the Dendritic Cell Receptors DC-SIGN and Langerin. *Protein Eng*. *Des*. *Sel*. **2011**, *24*, 659–669.

(42) Van Liempt, E.; Bank, C. M. C.; Mehta, P.; García-Vallejo, J. J.; Kawar, Z. S.; Geyer, R.; Alvarez, R. A.; Cummings, R. D.; Van Kooyk, Y.; Van Die, I. Specificity of DC-SIGN for mannose- and fucose-containing glycans. *FEBS Letters* **2006**, *580*, 6123-6131

(43) Valverde, P.; Delgado, S.; Martínez, J. D.; Vendeville, J. B.; Malassis, J.; Linclau, B.; Reichardt, N. C.; Cañada, F. J.; Jiménez-Barbero, J.; Ardá, A. Molecular Insights into DC-SIGN Binding to Self-Antigens: The Interaction with the Blood Group A/B Antigens. *ACS Chem*. *Biol*. **2019**, *14*, 1660–1671.

(44) Sindrewicz, P.; Li, X.; Yates, E. A.; Turnbull, J. E.; Lian, L.-Y.; Yu, L.-G. Intrinsic Tryptophan Fluorescence Spectroscopy Reliably Determines Galectin-Ligand Interactions. *Sci*. *Rep*. **2019**, *9*, 11851.

(45) Li, Q. Application of Fragment-Based Drug Discovery to Versatile Targets. *Front. Mol. Biosci.* **2020**, *7*, 180.

Chapter 3

Time-resolved neuraminidase-aided ESI approach for the relative quantification of α2,3-N-acetylneuraminic acid on PSA

3.1 Introduction

Cancer is a major public health concern worldwide and it is the second leading cause of death in the United States.[1] Among the top five (5) most diagnosed cancers between women and men in the United States, Prostate cancer (PCa) occupies the third place in this list.[1] Currently, serological levels of prostate-specific antigen (PSA) jointly with a digital rectal examination (DRE) are employed as the standard procedure for PCa diagnosis. This procedure was approved in 1994 by the Federal Drug Administration (FDA).[2] PSA, also called human Kallikrein 3 (hK3), is a 28430 Da glycoprotein comprising 237 amino acid residues with an N-glycosylation site at Asn61. Also an O-glycosylation site has been reported at Thr125.[3] PSA is secreted into the lumen of the prostate by epithelial prostatic cells as proPSA (a zymogen of 244 amino acid residues), which is activated through enzymatic digestion by human Kallikrein 2 (hK2) and human Kallikrein 4 (hK4).[4] hK2 and the active form of PSA (hK3) belong to a family of serine proteases, they play an important role in fertilization, these enzymes digest the gel-forming proteins semenogelin I and II, which liquefies seminal plasma and increases the motility of spermatozoa.[5] From now on, the active form of PSA (hK3) will be mentioned as PSA. Truncated forms of proPSA can also be generated by cleavage within the propeptide, these truncated forms of proPSA (e.g. [5-2]proPSA) are inactive. PSA might also undergo proteolysis in the lumen, these forms are inactive as well. All these inactive forms of PSA jointly with PSA are called free PSA (fPSA).[6,7] A fraction of PSA might diffuse into circulation as well, where it is bound by protease inhibitors (mainly alpha 1-antichymotrypsin (ACT), and minor quantities to α2-macroglobulin (A2M) or α1-antitrypsin).[4] 70% to 90% of PSA that enters the peripheral blood circulates as an 80- to 90-kDa complex, this is called complexed PSA.[4]

Basal cells and basement membrane in the prostate are responsible to hold active PSA into the lumen of the prostate, however, loss of the basal cells and disruption of the basement

membrane during PCa development increases the access of PSA, proPSA and truncated forms of proPSA to the bloodstream[4], which turns into an increase of complexed PSA in circulation. PSA test, the standard test for PCa screening in clinical settings, is based on total PSA (tPSA) measurement in circulation, which includes fPSA, hK2 and complexed PSA.[8] A clinically used PSA test uses biotinylated and ruthenium-labeled anti-tPSA mouse monoclonal antibodies (mAbs) to form a sandwich complex (Figure 3.1). Streptavidin-coated paramagnetic microparticles are used to separate PSA-antibody complexes from unbound ruthenium labeled anti-tPSA mouse monoclonal antibodies. A defined voltage is applied and an electrochemiluminescent reaction occurs in the presence of tripropylamine (TPA), resulting in light emission that is quantitated.[9]

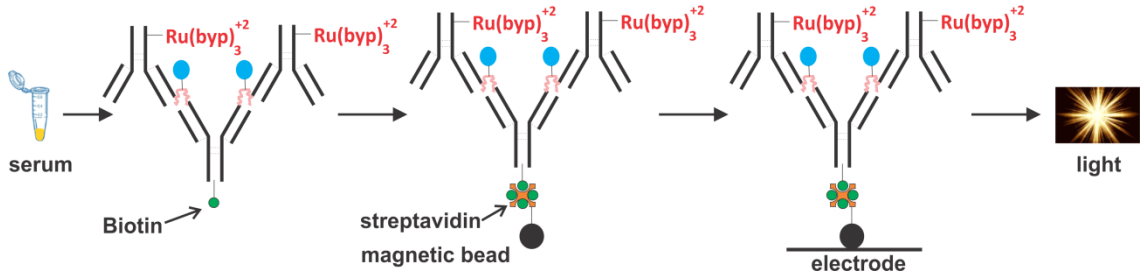

Figure 3.1. Schematic representation of an electrochemiluminescence system (ELECSYS) for the quantification of tPSA. The same scheme is used for the quantification of fPSA, but anti-fPSA mAbs are used instead.

A tPSA level up to 4 ng/mL is considered normal, while over 10 ng/mL is considered high with a 67% probability of advanced disease.[10] A tPSA level in the range of 4-10 ng/mL (so-called the grey zone) is considered intermediate with cancer present in 30-35% of patients (Table 3.1).[10] The disease is confirmed by histopathological analysis (biopsy), which is an invasive procedure with some potential complications, such as bleeding, urinary retention, and life-threatening infection.[8] The reason underlying the deficiency of PSA test to accurately screen for PCa is that PSA is a prostate- and not a PCa-specific biomarker. Benign illnesses of the prostate, such as benign prostate hyperplasia (BPH) and prostatitis, might cause an increase in tPSA levels as well.[2,11-13] As a consequence, overdiagnosis is a major issue with this test, it brings unnecessary concerns and anxiety to patients.[2] Also, treatment due to high tPSA levels might

result in life-altering issues such as incontinence and impotence.[12] Moreover, a normal tPSA level might cause false-negative because a biopsy in 15% of men reveals PCa.[12]

Another concern regarding this test is that serological levels of PSA do not provide information on the aggressiveness of PCa. Only 25% of biopsy with high tPSA levels is PCa, and many patients have clinically insignificant cancer (indolent or non-aggressive cancer), which does not need to be treated.[14] This leads to an increase in false-positive, misdiagnosis and overtreatment of patients.[2,15] To tackle the deficiencies of PSA test, other blood-based methods are available. fPSA test measures fPSA levels in circulation with a similar methodology followed for tPSA but employing anti-fPSA mouse mAbs instead, this test was approved by the FDA in 1998.[6,16] This test compares the ratio of fPSA to tPSA, the percentage decreases during PCa development due to the formation of more complexed PSA, values ≥ 25% are considered normal. However, the fPSA to tPSA ratio as a biomarker has been questioned due to its high false-positive rate in the diagnosis.[17,18] PSA density (PSAD) measures the ratio of tPSA to the volume of the prostate calculated using transrectal ultrasound, values over 0.1 are considered abnormal (although the units should be $ng/mLcm^3$, the results are frequently reported dimensionless).[19] Unfortunately, these methods (fPSA to tPSA ratio and PSAD) do not offer prognostic value.[20] Also, measurement of prostate volume is an invasive, time-consuming procedure.[2,8] Prostate Health Index (PHI) test combines fPSA, tPSA and [-2]proPSA, this test was approved in 2012 by the FDA. This test assesses the risk of aggressive PCa in patients with tPSA levels between 4-10 ng/mL and negative DRE. In this case, higher values mean a higher probability of aggressive PCa.[21] However, its clinical utility has been questioned[22] and there are no published long-term outcome studies associated with the clinical used of PHI test in either predicting development of metastatic disease or demonstrating the safety of deferring biopsy in men with a low PHI test result.[2,8] 4 Kallikrein (4K) score is a non-FDA approved method that measures tPSA, fPSA, intact PSA (PSA with 244 amino acid sequence) and hK2, and takes into consideration clinical information of the patient. The method is intended to assess the risk of aggressive PCa.[13] However, it is not specific enough to distinguish indolent from aggressive PCa.[23,24] Additionally, there are RNA- and genetic-based methods available, but these methods are not widespread because their cost, most insurance companies do not approve these methods and some technical limitations as well, e.g. need of biopsy, lack of optimal cut-off for a positive test result, difficult interpretation, lack of consistency on their prognostic value.[2,8,21,23,25,26] Therefore, non-invasive

biomarkers that can be tested in blood and are capable of distinguishing between indolent and aggressive PCa are required.

Glycosylation is a common post-translational modification of proteins, and the glycosylation patterns of glycoproteins have been found altered during cancer development and progression.[27,28] Common alterations in cancer development are related to overexpression or downregulation of N-acetylneuraminic acid (Neu5Ac) and fucose.[28,29,30]. However, methods to quantify LacdiNAc (GalNAc-GlcNAc) and mannose content on PSA have also been developed.[12] It is also important to mention that regulatory boards have not approved glycan-based biomarkers for the diagnosis or prognosis of PCa. The dominant N-glycans from PSA are fucosylated, sialylated complex N-glycans, and changes in PSA glycosylation pattern has been shown in blood serum from PCa patients compared to PSA from seminal plasma of healthy controls (standard PSA).[11,31,32] Different strategies have been employed for the quantification of α2,3- and α2,6-linked Neu5Ac (Figure 3.2). Yoneyama *et al*.[33] used anti-fPSA mAb conjugated to magnetic particles to extract fPSA from samples, anti-α2,3-linked Neu5Ac mAb (HYB4) makes a sandwich with those glycoforms containing α2,3-linked Neu5Ac. The quantification was performed after adding phycoerythrin (PE)-labeled goat anti-mouse mAb, which was excited with a green laser. They found higher content of α2,3-linked Neu5Ac in PCa patients. Llop *et al*.[32] employed a *Sambucus nigra agglutinin* (SNA) lectin column (which recognizes only α2,6-linked Neu5Ac) to separate α2,6-linked Neu5Ac (bound fraction) from α2,3-linked Neu5Ac (unbound fraction). The quantification of PSA in the bound and unbound fraction is performed following a commercial technology previously described[9], then the ratio of α2,3- over α2,6-linked Neu5Ac is calculated. They detected a significant increase of α2,3-linked Neu5Ac in fPSA of aggressive PCa patients in comparison with BPH and indolent PCa patients. Ishikawa *et al*.[34] quantified the ratio of α2,3- over α2,6-linked Neu5Ac using a "micro-total immunoassay system (μTAS)-based microcapillary electrophoresis". This technology uses a microfluidic system which integrates lectin-aided capillary electrophoresis separation with fluorescence detection of α2,3- and α2,6-linked Neu5Ac on PSA from blood serum. In this assay DNA-labeled anti-tPSA fragment antibody (Fab) forms a sandwich with HiLyte Fluor 647 labeled anti-fPSA to separate PSA from serum, then a voltage is applied and electrophoresis separation is achieved aided by *Maackia amurensis agglutinin* (MAA), which recognizes only α2,3-linked Neu5Ac. Laser induced fluorescence (LIF) is used for detection and quantification of the

isomers. They also found higher content of α2,3-linked Neu5Ac in serum of PCa patients in comparison with BPH patients.

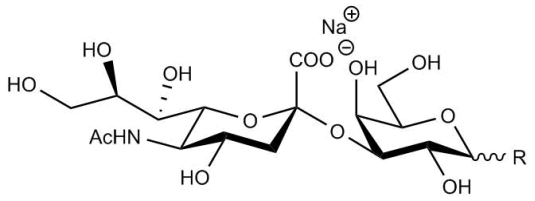

α2,3-linked Neu5Ac bound to Galactose

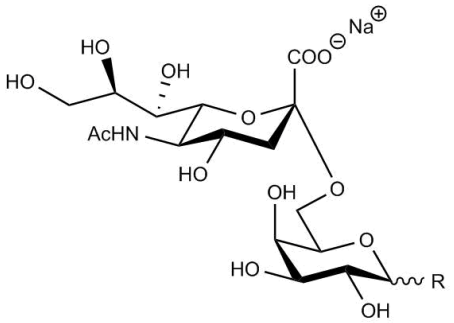

α2,6-linked Neu5Ac bound to galactose

Figure 3.2. Isomers of Neu5Ac bound to galactose (Gal) or N-acetylgalactosamine (GalNAc) in N-glycans on PSA.

Fukushima *et al.*[35] developed a lectin-based assay based on incubation of samples with sepharose-bound *Trichosanthes japonica agglutinin*-II (TJA-II), which recognizes α1-2-fucose (branched fucose). PSA-containing α1-2-fucose was quantified using enzyme-linked immunosorbent assay (ELISA). Higher levels of α1-2-fucose in serum extracted from PCa patients in comparison with BPH patients were detected. Also, expression of fucosyltransferase I (FUT1) which regulates the conjugation of α1-2-fucose to glycoproteins was quantified by polymerase chain reaction (PCR). The gene was found overexpressed. Llop *et al*.[32] developed a lectin-based assay to quantify the content of core fucose on fPSA. In this assay serum PSA was released from ACT-PSA complex using ethanolamine, then fPSA is purified with anti-fPSA mAb conjugated to microplates. The content of core fucose is quantitated using an enzyme-linked lectin assay (ELLA). Biotinylated *Pholiota squarrosa lectin* (PhoSL), which recognizes only α1-6-fucose (core fucose), makes a sandwich with the immunoprecitated fPSA, then a streptavidin-horseradish peroxidase conjugate is added for chemifluorescent detection. They found a significant decrease of core fucose in fPSA of aggressive PCa patients in comparison with BPH and indolent PCa patients. Regarding LacdiNAc content on PSA, Yoneyama *et al.*[36] developed an automated lectin-based immunoassay using *Wisteria floribunda* agglutinin (WFA) for PCa diagnosis and prognosis. In this method anti-PSA mAb was immobilized on a gold thin

film, the sample was applied in a flow system and fluorescently labeled lectin-recognizing LacdiNAc was injected over the surface forming a sandwich. The signal was read as fluorescence intensity with a surface plasmon field-enhanced fluorescence spectrometer.[12] A higher content of LacdiNAc was found in PCa patients in comparison with BPH patients. On the other hand, a decreased mannose level with PCa development has also been reported. Ohyama *et al.*[37] employed a lectin-based assay in which samples were incubated with sepharose-bound Concanavalin A, the content of fPSA in lectin-bound fraction was found to be lower in PCa patients in comparison with BPH patients. As noted, the dominant technology for PSA glycoprofiling is ELISA or other related techniques (ELLA, ELECSYS), which provide simplicity, possibility of assay miniaturization and then point-of-care analysis, high sensitivity and minute sample volumes.[38] However, these technologies present drawbacks such as need for labeling, external standards, chemical pre-treatment of the sample, limited repertoire of glycan structural elements recognized by lectins and antibodies, antibody cross reactivity, and lectins with low affinity for carbohydrates.[12,38]

N-glycan analysis by hydrophilic interaction liquid chromatography (HILIC) with fluorescence detection has also been used for the identification and quantification of carbohydrates on PSA. Recently, a study aiming at the characterization and quantification of PSA glycoforms in aggressive PCa reported an increase in core fucosylated biantennary α2,3-disialylated, non-core fucosylated biantennary α2,3-monosialylated, core fucosylated biantennary GalNAc α2,3-/α2,6-disialylated, and core fucosylated biantennary GalNAc α2,6-monosialylated compared to standard PSA (PSA from seminal plasma of healthy individuals).[7] However, N-glycan analysis is not suitable for routine clinical diagnosis due to the high amount of PSA needed for the analysis (over 300 ng/mL to obtain micrograms of PSA per patient).[7] Another option are medium-bottom and bottom-up approaches, in which MS is used for the analysis of glycopeptides and glycans, respectively. A quantitative MS-based approach reported upregulation of LacdiNAc in PCa patients compared to BPH patients.[40] In this assay, 100 µL of serum PSA is purified by immunoprecipitation, the extracted PSA is digested and the glycopeptides enriched, the concentrated glycopeptides are then injected in a triple quadruple MS for fragmentation and monitoring of oxonium ions. However, this strategy is prone to high variability between laboratories due to the optimization of collisional induced dissociation (CID)

parameters. In general these approaches require a time-consuming sample preparation and high expertise for data analysis.[38,39,40]

Alternatively, the analysis of glycoforms by native ESI-MS combined with enzymatic digestions opens up a new avenue in the characterization of glycosylated proteins. This approach is fast and requires little sample preparation as intact glycoprotein is analyzed in its native form.[41,42] In this work, we explore native ESI-MS for collecting time-resolved data of the enzymatic digestion of α2,3-linked Neu5Ac on PSA glycoforms to indirectly measure the ratio of α2,3- to α2,6-linked Neu5Ac. This approach does not neither require labeling nor external standard for quantification. The glycoprotein is analyzed in its native form after extraction from blood serum, therefore, it does not require any further sample treatment. The relative quantification of α2,3- to α2,6-linked Neu5Ac could serve as a diagnostic tool for PCa.

3.2 Experimental

3.2.1 Materials

3.2.1.1 Carbohydrates

The structures of the glycans used in this study are shown in Figure 3.3. Neu5Acα2-6Galβ1-4Glc-S1 (CS_{6SL}^{S1}, MW 1395.55 Da) and Neu5Acα2-3Galβ1-4GlcNAc-S2 (CS_{3SLNAc}^{S2}, MW 1534.59 Da) were synthesized in-house and reported previously as CUPRA substrates (CS).[43] S1 and S2 represent different linkers to each oligosaccharide, however, the linkers do not affect neuraminidase activity over these substrates.[43] N-acetyl-D-neuraminic acid-1,2,3-$^{13}C_3$ (Neu5Ac-$^{13}C_3$), Internal Standard (**IS**) (MW 312.25 Da) was purchased from Omicron Biochemicals Inc. (South Bend, IN, USA). Stock solution of the glycan was prepared by dissolving a known mass in ultrafiltered water (Milli-Q Millipore, MA) to achieve a final concentration of ~1 mM, the stock solution was stored at -20 ºC until needed.

3.2.1.2 Protein

Prostate-Specific Antigen (PSA, MW 28,430 Da) was purchased from LEE Biosolutions (Maryland Heights, MO, USA). Human carbonic anhydrase I (hCA, MW 28,848 Da) and Neuraminidase C (NeuC, MW 69000 Da) were purchased from Sigma-Aldrich Canada (Oakville, Canada). Neuraminidase S (NeuS) was purchased from Prozyme (Hayward, ON, CA).

All protein stock solutions were dialyzed against 200 mM aqueous ammonium acetate pH 6.8 four times (4) using an Amicon 0.5 mL microconcentrator with a MW cut-off of 10 kDa (EMD Millipore, Billerica, MA) and stored at -20 ºC until needed. The concentration of protein stock solution was estimated by UV absorption at 280 nm.

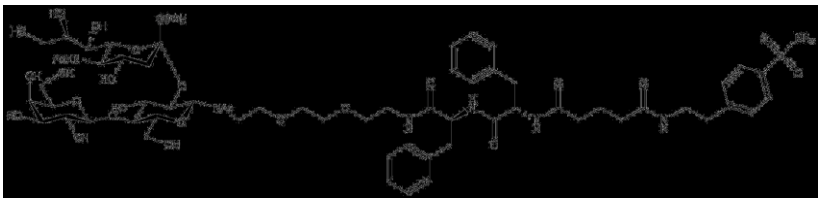

Neu5Acα2-6Galβ1-4Glc-S1(CS_{6SL}^{S1})

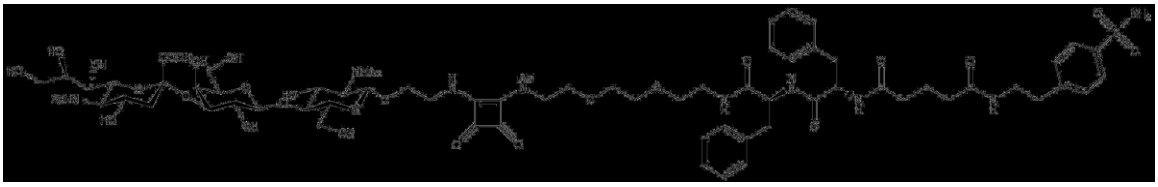

Neu5Acα2-3Galβ1-4GlcNAc-S2 (CS_{3SLNAc}^{S2})

N-acetyl-D-neuraminic acid-1,2,3-$^{13}C_3$ (**IS**)

Figure 3.3. Structures of the glycans used in the present study.

3.2.1.3 (2,3/2,6)-Neu5Ac-linked to PSA

Neuraminidase C (NanC, MW 69000 Da), CMP-Neu5Ac disodium salt (MW 658.41) were purchased from Sigma-Aldrich Canada (Oakville, Canada). Expression of recombinant human sialyltransferases ST6Gal1 (UniProt P15907, amino acid residues 75-406) and ST3Gal4 (UniProt Q11206, amino acid residues 41-333) were performed in Freestyle 293F cells (ThermoFisher Scientific) as GFP fusions in the pGEn2 vector as previously described.[44] Purification by Ni-NTA chromatography, cleavage of the GFP fusion tag with recombinant TEV protease, and further purification by Ni-NTA chromatography and gel filtration was also performed as previously described.[45,46]

3.2.1.4 Removal of N-glycans from PSA

Glycoprotein Denaturing Buffer (10X), Glycobuffer 2 (10X), 10% NP-40 and PNGase F were purchased from New England Biolabs Ltd. (Whitby, ON, Canada). Pierce 1,4-Dithiothreitol (DTT), Hypercab Hypersep Pgc 100 mg/Spherical cartridges, Trifluoroacetic acid (TFA) LC/MS grade and Dimethyl Sulfoxide (DMSO) were purchased from Thermo Scientific (Edmonton, AB, Canada). Sodium Dodecyl Sulfate was purchased from Fisher Scientific (Edmonton, AB, Canada). Anthranilamide (AB) and Sodium cyanoborohydride were purchased from Sigma-Aldrich (Oakville, ON, Canada). Acetonitrile LC/MS grade, Water LC/MS grade and Ammonium formate were purchased from Fisher Chemical (Ottawa, ON, Canada). Oasis HLB 1 cc (30 mg) extraction cartridges were purchased from Waters (Mississauga, ON, Canada). Millipore Milli-Q water system was purchased from Millipore (Millipore Sigma, MA, USA).

3.2.1.5 Extraction of PSA from blood serum

Streptavidin High Performance (HP) SpinTrap was purchased from General Electric Healthcare (Chicago, IL, USA). Biotinylated anti-Prostate Specific Antigen antibody was purchased from abcam (Toronto, ON, Canada). Ammonium acetate and 3-(N,N-Dimethylmyristylammonio)propanesulfonate were purchased from Sigma-Aldrich (Oakville, ON, Canada). Glacial Acetic Acid was purchased from EMD Millipore (Oakville, ON, Canada). Phosphate-buffered saline (PBS) solution was a gift from Ruixiang B. Zheng (University of Alberta). Benchtop centrifuge was purchased from Gyrozen (Gimpo, Republic of Korea). Blood serum was donated by a healthy individual.

3.2.2 Methods

3.2.2.1 Mass spectrometry

All ESI-MS binding measurements were performed in positive ion mode using a Q Exactive Quadrupole-Orbitrap mass spectrometer (Thermo Fisher Scientific, U.K.) equipped with a modified nanoESI source. Standard emitters were produced from borosilicate capillary glass with filament of 1.0 mm outside diameter (o.d.), 0.78 mm inner diameter (i.d.), 10 cm length (Sutter Instruments, CA) using a P-1000 micropipette puller (Sutter Instruments, CA). To perform nanoESI, a platinum wire was inserted into the open end of the emitter, making contact with the solution, and a voltage of ~0.8 kV was applied. The Capillary temperature was 180 ºC, S-lens RF level was 100, maximum inject time was 200

ms and each 10 microscans were combined into a single scan. The typical scan rate was 20 scan/min and approximately 3600 scans were used for specificity testing and collecting data for progress curves. Data acquisition and pre-processing were performed using the Xcalibur software (version 4.1); ion abundances were extracted using in-house software (SWARM).[47] When needed for simplification, raw mass spectra were deconvoluted using Thermo Scientific BioPharma Finder (version 3.0). Glycoforms were assigned using Glyco Mass Calculator (National Institute of Standards and Technology, NIST) and Bruker Compass DataAnalysis (version 5.0).

3.2.2.2 Preparation of (2,3/2,6)-Neu5Ac-linked to PSA

150 µg of seminal plasma PSA (standard PSA) was left mixing with 30 µg of NeuC at 25 ºC in an Eppendorf tube (Eppendorf, ON, Canada) for 6 hours. Then, the tube was placed in a PTC-100 Programmable Thermal Controller (MJ Research, Inc., QC, Canada) at 40 ºC for 24 hours. The tube was cool down at 25 ºC before adding CMP-Neu5Ac for a final concentration of 1 mM with 1 µmol of the required sialyl transferase (ST6Gal1 or ST3Gal4) for 2,6-Neu5Ac-linked to PSA and 2,3-Neu5Ac-linked to PSA, respectively. The reaction was left overnight at 25 ºC. Removal of CMP and purification of 2,3-Neu5Ac-linked to PSA and 2,6-Neu5Ac-linked to PSA was achieved by buffer exchange using 200 mM ammonium acetate and microconcentrator with a MW cut-off of 10 kDa (EMD Millipore, Billerica, MA). The concentrated solutions were stored at -20 ºC until needed.

3.2.2.3 Specificity testing

The specificity for 2,3-Neu5Ac-linked to PSA and 2,6-Neu5Ac-linked to PSA of NeuS was explored using a CUPRA-ZYME system as a control. In this assay oligosaccharides labeled at the reducing end with an affinity tag (e.g. CS_{6SL}^{S1} and CS_{3SLNAc}^{S2}) are recognized by a protein receptor (referred to as universal proxy receptor, ${}^{Uni}P_{proxy}$, in this case hCA). Free ${}^{Uni}P_{proxy}$ and ${}^{Uni}P_{proxy}$ – CS_{6SL}^{S1}/CS_{3SLNAc}^{S2} ions can be detected by ESI-MS, therefore, changes in relative abundances upon introduction of a CAZyme (an enzyme that recognizes carbohydrates as substrates, in this case NeuS) allows for the detection of time-dependent changes in the concentration/fraction of the substrate. In parallel, the conversion of 2,3-Neu5Ac-linked to PSA or 2,6-Neu5Ac-linked to PSA into asialo-PSA was followed over the period of the reaction (240 min). Concentrations of 20 µM ${}^{Uni}P_{proxy}$, 10 µM CS_{6SL}^{S1}, 10 µM CS_{3SLNAc}^{S2} and 5 µM 2,3-Neu5Ac-linked to PSA or 5 µM 2,6-Neu5Ac-linked to PSA were used for these experiments.

The solutions contain 200 mM ammonium acetate at pH 7. The experiments were all performed at 25 ºC.

3.2.2.4 N-glycan analysis

60 µg of standard PSA was denatured with 3 µL of Glycoprotein Denaturing buffer (10X) at 100 ºC for 10 min. The solution was cold down on ice and centrifuged for 10 seconds. A total reaction volume of 100 µL was made by adding 6 µL of Glycobuffer 2 (10X), 6 µL 10% NP-40 and the rest of the volume was made up by adding Milli-Q water. Then, 3 uL PNGase F was added and the reaction mix was incubated at 37 ºC for 16 hours in order to cleave N-glycans from the polypeptide backbone. The solution was filtered using a Hypercarb cartridge to separate the polypeptide backbone from the N-glycans. N-glycans were eluted with 25% ACN in 0.1% TFA and dried under nitrogen gas. AB solution was prepared by dissolving 5 mg of AB in 100 µL of DMSO/acetic acid (7:3 v/v), 6 mg of Sodium cyanoborohydride were added to this solution. Then, 60 µL of AB solution was added to the extracted N-glycans, the solution was left at 65 ºC for 3 h. The solution was cold down at room temperature and filtrated using Oasis HLB extraction cartridge to separate the excess of AB from the N-glycans. The N-glycans were eluted using ACN/Milli-Q water (20:80 v/v) and dried under nitrogen gas. The crystals were reconstituted in 75% ACN/25% Milli-Q water. This solution was separated in two (2) different fractions/vials, 14 µL each. NeuS was added in one vial and 1 µL of Milli-Q water was added in the other vial for a total volume of 15 µL per vial. 2AB derivatized *N*-glycans were separated by ultra-high performance liquid chromatography (UPLC) (ThermoScientific, Germany) with fluorescence detection under the control of ThermoScientific Xcalibur software. Hydrophilic interaction chromatography (HILIC) separations were performed using Waters Acquity UPLC Glycan BEH Amide column, 130 °A, 2.1 x 150 mm, 1.7 µm BEH particles (Milford, MA, USA). Solvent A was 50 mM ammonium formate adjusted to pH 4.4 with formic acid and solvent B was acetonitrile. The column temperature was set to 60 ºC. A linear gradient of 75% to 50% ACN at 0.20 mL/min was used for chromatography. An injection volume of 20 µL sample prepared in 75% v/v acetonitrile was employed. The fluorescence detection excitation/emission wavelengths were 330 nm and 420 nm, respectively. Structural identification was performed by

mass spectrometry using ESI-MS, Q Exactive Quadrupole-Orbitrap mass spectrometer (Thermo Fisher Scientific, U.K.), and a free-software (Glyco Worksbench)[48]. The chromatogram was deconvoluted using Thermo Sciuentific Freestyle.

3.2.2.5 Extraction of PSA from blood serum

400 µL of Milli-Q water was added into the cartridge and centrifuged for 1 min at 150 x g, it was repeated 3 times. This step is performed to clean up the cartridge. 400 µL of PBS was added into the cartridge and centrifuged for 1 min at 150 x g to equilibrate the column, it was repeated 3 times. An aliquot of 100 µL of the antibody was dissolved into 200 µL of PBS, this solution was poured into the cartridge. The medium was suspended by inversion for 20 min. 625 pmol of antibody were approximately deposited into the cartridge. The cartridge was centrifuged for 1 min at 150 x g to remove unbound biotinylated antibody. The cartridge was washed with 400 µL of PBS three times. 200 µL of PBS and 400 µL of human serum were mix manually for 2 min and by inversion for 58 min. The cartridge was centrifuged for 1 min at 150 x g to wash out unbound PSA. 400 µL of 0.01% Zittergent in PBS was added into the cartridge and centrifuged for 1 min at 150 x g. This step was repeated five times. Then, Milli-Q water was added into the cartridge and centrifuged for 1 min at 150 x g. This step was repeated three times. 150 µL of acetic acid/200 mM AmAc buffer pH 5.5 was added into the cartridge and mixed manually for 2 min by inversion and incubated at 4 ºC for 28 min. The cartridge was further centrifuged for 1 min at 1000 x g, this step was repeated three times, however, it is not necessary to incubate it the second and third time. The eluates were collected in one tube. This solution was transferred to a 50 kDa filter and centrifuged for 40 min at 14000 x g. The concentrated solution was transferred to a 10 kDa filter and the concentrate was buffer exchanged four times using 200 mM AmAc buffer pH 7 for 20 min at 14000 x g and 5 ºC. The last centrifugation was performed for 40 min at 14000 x g and 5 ºC.

3.3 Data analysis

3.3.1 Progress curves for specificity testing

At a given reaction time, the fractional abundance of PSA_{asialo} ($F_{PSA\text{-}asialo}$) and CUPRA products

were calculated using Eq. 3.1 and Eq. 3.2.

$$F_{PSA_{asialo}} = \frac{2Ab(PSA_{asialo}) + Ab(PSA_{monosialo})}{2[Ab(PSA_{asialo}) + Ab(PSA_{monosialo}) + Ab(PSA)]} \quad \text{Eq, 3.1}$$

where $PSA_{monosialo}$ represents monosialylated-PSA, while PSA_{asialo} represents PSA glycoforms without Neu5Ac.

$$F_{CP} = \frac{Ab({}^{Uni}P_{proxy} - CP)}{Ab({}^{Uni}P_{proxy}) + Ab({}^{Uni}P_{proxy} - CS) + Ab({}^{Uni}P_{proxy} - CP)} \quad \text{Eq, 3.2}$$

where Ab(CP), Ab(CS) and $Ab({}^{Uni}P_{proxy})$ are the gas-phase abundances of CP, CS and ${}^{Uni}P_{proxy}$, respectively.

3.3.2 Relative abundances of N-glycans from PSA by HILIC-fluorescence

The relative abundance of each N-glycan was calculated using the sum of the intensities of the detected N-glycans and individual intensities by for each N-glycan as shown in Eq. 3.3.

$$\text{Abundance}_{N-glycan} = \frac{\text{Intensity}_{N-glycan}}{\Sigma\ \text{Intensities}_{N-glycans}} \text{x}100\% \quad \text{Eq, 3.3}$$

3.3.3 Quantification of α2,3-Neu5Ac on standard PSA using IS

A solution of 2 µM PSA, 2.5µM **IS**, treated with NeuS into 200 mM AmAc pH 7 at 25 ºC was sprayed three (3) times using standard emitters. Each replicate represents one (1) set of progress curve (1 progress curve for Neu5Ac and 1 progress curve for PSA_{asialo}). Data were collected and processed as described in section 3.2.2.1 (Mass Spectrometry). The fractional abundance of PSA_{asialo} ($F_{PSA\text{-}asialo}$) was calculated taking into consideration all the sialylated species detected in the spectrum, see Eq. 3.1. The species found in the spectrum are listed in Table 3.4. The fractional abundance of Neu5Ac was calculated using Eq. 3.4.

$$[\text{Neu5Ac}] = \frac{[\text{Neu5Ac-}^{13}\text{C}_3](Ab(\text{Neu5Ac}) + (Ab(\text{Neu5Ac})^{Na} + Ab(\text{Neu5Ac})^{P})}{Ab(\text{Neu5Ac-}^{13}\text{C}_3) + Ab(\text{Neu5Ac-}^{13}\text{C}_3^{Na}) + Ab(\text{Neu5Ac-}^{13}\text{C}_3^{P})} \quad \text{Eq, 3.4}$$

where Ab(Neu5Ac), Ab(Neu5Ac^{Na}) and Ab(Neu5Ac^{P}) are the gas-phase abundances of protonated, sodiated and potassiated Neu5Ac ions, respectively, and Ab(Neu5Ac-$^{13}C_3$), Ab(Neu5Ac-$^{13}C_3^{Na}$) and Ab(Neu5Ac-$^{13}C_3^{P}$) are the gas-phase abundances of protonated, sodiated and potassiated Neu5Ac-$^{13}C_3$ ions.

3.4 Results and Discussion

3.4.1 Specificity of NeuS for α2,3-linked Neu5Ac

NeuS, a *Streptococcus pneumoniae* neuraminidase, has been extensively used in the literature for the specific cleavage of α2,3-Neu5Ac-linked to PSA.[7,11,32] The specificity of NeuS (also called Nan1, NanB) for α2,3-Neu5Ac was demonstrated by incubation with human α-1 acid glycoprotein (AGP), this glycoprotein has both α2,6- and α2,3-linked Neu5Ac.[49] Lectin blotting with *Sambucus nigra* agglutinin (SNA, specificity for α2,6-linked Neu5Ac), MAA (specificity for α2,3-linked Neu5Ac) and *Datura stramonium* agglutinin (DSA, specificity for galactose β1,4-linked to N-acetylglucosamine (Galβ1,4-GlcNAc) within the N-linked glycan in both the presence and absence of terminal Neu5Ac) was used to detect α2,6-linked Neu5Ac, α2,3-linked Neu5Ac and Galβ1,4-GlcNAc, respectively. AGP treated with NeuS could be detected using SNA and DSA but not MAA.[49] In the same work, 3'Sialyllactose (3SL) and 6'Sialyllactose (6SL) were used as substrates for NeuS and the Amplex Red Neuraminidase assay was employed for fluorescence detection. Briefly, the cleavage of Neu5Ac generates terminal-linked galactose as enzymatic product, the Amplex Red Neuraminidase assay adds galactose oxidase to oxidize the hydroxyl at position 6 of the terminal galactose, which in presence of Amplex Red and Horseradish peroxidase (HRP) produces resorufin (a fluorogenic compound). The authors concluded that NeuS does not have enzymatic activity towards α2,6-linked Neu5Ac.[49] Additionally, the authors found out that NeuS produces exclusively 2,7-anhydro-Neu5Ac instead of Neu5Ac, and that free Neu5Ac can be a substrate for NeuS as well.[49] These findings are in agreement with a previous report in which a sialidase produced by *Macrobdella decora* (leech)

was found to be α2,3-Neu5Ac-specific.[50] Steric hindrance in the active site of NeuS due to stacking residues (Tyr589 and Trp674) accounts for the strict specificity of NeuS towards α2,3-linked Neu5Ac (PDB 2JKB).[49] In the active site the C2-OH acquires a proton and leaves, the intermediate with a positive charge in C2 (oxycarbenium intermediate) adopts a boat conformation, this constraint brings the C7-OH into close proximity to the C2-atom and enables the formation of the 2,7-anhydro bond (Figure 3.4).[49,50] Generally, the space above the carboxylate of Neu5Ac is left open in the active site of most bacterial and viral sialidase to non-selectively accommodate the subterminal glycan.[50]

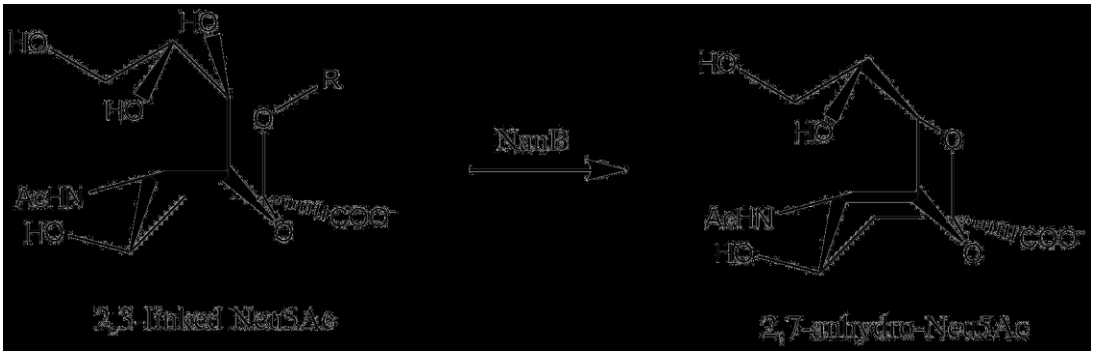

Figure 3.4. Enzymatic product of NeuS, R represents a glycoconjugate. The chair conformation is adopted in the active site of the enzyme.

Despite the experiments shown in Ref. 49 aimed at demonstrating the specificity for α2,3-linked Neu5Ac of NeuS, the authors did not report quantitative comparison of the specificity of NeuS towards α2,3-linked Neu5Ac. Here, we used time-resolved MS data to accurately measure the fractional abundance of PSA_{asialo} from 2,3-Neu5Ac-linked to PSA and 2,6-Neu5Ac-linked to PSA over the period of the enzymatic reaction (Figure 3.5 and Figure 3.6). In this experiment we used CS_{6SL}[S1] and CS_{3SLNAc}[S2] as controls of the enzymatic activity. This approach offers several advantages over quenching approaches; the substrates of interest are authentic substrates. Also, MS allows to unambiguously identifying species in solution, in this case substrates and enzymatic products. Additionally, the approach does not require quenching and this allows a quantitative assessment of the specificity using accurate measurements of initial rates.

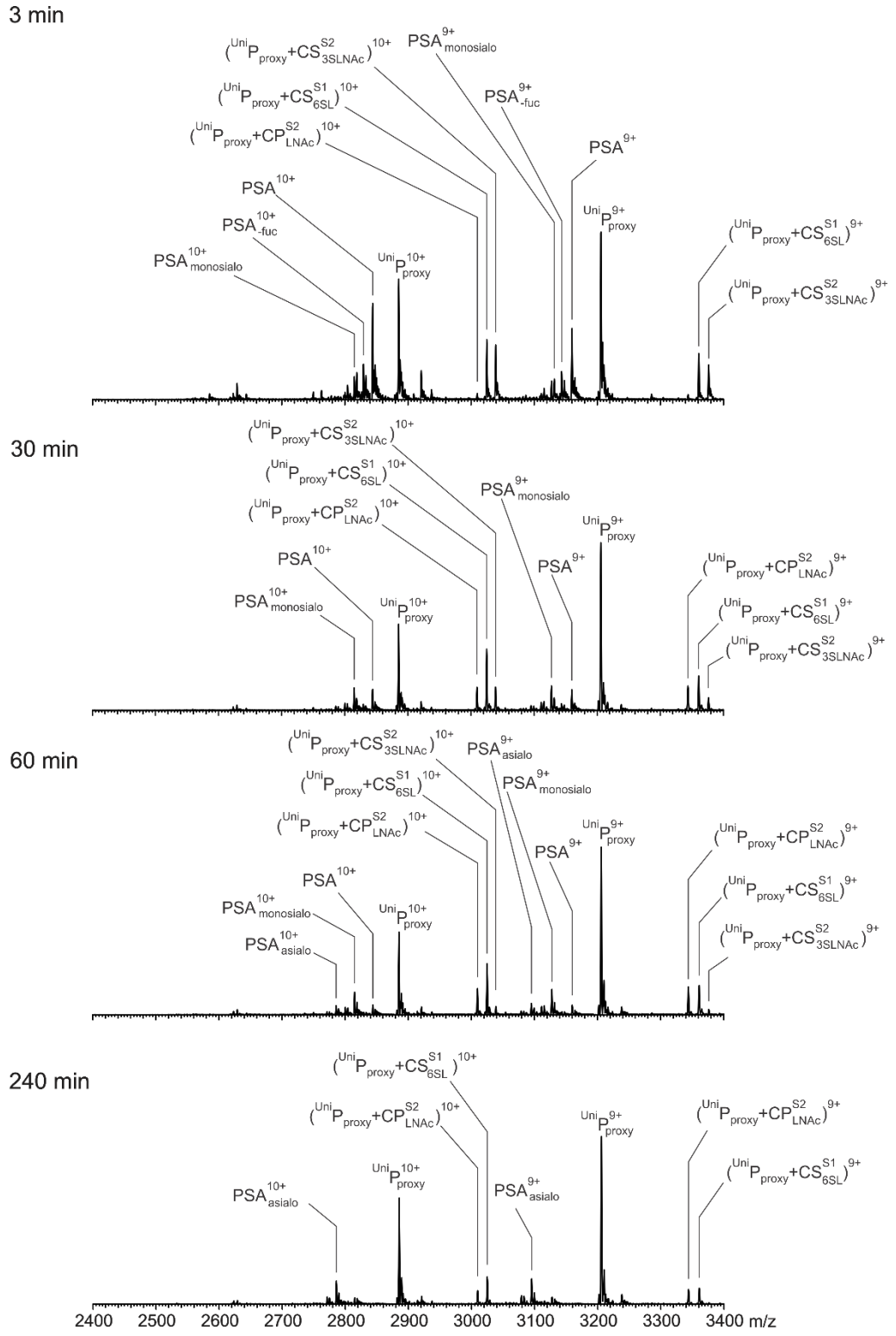

Figure 3.5. Representative ESI mass spectra of a solution of 20 μM $UniP_{proxy}$, 10 μM CS_{6SL}^{S1}, 10 μM CS_{3SLNAc}^{S2} and 5 μM 2,3-Neu5Ac-linked to PSA in presence of NeuS and 200 mM

ammonium acetate at pH 7 and 25 ºC. The spectra were taken at different time points: a) 0-3 min; b) 29-30 min; c) 59-60 min; 239-240 min.

ESI mass spectra in Figure 3.5 were collected continuously (time-resolved) starting 3 min after mixing. $^{Uni}P_{proxy}$ complexes with the CUPRA substrates can be followed in the m/z window from 2800 to 3400. The progressive consumptions of CS_{3SLNAc}^{S2} and 2,3-Neu5Ac-linked to PSA are observed over time. In contrast, ion signals of CS_{6SL}^{S1} remains steady over the reaction period. This suggests the reactivity of the enzyme towards α2,3-Neu5Ac-containing substrates. In order to assess if the enzyme digests α2,6-Neu5Ac-linked to glycoproteins, another experiment was performed adding 2,6-Neu5Ac-linked to PSA instead of its 2,3-Neu5Ac counterpart (Figure 3.6). It is observed the ion signals of CS_{6SL}^{S1} and 2,6-Neu5Ac-linked to PSA remains steady over the reaction period while CS_{3SLNAc}^{S2} is totally consumed after 60 min of reaction. The no reactivity of the enzyme towards α2,6-Neu5Ac-containing substrates is in agreement with previous reports.[7,11,32,49] To quantitatively establish the specificity of the enzyme, progress curves were constructed. These curves are plots of fractional abundances of the enzymatic products of 2,3-Neu5Ac-linked to PSA or 2,6-Neu5Ac-linked to PSA (PSA_{asialo}) versus time (Figure 3.7). The fractional abundances were obtained using Eq. 3.1 and Eq. 3.2 for 2,3-Neu5Ac-linked to PSA/2,6-Neu5Ac-linked to PSA and CUPRA product (CP), respectively . Using the progression curves for 2,3-Neu5Ac-linked to PSA and 2,6-Neu5Ac-linked to PSA, the initial rates were determined with data acquired from 3 to 7 min, where the curve is still linear as observed in Table 3.2. The reactivity of NeuS towards 2,3-Neu5Ac-linked to PSA is ~300 times higher than 2,6-Neu5Ac-linked to PSA. Therefore, the enzyme selectively recognizes α2,3-Neu5Ac. On the other hand, the substrates employed for these experiments are natural substrates in the biological context of PSA, however, the biological sample is more complex regarding the number of glycoforms. This will be addressed in the next section.

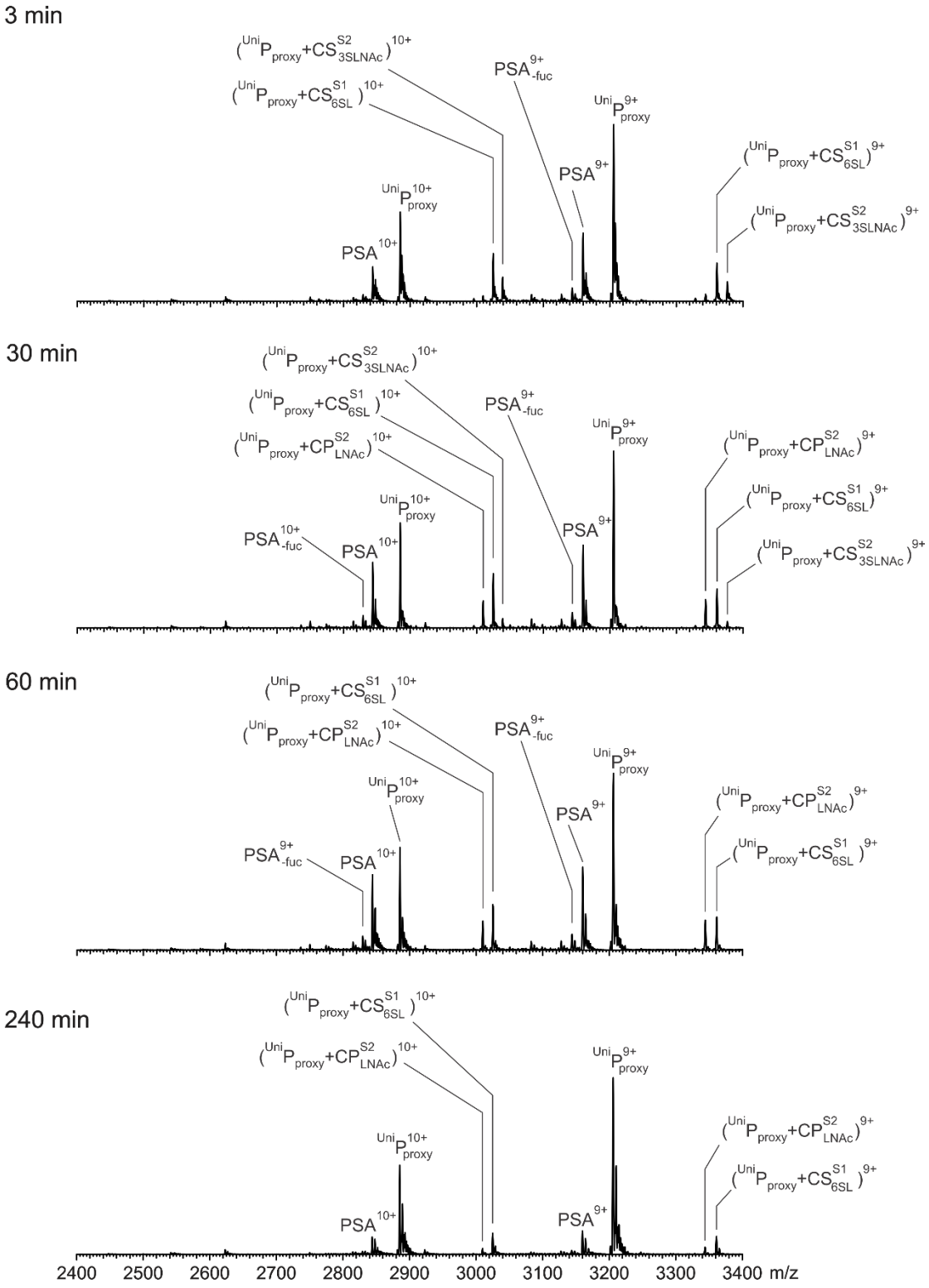

Figure 3.6. Representative ESI mass spectra of a solution of 20 μM $UniP_{proxy}$, 10 μM CS_{6SL}^{S1}, 10 μM CS_{3SLNAc}^{S2} and 5 μM 2,6-Neu5Ac-linked PSA in presence of NeuS and 200 mM ammonium

acetate at pH 7 and 25 ºC. The spectra were taken at different time points: a) 0-3 min; b) 29-30 min; c) 59-60 min; 239-240 min.

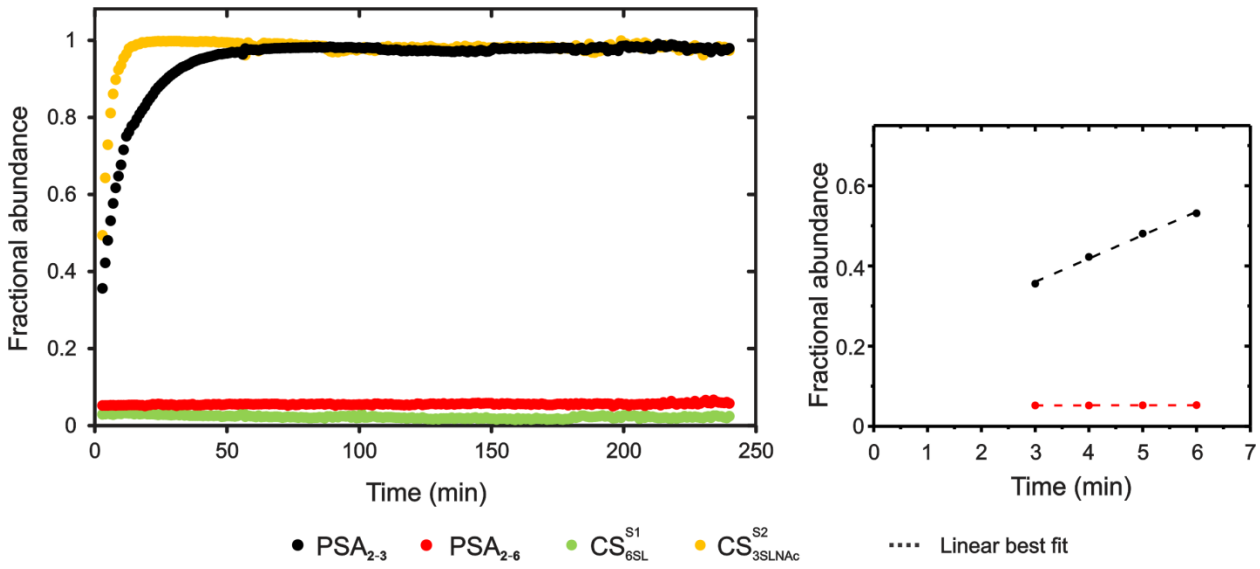

Figure 3.7. Fractional abundance of PSA_{asialo} from 2,3-Neu5Ac-linked to PSA (black curve) or 2,6-Neu5Ac-linked to PSA (red curve) after treatment with NeuS. Also, the fractional abundances of lactose (green curve) from 6SL and N-acetyllactosamine (orange curve) from 3SLNAc were included. Raw data was taken from Figure 3.5 and Figure 3.6.

3.4.2 Glycoforms of PSA (N-glycan analysis)

N-glycans from PSA have been evaluated since early 2000s and there are several reports available in the literature.[7,11,31-34,37,39,40,51] Mainly, PSA bears complex N-glycans but hybrid and high-mannose have also been reported in seminal plasma.[39] The N-glycan with the highest abundance has been reported to be core fucosylated biantennary disialylated complex N-glycan, with a relative abundance between 45-50%.[7,11,40] This is consistent with our findings, where the core fucosylated biantennary disialylated complex N-glycan was the most abundant N-glycan with a relative abundance of ~ 41% (Figure 3.8 and Table 3.3). The relative abundance of N-glycans from PSA was calculated using Eq. 3.3.

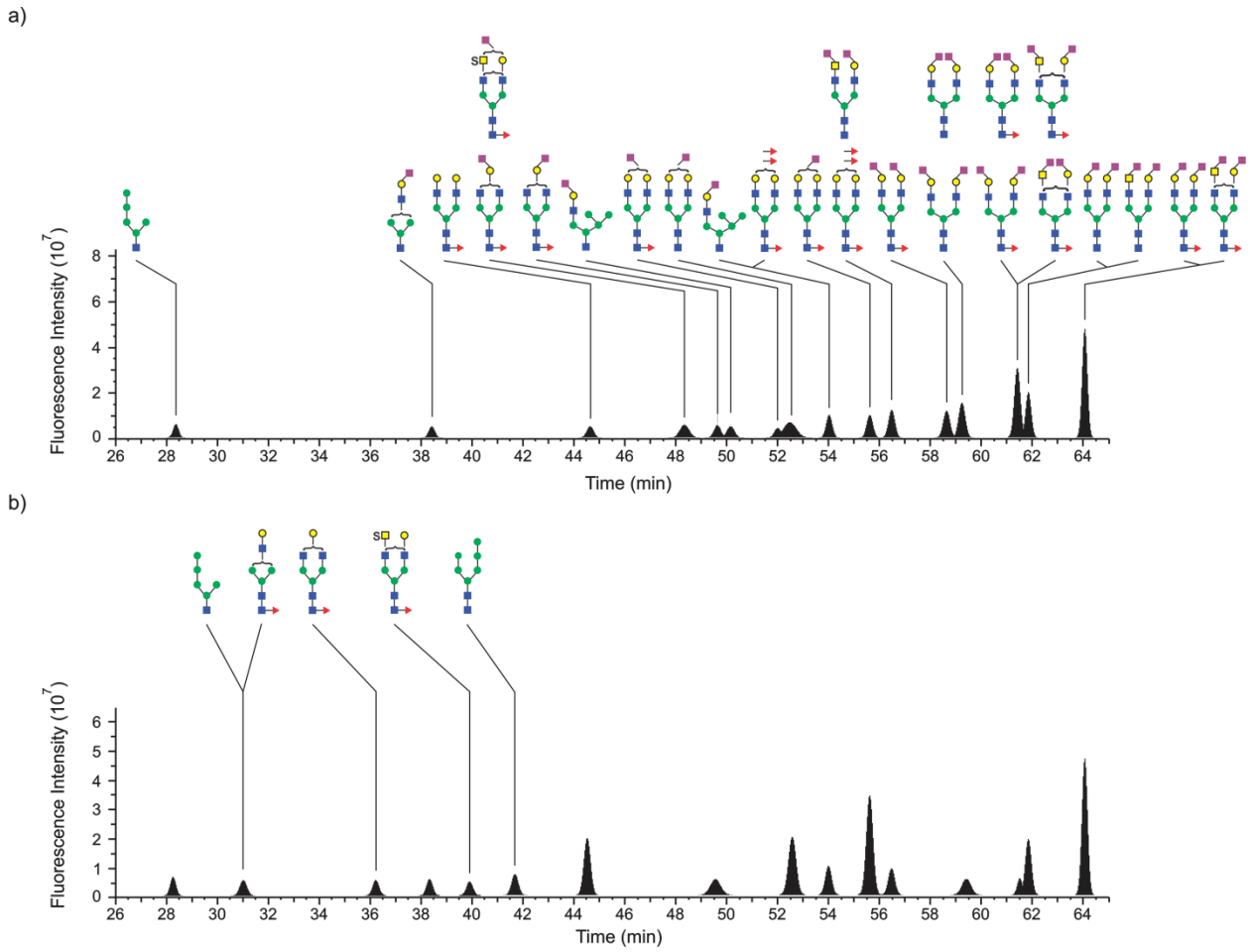

Figure 3.8. Deconvoluted chromatogram of N-glycans from PSA a) before treatment with NeuS and; b) after treatment with NeuS.

The second most abundant N-glycan is non-core fucosylated biantennary disialylated with an abundance of ~ 23%, while the third and fourth most abundant are core fucosylated biantennary monosialylated and non-core fucosylated biantennary monosialylated with relative abundances of ~ 7%. Notably, these are the glycoforms detected by ESI-MS as well, as shown in Figure 3.9. These glycoforms cover approximately 71% of the N-glycans detected by HILIC-Fluorescence. However, the relative abundance of the N-glycans bearing α2,3-Neu5Ac but not detected by ESI-MS is 7% as per the data shown in Figure 3.9. Aiming for an increase in the detection of N-glycans, our Q Exactive UHMR Quadrupole-Orbitrap mass spectrometer (Thermo Fisher Scientific, U.K.) was also employed. In this case, voltages of lenses, accumulation time of the ions, gas pressure, narrower band pass were parameters tuned manually

to increase the sensitivity. Unfortunately, the adjustments of those parameters might be useful for a qualitative improvement of the spectrum but, in exchange, a narrower window of m/z can only be detected. Also, the parameters need to be tuned according to the m/z window that needs to be detected. In practice, this strategy cannot be pursued for quantitative analysis. Although 7% of the N-glycans bearing α2,3-Neu5Ac could not be detected by ESI-MS, the parameters shown in section 3.2.2.1 gave us the best sensitivity for the quantification of the ratio of α2,3-Neu5Ac to α2,6-Neu5Ac.

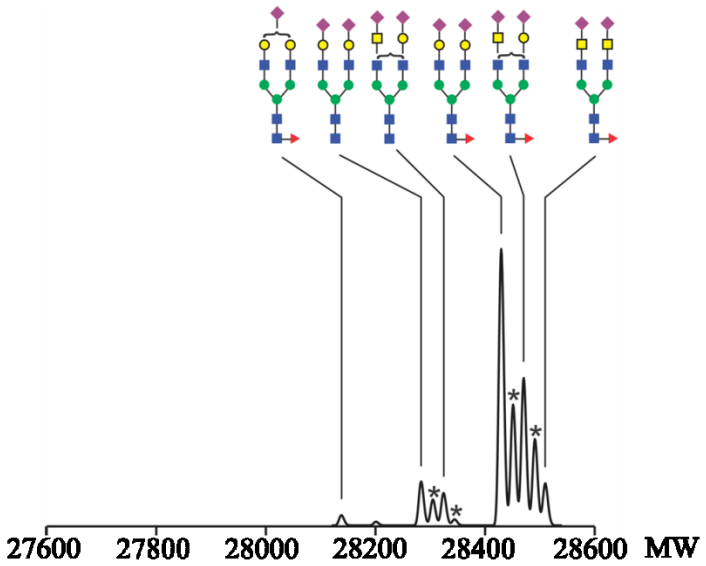

Figure 3.9. Deconvoluted spectrum of a solution of 5 µM PSA in 200 mM ammonium acetate at pH 7 and 25 ºC. The peaks marked with an asterisk represent the sodium adducts of the ion peak of the glycoform shown at the left of the asterisk. The raw data was deconvoluted using Thermo Scientific Biopharma Finder.

3.4.3 Quantification of the ratio of α2,3-Neu5Ac to α2,6-Neu5Ac on standard PSA

To assess the accuracy of the quantification of α2,3-Neu5Ac on PSA by ESI-MS a solution of 2 µM PSA, 2.5 µM Neu5Ac-$^{13}C_3$ (**IS**) in presence of NeuS into 200 mM ammonium acetate at pH 7 and 25 ˚C was sprayed in triplicate. Representative ESI mass spectra are shown in Figure 3.10. The theoretical molecular weights of the glycoforms are listed in Table 3.4. Using Eq. 3.1 and Eq. 3.4 for calculation of the fractional abundance of PSA_{asialo} and Neu5Ac, respectively, a plot of the fractional abundances over the period of the enzymatic reaction were

obtained for both species (Figure 3.11).

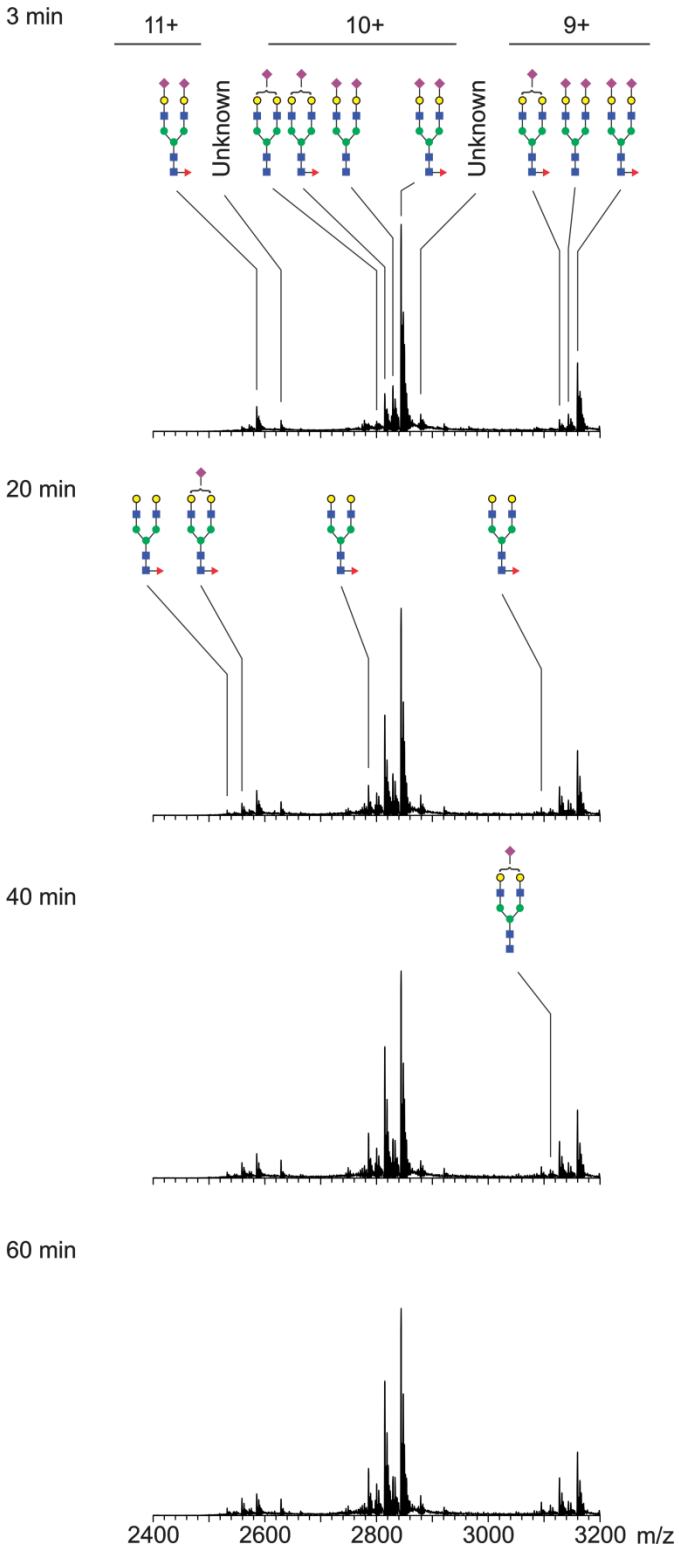

Figure 3.10. Representative ESI mass spectra of a solution of 2 μM PSA and 2.5 μM Neu5Ac-

$^{13}C_3$ (**IS**) in presence NeuS into 200 mM ammonium acetate at pH 7 and 25 ºC.

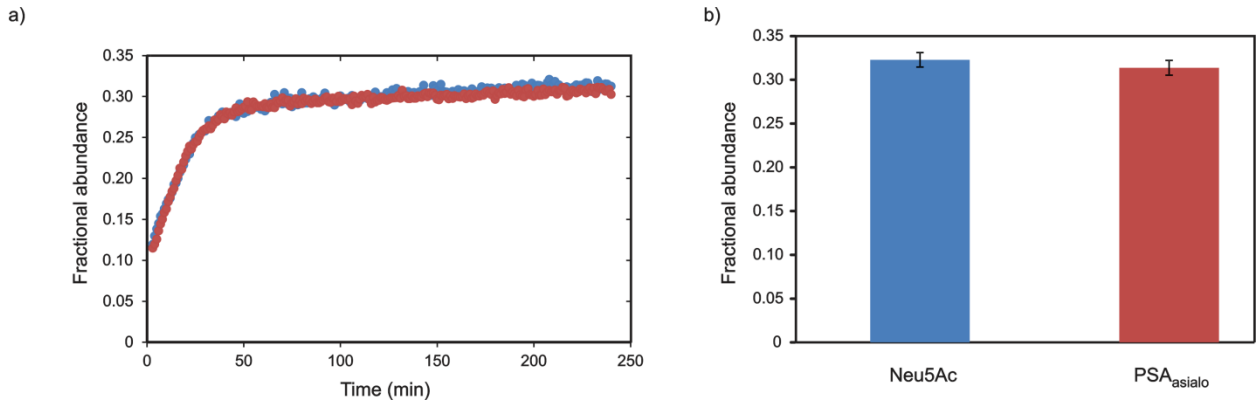

Figure 3.11. a) Progress curves of PSA_{asialo} (red dots) and Neu5Ac (blue dots). b) Fractional abundance of Neu5Ac from N-glycans on PSA and PSA_{asialo}, respectively, from a solution of 2 µM PSA, 2.5 µM Neu5Ac-$^{13}C_3$ (**IS**) in presence of NeuS into 200 mM ammonium acetate at pH 7 and 25 ºC. The experiment was formed using n=3 replicates.

The consumption of the substrate was completed after 60 min of the enzymatic reaction, as it can be observed from the plateau in Figure 3.11a. One set of progression curves was shown for illustration, however, the experiment was performed using n=3 replicates. It is important to mention that two enzymatic products are formed from the enzymatic reaction, PSA_{asialo} is the main product as observed from the ion signal in the spectra shown in Figure 3.10 but $PSA_{monosialo}$ is also formed. $PSA_{monosialo}$ contributes to the fractional abundance of α2,3-Neu5Ac on PSA as shown in Eq. 3.1. This is expected from the results obtained by N-glycan analysis (Table 3.3) where core fucosylated biantennary disialylated (α2,3-/α2,6-) species account for ~15% of the relative abundance while non-core fucosylated biantennary disialylated (α2,3-/α2,6-) species account for ~8%. Regarding the quantification of the F_{Neu5Ac}, the ratio between the ion intensities of the **IS** and the enzymatic product was employed for its calculation. Notably, the enzymatic product of this reaction was 2,7-anhydro-Neu5Ac (MW 292 Da), which is produced as a consequence of a intramolecular nucleophilic attack with loss of water. This enzymatic product has a difference of 18 Da in comparison with Neu5Ac (MW 310 Da). Unfortunately, there is no commercially available C-13 labeled standard for 2,7-anhydro-Neu5Ac. Therefore, the response factors of the available **IS** and 2,7-anhydro-Neu5Ac were considered similar assuming the

difference in molecular weight does not influence the ionization efficiency of the species in the gas-phase. The fractional abundance of α2,3-Neu5Ac on standard PSA was calculated to be 0.31 ± 0.01 (Figure 11b). Notably, this result is in agreement with the relative abundance of α2,3-Neu5Ac on standard PSA calculated by N-glycan analysis, where its relative abundance was found to be ~ 34% (Table 3.3). Only the species annotated as α2,3-Neu5Ac-containing N-glycans in the chromatogram (Figure 3.8) were considered for the relative abundance of α2,3-Neu5Ac on standard PSA.

3.4.4 Extraction of PSA from blood serum

The procedure described above for the extraction of PSA from blood serum was carried to qualitatively assess the purity of the solution after extraction. It is important to mention that the purification step using a 50 kDa filter was not included in the initial protocol. Human Serum Albumin (from now on Albumin) was detected as the most abundant ion peak (Figure 3.12a). Albumin is the most abundant protein in human serum, it is normally present at concentrations between 30-50 g/L and accounts for 60% of the total protein content in serum.[52] It has a MW of 6.7 kDa, which matches the MW of the protein detected in the spectrum. Although Albumin is not glycosylated, it might suppress the ionization of PSA due to its much higher concentration in blood serum. Therefore, a double purification step was included (a 50 kDa filter) as part of the procedure in an attempt to remove Albumin from the solution after extraction. To evaluate how effective the double purification step was, the aliquot of blood serum was spiked to have an aliquot of blood serum with 10 μM standard PSA. Then, the extraction procedure was carried out and the spectra compared (Figure 3.12b). The quality of the spectrum after including a second purification step increased dramatically. Unfortunately, a limit of quantification was not performed to assess the amount of PSA that can be extracted and quantified using ESI-MS. This step is rather important if the purpose of the method is to quantify the ratio of α2,3-Neu5Ac to α2,6-Neu5Ac in real samples, where the concentration of free PSA can be as low as (0.97 ± 0.01) μg/L in PCa patients.[53] An experiment that addresses this question requires female blood serum with no detectable levels of PSA.

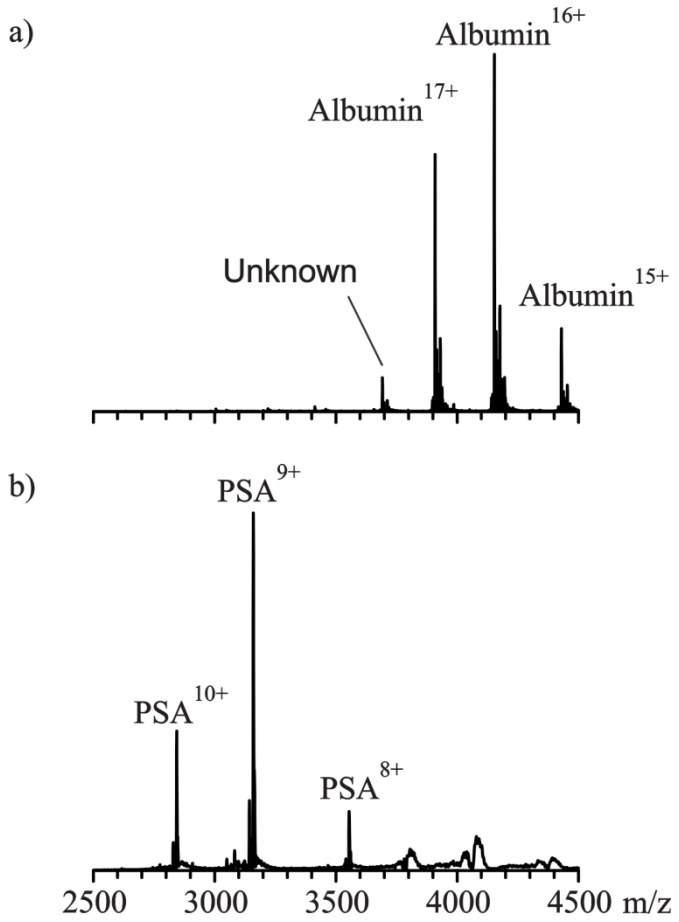

Figure 3.12. Representative mass spectra for a solution of a) an aliquot of blood serum from a healthy individual; b) an aliquot of blood serum spiked with PSA to have a final concentration of 10 µM PSA, into 200 mM ammonium acetate at pH 7 and 25 ºC.

Table 3.1. tPSA levels related to medical conditions regarding Prostate Cancer (PCa). This information was extracted from Ref. 10

Condition	Normal	Uncertain	Abnormal
tPSA level ($ngmL^{-1}$)	≤ 4	4-10	≥ 10
Percentage of Patients diagnosed with PCa (%)	15	30-35	67

Table 3.2. Specificity for α2,3-Neu5Ac-linked PSA of NanB

Enzyme	Substrate	Initial rates (fraction/min)	Coefficient of determination (R^2)
NanB	2,3-Neu5Ac-linked PSA	0.0584 ± 0.0003	0.995
	2,6-Neu5Ac-linked PSA	0.00020 ± 0.00003	0.955

Table 3.3. Relative abundance of N-glycan by HILIC-Fluorescence

Before treatment			After treatment			
t_R (min)	Peak Area	% Area	t_R (min)	Peak Area	% Area	Difference (%)
28.38	92343261.1	2.64	28.27	105840569	2.62	
31.03	0	0	31.03	107267186	2.65	
36.23	0	0	36.23	95998262.4	2.38	
38.42	85556367.5	2.45	38.34	99878821.5	2.47	
39.91	0	0	39.91	87345216.4	2.16	
40.88	0	0	40.88	79449887.7	1.97	
41.69	0	0	41.69	141643155	3.50	
44.64	95134670.6	2.72	44.53	370462552	9.16	
48.35	146940192	4.20	48.35	0	0	4.20
49.64	106263810	3.04	49.56	156540730	3.87	
50.16	105920612	3.03	50.16	0	0	3.03
52.48	243099777	6.95	52.57	435922881	10.78	
54.03	168854931	4.83	54.00	182124899	4.51	
55.31	0	0	55.31	49796643.4	1.23	
55.62	175038663	5.00	55.61	651375043	16.11	
56.48	220373097	6.30	56.47	169524892	4.19	2.10
58.64	226656886	6.48	58.64	0	0	6.48
59.24	288308965	8.24	59.41	141966859	3.51	4.73
61.41	525334032	15.01	61.51	84305814.8	2.09	12.93
61.85	315533475	9.02	61.84	336952110	8.33	
64.06	704497373	20.13	64.06	746468293	18.46	

Table 3.4. Glycoforms from N-glycans on PSA found by N-glycan analysis. Compositions are given as H_N_S_F_Su: H (Hex, 162.1406 Da), N (HexNAc, 203.1925 Da), S (Sia, 291.2546 Da), F (Fuc, 146.1412 Da) and Su (Sulfur, 32.065 Da).

Glycoform structure	Annotation	MW
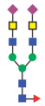	H3N6S2F	28512.05
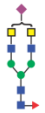	H3N6SF	28220.95
	H3N6F	27929.79
	H4N5S2F	28470.96
	H4N5SF	28179.85
	H4N5F	27888.77
	H5N4S2F	28429.93
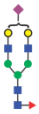	H5N4SF	28138.90
	H5N4F	27847.80
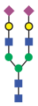	H5N4S2	28283.94
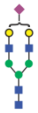	H5N4S	27992.84
	H5N4	27701.74

3.5 Conclusions

This work demonstrates the capability of ESI-MS for the relative quantification of Neu5Ac from Neu5Ac-linked to glycoproteins such as PSA. The method does not require either a time-consuming sample preparation or labeling. However, the lack of commercially available ^{13}C-labeled 2,7-anhydro-Neu5Ac hampered the application of this approach for the quantification of the ratio of α2,3-Neu5Ac to α2,6-Neu5Ac-linked to N-glycans from PSA. The extraction of spiked PSA from blood serum of a healthy donor was achieved successfully, as demonstrated by the quality of the spectrum after extraction.

3.6 References

(1) Siegel, R. L.; Miller, K. D.; Jemal, A. Cancer Statistics, 2020. *CA. Cancer J. Clin.* **2020**, *70*, 7–30.

(2) O'Reilly, J.-A. Prostate Cancer Detection: Complexities and Strategies. *J. Cancer Treat. Diagnosis* **2017**, *2*, 18–25.

(3) Guo, S.; Briza, P.; Magdolen, V.; Brandstetter, H.; Goettig, P. Activation and Activity of Glycosylated KLKs 3, 4 and 11. *Biol. Chem.* **2018**, *399*, 1009–1022.

(4) Balk, S. P.; Ko, Y. J.; Bubley, G. J. Biology of Prostate-Specific Antigen. *J. Clin. Oncol.* **2003**, *21*, 383–391.

(5) Sotiropoulou, G.; Pampalakis, G.; Diamandis, E. P. Functional Roles of Human Kallikrein-Related Peptidases. *J. Biol. Chem.* **2009**, *284*, 32989–32994.

(6) Mikolajczyk, S. D.; Marks, L. S.; Partin, A. W.; Rittenhouse, H. G. Free Prostate-Specific Antigen in Serum Is Becoming More Complex. *Urology* **2002**, *59*, 797–802.

(7) Gratacós-Mulleras, A.; Duran, A.; Asadi Shehni, A.; Ferrer-Batallé, M.; Ramírez, M.; Comet, J.; de Llorens, R.; Saldova, R.; Llop, E.; Peracaula, R. Characterisation of the Main PSA Glycoforms in Aggressive Prostate Cancer. *Sci. Rep.* **2020**, *10*, 1–14.

(8) Punnen, S.; Pavan, N.; Parekh, D. J. Finding the Wolf in Sheep's Clothing: The 4Kscore Is a Novel Blood Test That Can Accurately Identify the Risk of Aggressive Prostate Cancer. *Rev. Urol.* **2015**, *17*, 3–13.

(9) Butch, A. W.; Crary, D.; Yee, M. Analytical Performance of the Roche Total and Free PSA Assays on the Elecsys 2010 Immunoanalyzer. *Clin. Biochem.* **2002**, *35*, 143–145.

(10) Rodriguez, J. Z.; O'Kennedy, R. New Approaches for the Development of Diagnostic Systems for Prostate Cancer. *Asian Hosp. Heal. Manag.* **2017**, *36*, 18–23.

(11) Tabarés, G.; Radcliffe, C. M.; Barrabés, S.; Ramírez, M.; Aleixandre, N.; Hoesel, W.; Dwek, R. A.; Rudd, P. M.; Peracaula, R.; de Llorens, R. Different Glycan Structures in Prostate-Specific Antigen from Prostate Cancer Sera in Relation to Seminal Plasma PSA. *Glycobiology* **2006**, *16*, 132–145.

(12) Tkac, J.; Gajdosova, V.; Hroncekova, S.; Bertok, T.; Hires, M.; Jane, E.; Lorencova, L.; Kasak, P. Prostate-Specific Antigen Glycoprofiling as Diagnostic and Prognostic Biomarker of Prostate Cancer. *Interface Focus* **2019**, *9*.

(13) Lilja, H.; Ulmert, D.; Vickers, A. J. Prostate-Specific Antigen and Prostate Cancer:

Prediction, Detection and Monitoring. *Nat. Rev. Cancer* **2008**, *8*, 268–278.

(14) Crawford, E. D.; Denes, B. S.; Ventii, K. H.; Shore, N. D. Prostate Cancer: Incorporating Genomic Biomarkers in Prostate Cancer Decisions. *Clin. Pract.* **2014**, *11*, 605–612.

(15) Hatakeyama, S.; Yoneyama, T.; Tobisawa, Y.; Ohyama, C. Recent Progress and Perspectives on Prostate Cancer Biomarkers. *Int. J. Clin. Oncol.* **2017**, *22*, 214–221.

(16) De Angelis, G.; Rittenhouse, H. G.; Mikolajczyk, S. D.; Blair Shamel, L.; Semjonow, A. Twenty Years of PSA: From Prostate Antigen to Tumor Marker. *Rev. Urol.* **2007**, *9*, 113–123.

(17) Catalona, W. J.; Partin, A. W.; Slawin, K. M.; Brawer, M. K.; Flanigan, R. C.; Patel, A.; Richie, J. P.; DeKernion, J. B.; Walsh, P. C.; Scardino, P. T.; Lange, P.H.; Subong, E.N.; Parson, R.E.; Gasior. G.H.; Loveland, K.G.; Southwick, P.C. Use of the Percentage of Free Prostate-Specific Antigen to Enhance Differentiation of Prostate Cancer from Benign Prostatic Disease: A Prospective Multicenter Clinical Trial. *J. Am. Med. Assoc.* **1998**, *279*, 1542–1547.

(18) Ceylan, C.; Gazel, E.; Kele, B.; Doluolu, Ö.; Yman, M. Can the Free/Total PSA Ratio Predict the Gleason Score before Prostate Biopsy? *Curr. Urol.* **2015**, *9*, 24–27.

(19) Benson, M. C.; Ihn Seong Whang; Pantuck, A.; Ring, K.; Kaplan, S. A.; Olsson, C. A.; Cooner, W. H. Prostate Specific Antigen Density: A Means of Distinguishing Benign Prostatic Hypertrophy and Prostate Cancer. *J. Urol.* **1992**, *147*, 815–816.

(20) Sharma, P.; Zargar-Shoshtari, K.; Pow-Sang, J. M. Biomarkers for Prostate Cancer: Present Challenges and Future Opportunities. *Future Sci. OA* **2016**, *2*, FSO72.

(21) Ferro, M.; Bruzzese, D.; Perdonà, S.; Marino, A.; Mazzarella, C.; Perruolo, G.; D'Esposito, V.; Cosimato, V.; Buonerba, C.; Di Lorenzo, G.; Musi, G.; De Cobelli, O.; Chun, F.K.; Terracciano, D. Prostate Health Index (Phi) and Prostate Cancer Antigen 3 (PCA3) Significantly Improve Prostate Cancer Detection at Initial Biopsy in a Total PSA Range of 2-10 ng/ml. *PLoS One* **2013**, *8*, 1–7.

(22) Fossati, N.; Buffi, N. M.; Haese, A.; Stephan, C.; Larcher, A.; McNicholas, T.; De La Taille, A.; Freschi, M.; Lughezzani, G.; Abrate, A.; Bini, V.; Redorta, J.P.; Graefen, M.; Guazzoni, G.; Lazzeri, M. Preoperative Prostate-Specific Antigen Isoform P2PSA and Its Derivatives, %p2PSA and Prostate Health Index, Predict Pathologic Outcomes in Patients Undergoing Radical Prostatectomy for Prostate Cancer: Results from a Multicentric

European Prospective Stud. *Eur. Urol.* **2015**, *68*, 132–138.

(23) Filella, X.; Fernández-Galan, E.; Bonifacio, R. F.; Foj, L. Emerging Biomarkers in the Diagnosis of Prostate Cancer. *Pharmgenomics. Pers. Med.* **2018**, *11*, 83–94.

(24) McDonald, M. L.; Parsons, J. K. 4-Kallikrein Test and Kallikrein Markers in Prostate Cancer Screening. *Urol. Clin. North Am.* **2016**, *43*, 39–46.

(25) Cary, K. C.; Cooperberg, M. R. Biomarkers in Prostate Cancer Surveillance and Screening: Past, Present, and Future. *Ther. Adv. Urol.* **2013**, *5*, 318–329.

(26) Cui, Y.; Cao, W.; Li, Q.; Shen, H.; Liu, C.; Deng, J.; Xu, J.; Shao, Q. Evaluation of Prostate Cancer Antigen 3 for Detecting Prostate Cancer: A Systematic Review and Meta-Analysis. *Sci. Rep.* **2016**, *6*, 2–10.

(27) Taniguchi, N.; Kizuka, Y. *Glycans and Cancer: Role of N-Glycans in Cancer Biomarker, Progression and Metastasis, and Therapeutics*, 1st Edition.; Elsevier Inc., 2015; Vol. 126.

(28) Varki, A. Biological Roles of Glycans. *Glycobiology* **2017**, *27*, 3–49.

(29) Schneider, M.; Al-Shareffi, E.; Haltiwanger, R. S. Biological Functions of Fucose in Mammals. *Glycobiology* **2017**, *27*, 601–618.

(30) Pearce, O. M. T.; Läubli, H. Sialic Acids in Cancer Biology and Immunity. *Glycobiology* **2015**, *26*, 111–128.

(31) Peracaula, R.; Tabarés, G.; Royle, L.; Harvey, D. J.; Dwek, R. A.; Rudd, P. M.; de Llorens, R. Altered Glycosylation Pattern Allows the Distinction between Prostate-Specific Antigen (PSA) from Normal and Tumor Origins. *Glycobiology* **2003**, *13*, 457–470.

(32) Llop, E.; Ferrer-Batallé, M.; Barrabés, S.; Guerrero, P. E.; Ramírez, M.; Saldova, R.; Rudd, P. M.; Aleixandre, R. N.; Comet, J.; de Llorens, R.; Peracaula, R. Improvement of Prostate Cancer Diagnosis by Detecting PSA Glycosylation-Specific Changes. *Theranostics* **2016**, *6*, 1190–1204.

(33) Yoneyama, T.; Ohyama, C.; Hatakeyama, S.; Narita, S.; Habuchi, T.; Koie, T.; Mori, K.; Hidari, K. I. P. J.; Yamaguchi, M.; Suzuki, T.; Tobisawa, Y. Measurement of Aberrant Glycosylation of Prostate Specific Antigen Can Improve Specificity in Early Detection of Prostate Cancer. *Biochem. Biophys. Res. Commun.* **2014**, *448*, 390–396.

(34) Ishikawa, T.; Yoneyama, T.; Tobisawa, Y.; Hatakeyama, S.; Kurosawa, T.; Nakamura, K.; Narita, S.; Mitsuzuka, K.; Duivenvoorden, W.; Pinthus, J. H.; Hashimoto, Y.; Koie, T.; Habuchi, T.; Arai, Y.; Ohyama, C. An Automated Micro-Total Immunoassay System for

Measuring Cancer-Associated α2,3-Linked Sialyl N-Glycan-Carrying Prostate-Specific Antigen May Improve the Accuracy of Prostate Cancer Diagnosis. *Int. J. Mol. Sci.* **2017**, *18*, 470.

(35) Fukushima, K.; Satoh, T.; Baba, S.; Yamashita, K. α1,2-Fucosylated and β-N-Acetylgalactosaminylated Prostate-Specific Antigen as an Efficient Marker of Prostatic Cancer. *Glycobiology* **2010**, *20*, 452–460.

(36) Hagiwara, K.; Tobisawa, Y.; Kaya, T.; Kaneko, T.; Hatakeyama, S.; Mori, K.; Hashimoto, Y.; Koie, T.; Suda, Y.; Ohyama, C.; Yoneyama, T. *Wisteria floribunda* Agglutinin and its Reactive-Glycan-Carrying Prostate-Specific Antigen as a Novel Diagnostic and Prognostic Marker of Prostate Cancer. *Int. J. Mol. Sci.* **2017**, *18*, 261

(37) Ohyama, C.; Hosono, M.; Nitta, K.; Oh-eda, M.; Yoshikawa, K.; Habuchi, T.; Arai, Y.; Fukuda, M. Carbohydrate Structure and Differential Binding of Prostate Specific Antigen to Maackia Amurensis Lectin Between Prostate Cancer and Benign Prostate Hypertrophy. *Glycobiology* **2004**, *14*, 671-679.

(38) Etxebarria, J.; Reichardt, N. C. Methods for the Absolute Quantification of N-Glycan Biomarkers. *Biochim. Biophys. Acta - Gen. Subj.* **2016**, *1860*, 1676–1687.

(39) Tajiri, M.; Ohyama, C.; Wada, Y. Oligosaccharide Profiles of the Prostate Specific Antigen in Free and Complexed Forms from the Prostate Cancer Patient Serum and in Seminal Plasma: A Glycopeptide Approach. *Glycobiology* **2008**, *18*, 2-8.

(40) Haga, Y.; Uemura, M.; Baba, S.; Inamura, K.; Takeuchi, K.; Nonomura, N.; Ueda, K. Identification of Multisialylated LacdiNAc Structures as Highly Prostate Cancer Specific Glycan Signatures on PSA. *Anal. Chem.* **2019**, *91*, 2247–2254.

(41) Wohlschlager, T.; Scheffler, K.; Forstenlehner, I.C.; Skala, W.; Senn, S.; Damoc, E.; Holzmann, J.; Huber, C.G. Native Mass Spectrometry Combined with Enzymatic Dissection Unravels Glycoform Heterogeneity of Biopharmaceuticals. *Nat. Commu.* **2018**, *9*, 1713.

(42) Banazadeh, A.; Veillon, L.; Wooding, K.M.; Zabet-moghaddam, M.; Mechref, Y. Recent Advances in Mass Spectrometric Analysis of Glycoproteins. *Electrophoresis* **2017**, *38*, 162-189.

(43) Li, Z.; Kitov, P. I.; Han, L.; Kitova, E. N.; Mozenah, F.; Rodrigues, E.; Chapla, D. G.;

Moremen, K. W.; Macauley, M. S.; Klassen, J. S. CUPRA-ZYME: An Assay for Measuring Carbohydrate-Active Enzyme Activities, Pathways, and Substrate Specificities. *Anal. Chem.*, **2020**, *92*, 3228-3236.

(44) Gerber, S.A.; Scott, C.R.; Turecek, F.; Gelb, M.H. Analysis of Rates of Multiple Enzymes in Cell Lysates by Electrospray Ionization Mass Spectrometry. *J. Am. Chem. Soc.*, **1999**, *121*, 1102-1103.

(45) Moremen, K.W.; Ramiah, A.; Stuart, M.; Steel, J.; Meng, L.; Forouhar, F.; Moniz, H.A.; Gahlay, G.; Gao, Z.; Chapla, D.; Wang, S.; Yang, J.-Y.; Prabhakar, P.K.; Johnson, R.; Dela Rosa, M.; Geisler, C.; Nairn, A.V.; Seetharaman, J.; Wu, S.-C.; Tong, L.; Gilbert, H.J.; LaBaer, J.; Jarvis, D.L. Expression System for Structural and Functional Studies of Human Glycosylation Enzymes. *Nat. Chem. Biol.*, **2018**, *14*, 156-162.

(46) Meng, L.; Forouhar, F.; Thieker, D.; Gao, Z.; Ramiah, A.; Moniz, H.; Xiang, Y.; Seetharaman, J.; Milaninia, S.; Su, M.; Bridger, R.; Veillon, L.; Azadi, P.; Kornhaber, G.; Wells, L.; Montelione, G.T.; Woods, R.J.; Tong, L.; Moremen, K.W. Enzymatic Basis for N-glycan Sialylation: Structure of Rat α2,6-sialyltransferase (ST6Gal1) Reveals Conserved and Unique Features for Glycan Sialylation. *J. Biol. Chem.*, **2013**, *288*, 34680-34698.

(47) Kitov, P. I.; Han, L.; Kitova, E. N.; Klassen, J. S. Sliding Window Adduct Removal Method (SWARM) for Enhanced Electrospray Ionization Mass Spectrometry Binding Data. *J. Am. Soc. Mass Spectrom*, **2019**, *30*, 1446–1454.

(48) Ceroni, A.; Dell, A.; Haslam, S.M. The GlycanBuilder: A Fast, Intuitive and Flexible Software Tool for Building and Displaying Glycan Structures. *Source Code for Biology and Medicine*. **2007**, *2*, 3.

(49) Gut, H.; King, S. J.; Walsh, M. A. Structural and Functional Studies of Streptococcus Pneumoniae Neuraminidase B: An Intramolecular Trans-Sialidase. *FEBS Lett.* **2008**, *582*, 3348–3352.

(50) Luo, Y.; Li, S.C.; Li, Y.T. Luo, M. The 1.8 A° Structures of Leech Intramolecular Trans-Sialidase Complexes: Evidence of its Enzymatic Mechanism. A. *J. Mol. Biol.* **1999**, *285*, 323-332.

(51) Sarrats, A.; Saldova, R.; Comet, J.; O'Donoghue, N.; de Llorens, R.; Rudd, P.M.; Peracaula, R. Glycan Characterization of PSA 2-DE Subforms from Serum and Seminal Plasma.

OMICS, **2010**, *14*, 465-474.

(52) Anguizola, J.; Matsuda, R.; Barnaby, O.S.; Joseph, K.S.; Wa, C.; DeBolt, E.; Koke, M.; Hage, D.S. Review: Glycation of Human Serum Albumin. *Clinica Chimica Acta*. **2013**, *0*, 64-76.

(53) Tabarés, G.; Jung, K.; Reiche, J.; Stephan, C.; Lein, M.; Peracaula, R.; de Llorens, R.; Hoesel, W. Free PSA Forms in Prostatic Tissue and Sera of Prostate Cancer Patients: Analysis by 2-DE and Western Blotting of Immunopurified Samples. *Clinical Biochemistry*. **2007**, *40*, 343-350.

Chapter 4
Conclusions

4.1 Conclusions

Chapter 2 sheds light on the application of submicron emitters for reliable quantification of weak glycan-protein interactions without the requirement of a correction method to account for non-specific interactions. The emitters reduce the size of the droplet which decreases the probability of finding multi-ligand molecule in the droplet as it approaches to dryness, the net effect is a significant mitigation of non-specific interactions observed in the spectrum. This allows the ratio of the abundances of ion intensities of protein and protein-ligand complex to be directly calculated from the spectrum. The reliability of the strategy was proven using the interactions between lyz and a trisaccharide (**L1**), and P_2^{Saga} and another trisaccharide (**L2**) as model systems. P_2^{Saga}-**L2** is a weak interaction, which required ligand concentration as high as 750 μM. Non-specific binding was negligible when the submicron emitters were employed to investigate the strength of the interaction, while the P_{ref} method (a correction method) was needed to correct for non-specific binding when standard emitters were employed at the same range of ligand concentration. Moreover, the interaction of the carbohydrate recognition domain (CRD) of DC-SIGN with a tetrasaccharide (**L3**) was chosen as a model system because this is a calcium-dependent interaction, which posed a challenge regarding binding affinity measurements. As a starting point, the interaction between DC-SIGN CRD and calcium was characterized. Evidence of positive cooperativity of the binding sites of DC-SIGN CRD is unambiguously presented for the first time. The interaction between DC-SIGN CRD and **L3** was measured to be (3.7 ± 0.8) mM at physiologically relevant calcium concentration (2.5 mM), which was in agreement with the affinity reported in the literature at 4 mM Ca^{2+}. Notably, evidence of saturation of Ca^{2+} binding sites in presence of the ligand was reported in this work. This observation is in agreement with an extensive body of work suggesting the interaction requires three (3) Ca^{2+}. However, the submicron emitters allowed the calculation of the distribution of calcium ions bound to DC-SIGN CRD in presence and absence of ligand, which clearly contrasts the occupancy of the binding sites. On the other hand, the interaction of hGal-3C and lactose (**L2**) is known to be prone to in-source ion dissociation, the submicron emitters

allowed the measurement of this interaction due to their ability to mitigate non-specific binding at saturating ligand concentrations. Under this condition the missing fraction of the complex ion in the spectrum can be directly and unambiguously related to the fraction undergoing in-source dissociation, therefore, a correction factor can be used to correct for in-source dissociation. Following this strategy, the binding affinity was found to be in agreement within a factor of 2 with the affinity reported in the literature using ITC, which confirms the reliability of the submicron emitters to measure glycan-protein interactions prone to in-source dissociation.

PSA test is currently used as a blood-based method for the screening of Prostate Cancer (PCa), the second leading cost of death in the United States. However, a high rate of false-positive, lack of prognostic value and the requirement of a biopsy for diagnosis of PCa, make PSA test a controversial biomarker. Instead, carbohydrates on PSA have been found to have diagnostic and prognostic value, especially α2,3-Neu5Ac. Chapter 3 focuses on the implementation of an enzyme-aided ESI-MS-based strategy for the quantification of α2,3-Neu5Ac on PSA. The strategy takes advantage of time-resolved data collection by ESI-MS to calculate the relative abundances of asialo-PSA, monosialo-PSA and PSA during the reaction period. When reaction progress reaches a plateau, the relative abundance of asialo-PSA yields information about the content of α2,3-Neu5Ac-linked to PSA that was initially incorporated on the glycoprotein. Neuraminidase S (NeuS) was demonstrated to be an enzyme that specifically cleaves α2,3-linked Neu5Ac. CUPRA substrates, α2,3-Neu5Ac- and α2,6-Neu5Ac-linked to PSA were employed to demonstrate the specificity of the enzyme. The reliability of the method for the quantification of α2,3-Neu5Ac-linked to PSA was validated using an internal standard (Neu5Ac-$^{13}C_3$). Also, a purification method was developed for the extraction and concentration of PSA from blood serum. Yet, a limit of quantification (LOQ) experiment using female blood serum with no detectable PSA levels must be carried out to assess the PSA amount in real samples that this approach is capable of extracting and analyzing. This is a requirement to explore the application of this strategy for clinical purposes.

List of References

Chapter 1

(1) Marth, J. D. A Unified Vision of the Building Blocks of Life. *Nat. Cell Biol.* **2008**, *10*, 1015.

(2) Mariño, K.; Bones, J.; Kattla, J. J.; Rudd, P. M. A Systematic Approach to Protein Glycosylation Analysis: A Path through the Maze. *Nat. Chem. Biol.* **2010**, *6*, 713–723.

(3) Pearce, O. M. T.; Läubli, H. Sialic Acids in Cancer Biology and Immunity. *Glycobiology* **2015**, *26*, 111–128.

(4) Tachibana, H.; Taniguchi, K.; Ushio, Y.; Teruya, K.; Osada, K.; Murakami, H. Changes of Monosaccharide Availability of Human Hybridoma Lead to Alteration of Biological Properties of Human Monoclonal Antibody. *Cytotechnology* **1994**, *16*, 151–157.

(5) Cells, C. H. O.; Borys, M. C.; Linze, D. I. H.; Papoutsakis, E. T. Culture PH Affects Expression Rates and Glycosylation of Recombinant Mouse Placental Lactogen Proteins by Chines Ovary Hamster (CHO) Cells. *Nat. Biotechnol.* **1993**, *11*, 720–724.

(6) Doores, K. J.; Bonomelli, C.; Harvey, D. J.; Vasiljevic, S.; Dwek, R. A.; Burton, D. R.; Crispin, M.; Scanlan, C. N. Envelope Glycans of Immunodeficiency Virions Are Almost Entirely Oligomannose Antigens. *Proc. Natl. Acad. Sci. U. S. A.* **2010**, *107*, 13800–13805.

(7) Clark, M. C.; Baum, L. G. T Cells Modulate Glycans on CD43 and CD45 during Development and Activation, Signal Regulation, and Survival. *Ann. N. Y. Acad. Sci.* **2012**, *1253*, 58–67.

(8) Varki, A. Biological Roles of Glycans. *Glycobiology* **2017**, *27*, 3–49.

(9) Zhao, Y. Y.; Takahashi, M.; Gu, J. G.; Miyoshi, E.; Matsumoto, A.; Kitazume, S.; Taniguchi, N. Functional Roles of N-Glycans in Cell Signaling and Cell Adhesion in Cancer. *Cancer Science*. 2008, 1304–1310.

(10) Sola, R. J.; Griebenow, K. Effects of Glycosylate on the Stability of Protein Pharmaceuticals. *J. Pharm. Sci.* **2009**, *98*, 1223–1245.

(11) Lee, H. S.; Qi, Y.; Im, W. Effects of N-Glycosylation on Protein Conformation and

Dynamics: Protein Data Bank Analysis and Molecular Dynamics Simulation Study. *Sci. Rep.* **2015**, *5*, 1–7.

(12) Varki, A.; Cummings, R. D.; Esko, J . D.; Stanley, P.; Hart, G. W.; Aebi, M.; Darvill, A. G.; Kinoshita, T.; Packer, N. H.; Prestegard, J. H.; Schnaar, R. L.; Seeberger, P. H. *Essentials of Glycobiology*, 3rd edition; Cold Spring Harbor Laboratory Press: Cold Spring Harbor (NY), 2017.

(13) Cummings, R. D.; Pierce, J. M. The Challenge and Promise of Glycomics. *Chem. Biol.* **2014**, *21* (1), 1–15.

(14) Llop, E.; Ferrer-Batallé, M.; Barrabés, S.; Guerrero, P. E.; Ramírez, M.; Saldova, R.; Rudd, P. M.; Aleixandre, R. N.; Comet, J.; de Llorens, R.; Peracaula, R. Improvement of Prostate Cancer Diagnosis by Detecting PSA Glycosylation-Specific Changes. *Theranostics* **2016**, *6*, 1190–1204.

(15) Rodriguez, E.; Boelaars, K.; Brown, K.; Li, R. J.; Kruijssen, L.; Bruijns, S. C.; Schetters, S. T.; Crommentuijn, M. H.; van der Horst, J.; van Vliet, S.; Kazemier, G.; Giovannetti, E.; Garcia-Vallejo, J.J.; van Kooyk, Y. Sialic Acids in Pancreatic Cancer Drive Tumour-Associated Macrophage Differentiation via Siglec-7 and Siglec-9. *Nat. Commun.* **2021**, *12*, 1270.

(16) Stowell, S. R.; Ju, T.; Cummings, R. D. Protein Glycosylation in Cancer. *Annu. Rev. Pathol.* **2015**, *10*, 473–510.

(17) Solá, R. J.; Griebenow, K. Glycosylation of Therapeutic Proteins: An Effective Strategy to Optimize Efficacy. *BioDrugs* **2010**, *24*, 9–21.

(18) Liu, L. Antibody Glycosylation and Its Impact on the Pharmacokinetics and Pharmacodynamics of Monoclonal Antibodies and Fc-Fusion Proteins. *J. Pharm. Sci.* **2015**, *104*, 1866–1884.

(19) Boune, S.; Hu, P.; Epstein, A. L.; Khawli, L. A. Principles of N-Linked Glycosylation Variations of IgG-Based Therapeutics: Pharmacokinetic and Functional Considerations. *Antibodies* **2020**, *9*, 22.

(20) Liang, Y. Applications of Isothermal Titration Calorimetry in Protein Science. *Acta Biochim. Biophys. Sin. (Shanghai).* **2008**, *40*, 565–576.

(21) Dam, T. K.; Brewer, C. F. Thermodynamic Studies of Lectin−Carbohydrate Interactions by Isothermal Titration Calorimetry. *Chem. Rev.* **2002**, *102*, 387–430.

(22) Torres, F. E.; Recht, M. I.; Coyle, J. E.; Bruce, R. H.; Williams, G. Higher Throughput Calorimetry: Opportunities, Approaches and Challenges. *Curr. Opin. Struct. Biol*. 2010, *20*, 598–605.

(23) Rajarathnam, K.; Rösgen, J. Isothermal Titration Calorimetry of Membrane Proteins - Progress and Challenges. *Biochim. Biophys. Acta - Biomembr.* **2014**, *1838*, 69–77.

(24) De Crescenzo, G.; Boucher, C.; Durocher, Y.; Jolicoeur, M. Kinetic Characterization by Surface Plasmon Resonance-Based Biosensors: Principle and Emerging Trends. *Cell. Mol. Bioeng.* **2008**, *1*, 204–215.

(25) Myszka, D. G. Kinetic Analysis of Macromolecular Interactions Using Surface Plasmon Resonance Biosensors. *Curr. Opin. Biotechnol.* **1997**, *8*, 50–57.

(26) Morton, T. A.; Myszka, D. G. Kinetic Analysis of Macromolecular Interactions Using Surface Plasmon Resonance Biosensors. *Methods Enzymol.* **1998**, *295*, 268–282.

(27) Curie, P. Dilatation Électrique Du Quartz Pierre Curie To Cite This Version : HAL Id : Jpa-00238937. *J. Phys. Theor. Appl.* **1889**, *8*, 149–168.

(28) Sandoval, P. J.; Santiago, J. In Vitro Analytical Approaches to Study Plant Ligand-Receptor Interactions. *Plant Physiol.* **2020**, *182*, 1697–1712.

(29) Nomura, T.; Hattori, O. Determination of Micromolar Concentrations of Cyanide in Solution with a Piezoelectric Detector. *Anal. Chim. Acta* **1980**, *115*, 323–326.

(30) Dixon, M. C. Quartz Crystal Microbalance with Dissipation Monitoring: Enabling Real-Time Characterization of Biological Materials and Their Interactions. *J. Biomol. Tech.* **2008**, *19*, 151–158.

(31) Vogt, S.; Kelkenberg, M.; Nöll, T.; Steinhoff, B.; Schönherr, H.; Merzendorfer, H.; Nöll, G. Rapid Determination of Binding Parameters of Chitin Binding Domains Using Chitin-Coated Quartz Crystal Microbalance Sensor Chips. *Analyst* **2018**, *143*, 5255–5263.

(32) Howlett, G. J.; Minton, A. P.; Rivas, G. Analytical Ultracentrifugation for the Study of Protein Association and Assembly. *Curr. Opin. Chem. Biol.* **2006**, *10*, 430–436.

(33) Schuck, P. Analytical Ultracentrifugation as a Tool for Studying Protein Interactions. *Biophys. Rev.* **2013**, *5*, 159–171.

(34) Edwards, G. B.; Muthurajan, U. M.; Bowerman, S.; Luger, K. Analytical Ultracentrifugation (AUC): An Overview of the Application of Fluorescence and Absorbance AUC to the Study of Biological Macromolecules. *Curr. Protoc. Mol. Biol.*

2020, *133*, e131.

(35) Schaller, G. E.; Bleecker, A. B. Ethylene-Binding Sites Generated in Yeast Expressing the Arabidopsis ETR1. *Science* **1995**, *270*, 1809–1811.

(36) Hoare, S. R. J.; Usdin, T. B. Quantitative Cell Membrane-Based Radioligand Binding Assays for Parathyroid Hormone Receptors. *J. Pharmacol. Toxicol. Methods* **1999**, *41*, 83–90.

(37) Maguire, J. J.; Kuc, R. E.; Davenport, A. P. *Book: Methods in Molecular Biology, Receptor Binding Techniques by Davenport, A.P. (Ed). Chapther 3: Radioligand Binding Assays and Their Analysis. 31-78*; 2012; Vol. 897.

(38) Onizuka, T.; Shimizu, H.; Moriwaki, Y.; Nakano, T.; Kanai, S.; Shimada, I.; Takahashi, H. NMR Study of Ligand Release from Asialoglycoprotein Receptor under Solution Conditions in Early Endosomes. *FEBS J.* **2012**, *279*, 2645–2656.

(39) Valverde, P.; Delgado, S.; Martínez, J. D.; Vendeville, J. B.; Malassis, J.; Linclau, B.; Reichardt, N. C.; Cañada, F. J.; Jiménez-Barbero, J.; Ardá, A. Molecular Insights into DC-SIGN Binding to Self-Antigens: The Interaction with the Blood Group A/B Antigens. *ACS Chem. Biol.* **2019**, *14*, 1660–1671.

(40) Cala, O.; Guillière, F.; Krimm, I. NMR-Based Analysis of Protein-Ligand Interactions. *Anal. Bioanal. Chem.* **2014**, *406*, 943–956.

(41) Becker, W.; Bhattiprolu, K. C.; Gubensäk, N.; Zangger, K. Investigating Protein–Ligand Interactions by Solution Nuclear Magnetic Resonance Spectroscopy. *ChemPhysChem* **2018**, *19*, 895–906.

(42) Masson, G. R.; Burke, J. E.; Ahn, N. G.; Anand, G. S.; Borchers, C.; Brier, S.; Bou-Assaf, G. M.; Engen, J. R.; Englander, S. W.; Faber, J.; *et al*. Recommendations for Performing, Interpreting and Reporting Hydrogen Deuterium Exchange Mass Spectrometry (HDX-MS) Experiments. *Nat. Methods* **2019**, *16*, 595–602.

(43) Masson, G. R.; Jenkins, M. L.; Burke, J. E. An Overview of Hydrogen Deuterium Exchange Mass Spectrometry (HDX-MS) in Drug Discovery. *Expert Opin. Drug Discov.* **2017**, *12*, 981–994.

(44) Zhang, J.; Kitova, E. N.; Li, J.; Eugenio, L.; Ng, K.; Klassen, J. S. Localizing Carbohydrate Binding Sites in Proteins Using Hydrogen/Deuterium Exchange Mass Spectrometry. *J. Am. Soc. Mass Spectrom.* **2016**, *27*, 83–90.

(45) Deng, L.; Sun, N.; Kitova, E. N.; Klassen, J. S. Direct Quantification of Protein-Metal Ion Affinities by Electrospray Ionization Mass Spectrometry. *Anal. Chem.* **2010**, *82*, 2170–2174.

(46) Kitova, E. N.; El-Hawiet, A.; Schnier, P. D.; Klassen, J. S. Reliable Determinations of Protein-Ligand Interactions by Direct ESI-MS Measurements. Are We There Yet? *J. Am. Soc. Mass Spectrom.* **2012**, *23*, 431–441.

(47) Han, L.; Tan, M.; Xia, M.; Kitova, E. N.; Jiang, X.; Klassen, J. S. Gangliosides Are Ligands for Human Noroviruses. *J. Am. Chem. Soc.* **2014**, *136*, 12631–12637.

(48) Han, L.; Shams-Ud-Doha, K.; Kitova, E. N.; Klassen, J. S. Screening Oligosaccharide Libraries against Lectins Using the Proxy Protein Electrospray Ionization Mass Spectrometry Assay. *Anal. Chem.* **2016**, *88*, 8224–8231.

(49) Shams-Ud-Doha, K.; Kitova, E. N.; Kitov, P. I.; St-Pierre, Y.; Klassen, J. S. Human Milk Oligosaccharide Specificities of Human Galectins. Comparison of Electrospray Ionization Mass Spectrometry and Glycan Microarray Screening Results. *Anal. Chem.* **2017**, *89*, 4914–4921.

(50) El-Hawiet, A.; Chen, Y.; Shams-Ud-Doha, K.; Kitova, E. N.; St-Pierre, Y.; Klassen, J. S. High-Throughput Label- and Immobilization-Free Screening of Human Milk Oligosaccharides Against Lectins. *Anal. Chem.* **2017**, *89*, 8713–8722.

(51) Wang, Y.; Park, H.; Lin, H.; Kitova, E. N.; Klassen, J. S. Multipronged ESI-MS Approach for Studying Glycan-Binding Protein Interactions with Glycoproteins. *Anal. Chem.* **2019**, *91*, 2140–2147.

(52) Rademacher, C.; Shoemaker, G. K.; Kim, H. S.; Zheng, R. B.; Taha, H.; Liu, C.; Nacario, R. C.; Schriemer, D. C.; Klassen, J. S.; Peters, T.; et al. Ligand Specificity of CS-35, a Monoclonal Antibody That Recognizes Mycobacterial Lipoarabinomannan: A Model System for Oligofuranoside-Protein Recognition. *J. Am. Chem. Soc.* **2007**, *129*, 10489–10502.

(53) Yao, Y.; Shams-Ud-Doha, K.; Daneshfar, R.; Kitova, E. N.; Klassen, J. S. Quantifying Protein-Carbohydrate Interactions Using Liquid Sample Desorption Electrospray Ionization Mass Spectrometry. *J. Am. Soc. Mass Spectrom.* **2015**, *26*, 98–106.

(54) Konermann, L.; Ahadi, E.; Rodriguez, A. D.; Vahidi, S. Unraveling the Mechanism of Electrospray Ionization. *Anal. Chem.* **2013**, *85*, 2–9.

(55) Kebarle, P.; Verkcerk, U. H. Electrospray: From Ions in Solution to Ions in the Gas Phase, What We Know Now. *Mass Spectrom. Rev.* **2009**, *28*, 898–917.

(56) Loeb, L. B.; Kip, A. F.; Hudson, G. G.; Bennett, W. H. Pulses in Negative Point-to-Plane Corona. *Phys. Rev.* **1941**, *60*, 714–722.

(57) Taylor, G. I.; Mcewan, A. D. The Stability of a Horizontal Fluid Interface in a Vertical Electric Field. *J. Fluid Mech.* **1965**, *22*, 1–15.

(58) Fernández de la Mora, J. The Fluid Dynamics of Taylor Cones. *Annu. Rev. Fluid Mech.* **2007**, *39*, 217–243.

(59) Iribarne, J. V.; Thomson, B. A. On the Evaporation of Small Ions from Charged Droplets. *J. Chem. Phys.* **1976**, *64*, 2287–2294.

(60) Thomson, B. A.; Iribarne, J. V. Field Induced Ion Evaporation from Liquid Surfaces at Atmospheric Pressure. *J. Chem. Phys.* **1979**, *71*, 4451–4463.

(61) Konermann, L.; Ahadi, E.; Rodriguez, A. D.; Vahidi, S. Unraveling the Mechanism of Electrospray Ionization. *Anal. Chem.* **2013**, *85*, 2–9.

(62) Metwally, H.; Duez, Q.; Konermann, L. Chain Ejection Model for Electrospray Ionization of Unfolded Proteins: Evidence from Atomistic Simulations and Ion Mobility Spectrometry. *Anal. Chem.* **2018**, *90*, 10069–10077.

(63) Konermann, L.; Rodriguez, A. D.; Liu, J. On the Formation of Highly Charged Gaseous Ions from Unfolded Proteins by Electrospray Ionization. *Anal. Chem.* **2012**, *84*, 6798–6804.

(64) Miller, P. E.; Denton, M. B. The Quadrupole Mass Filter: Basic Operating Concepts. *J. Chem. Educ.* **1986**, *63*, 617.

(65) Gross, J. H. *Mass Spectrometry*; Springer International Publishing: Cham, 2017; Vol. 56.

(66) Zubarev, R. A.; Makarov, A. Orbitrap Mass Spectrometry. *Anal. Chem.* **2013**, *85*, 5288–5296.

(67) Hecht, E. S.; Scigelova, M.; Eliuk, S.; Makarov, A. *Fundamentals and Advances of Orbitrap Mass Spectrometry*; 2019.

(68) Wang, W.; Kitova, E. N.; Klassen, J. S. Influence of Solution and Gas Phase Processes on Protein-Carbohydrate Binding Affinities Determined by Nanoelectrospray Fourier Transform Ion Cyclotron Resonance Mass Spectrometry. *Anal. Chem.* **2003**, *75*, 4945–4955.

(69) El-Hawiet, A.; Kitova, E. N.; Liu, L.; Klassen, J. S. Quantifying Labile Protein-Ligand Interactions Using Electrospray Ionization Mass Spectrometry. *J. Am. Soc. Mass Spectrom.* **2010**, *21*, 1893–1899.

(70) Sun, J.; Kitova, E. N.; Klassen, J. S. Method for Stabilizing Protein-Ligand Complexes in Nanoelectrospray Ionization Mass Spectrometry. *Anal. Chem.* **2007**, *79*, 416–425.

(71) Liu, L.; Kitova, E. N.; Klassen, J. S. Quantifying Protein-Fatty Acid Interactions Using Electrospray Ionization Mass Spectrometry. *J. Am. Soc. Mass Spectrom.* **2011**, *22*, 310–318.

(72) Bagal, D.; Kitova, E. N.; Liu, L.; El-Hawiet, A.; Schnier, P. D.; Klassen, J. S. Gas Phase Stabilization of Noncovalent Protein Complexes Formed by Electrospray Ionization. *Anal. Chem.* **2009**, *81*, 7801–7806.

(73) Gabelica, V.; Galic, N.; Rosu, F.; Houssier, C.; De Pauw, E. Influence of Response Factors on Determining Equilibrium Association Constants of Non-Covalent Complexes by Electrospray Ionization Mass Spectrometry. *J. Mass Spectrom.* **2003**, *38*, 491–501.

(74) Kitova, E. N.; Kitov, P. I.; Paszkiewicz, E.; Kim, J.; Mulvey, G. L.; Armstrong, G. D.; Bundle, D. R.; Klassen, J. S. Affinities of Shiga Toxins 1 and 2 for Univalent and Oligovalent Pk-Trisaccharide Analogs Measured by Electrospray Ionization Mass Spectrometry. *Glycobiology* **2007**, *17*, 1127–1137.

(75) Chitta, R. K.; Rempel, D. L.; Gross, M. L. Determination of Affinity Constants and Response Factors of the Noncovalent Dimer of Gramicidin by Electrospray Ionization Mass Spectrometry and Mathematical Modeling. *J. Am. Soc. Mass Spectrom.* **2005**, *16*, 1031–1038.

(76) Lin, H.; Kitova, E. N.; Klassen, J. S. Quantifying Protein-Ligand Interactions by Direct Electrospray Ionization-Ms Analysis: Evidence of Nonuniform Response Factors Induced by High Molecular Weight Molecules and Complexes. *Anal. Chem.* **2013**, *85*, 8919–8922.

(77) Hossain, B. M.; Konermann, L. Pulsed Hydrogen/Deuterium Exchange MS/MS for Studying the Relationship between Noncovalent Protein Complexes in Solution and in the Gas Phase after Electrospray Ionization. *Anal. Chem.* **2006**, *78*, 1613–1619.

(78) Wang, W.; Kitova, E. N.; Klassen, J. S. Nonspecific Protein-Carbohydrate Complexes Produced by Nanoelectrospray Ionization. Factors Influencing Their Formation and Stability. *Anal. Chem.* **2005**, *77*, 3060–3071.

(79) Wang, W.; Kitova, E. N.; Klassen, J. S. Nonspecific Protein-Carbohydrate Complexes Produced by Nanoelectrospray Ionization. Factors Influencing Their Formation and Stability. *Anal. Chem.* **2005**, *77*, 3060–3071.

(80) Wang, W.; Kitova, E. N.; Klassen, J. S. Bioactive Recognition Sites May Not Be Energetically Preferred in Protein-Carbohydrate Complexes in the Gas Phase. *J. Am. Chem. Soc.* **2003**, *125*, 13630–13631.

(81) Sun, J.; Kitova, E. N.; Wang, W.; Klassen, J. S. Method for Distinguishing Specific from Nonspecific Protein-Ligand Complexes in Nanoelectrospray Ionization Mass Spectrometry. *Anal. Chem.* **2006**, *78*, 3010–3018.

(82) Shimon, L.; Sharon, M.; Horovitz, A. A Method for Removing Effects of Nonspecific Binding on the Distribution of Binding Stoichiometries: Application to Mass Spectroscopy Data. *Biophys. J.* **2010**, *99*, 1645–1649.

(83) Sun, N.; Soya, N.; Kitova, E. N.; Klassen, J. S.; Ab, P. Nonspecific Interactions Between Proteins and Charged Biomolecules in Electrospray. *J. Am. Soc. Mass Spectrom.* **2010**, *21*, 472-481.

(84) Sun, J.; Kitova, E. N.; Sun, N.; Klassen, J. S. Method for Identifying Nonspecific Protein-Protein Interactions in Nanoelectrospray Ionization Mass Spectrometry. *Anal. Chem.* **2007**, *79*, 9301–9311.

(85) Han, L.; Zheng, R.; Richards, M. R.; Tan, M.; Kitova, E. N.; Jiang, X.; Klassen, J. S. Quantifying the Binding Stoichiometry and Affinity of Histo-Blood Group Antigen Oligosaccharides for Human Noroviruses. *Glycobiology* **2018**, *28*, 488–498.

(86) Balk, S. P.; Ko, Y. J.; Bubley, G. J. Biology of Prostate-Specific Antigen. *J. Clin. Oncol.* **2003**, *21*, 383–391.

(87) Sotiropoulou, G.; Pampalakis, G.; Diamandis, E. P. Functional Roles of Human Kallikrein-Related Peptidases. *J. Biol. Chem.* **2009**, *284*, 32989–32994.

(88) O'Reilly, J.-A. Prostate Cancer Detection: Complexities and Strategies. *J. Cancer Treat. Diagnosis* **2017**, *2*, 18–25.

(89) Tabarés, G.; Radcliffe, C. M.; Barrabés, S.; Ramírez, M.; Aleixandre, N.; Hoesel, W.; Dwek, R. A.; Rudd, P. M.; Peracaula, R.; de Llorens, R. Different Glycan Structures in Prostate-Specific Antigen from Prostate Cancer Sera in Relation to Seminal Plasma PSA. *Glycobiology* **2006**, *16*, 132–145.

(90) Tkac, J.; Gajdosova, V.; Hroncekova, S.; Bertok, T.; Hires, M.; Jane, E.; Lorencova, L.; Kasak, P. Prostate-Specific Antigen Glycoprofiling as Diagnostic and Prognostic Biomarker of Prostate Cancer. *Interface Focus* **2019**, *9*.

(91) Lilja, H.; Ulmert, D.; Vickers, A. J. Prostate-Specific Antigen and Prostate Cancer: Prediction, Detection and Monitoring. *Nat. Rev. Cancer* **2008**, *8*, 268–278.

(92) Punnen, S.; Pavan, N.; Parekh, D. J. Finding the Wolf in Sheep's Clothing: The 4Kscore Is a Novel Blood Test That Can Accurately Identify the Risk of Aggressive Prostate Cancer. *Rev. Urol.* **2015**, *17*, 3–13.

(93) Peracaula, R.; Tabarés, G.; Royle, L.; Harvey, D. J.; Dwek, R. A.; Rudd, P. M.; de Llorens, R. Altered Glycosylation Pattern Allows the Distinction between Prostate-Specific Antigen (PSA) from Normal and Tumor Origins. *Glycobiology* **2003**, *13*, 457–470.

(94) Etxebarria, J.; Reichardt, N. C. Methods for the Absolute Quantification of N-Glycan Biomarkers. *Biochim. Biophys. Acta - Gen. Subj.* **2016**, *1860*, 1676–1687.

(95) Wohlschlager, T.; Scheffler, K.; Forstenlehner, I.C.; Skala, W.; Senn, S.; Damoc, E.; Holzmann, J.; Huber, C.G. Native mass spectrometry combined with enzymatic dissection unravels glycoform heterogeneity of biopharmaceuticals. *Nat. Commu.* **2018**, *9*, 1713.

(96) Banazadeh, A.; Veillon, L.; Wooding, K.M.; Zabet-moghaddam, M.; Mechref, Y. Recent advances in mass spectrometric analysis of glycoproteins. *Electrophoresis* **2017**, *38*, 162-189.

Chapter 2

(1) Varki, A. Biological Roles of Glycans. *Glycobiology* **2017**, *27*, 3–49.

(2) Li, J.; Fan, X.; Kitova, E. N.; Zou, C.; Cairo, C. W.; Eugenio, L.; Ng, K. K. S.; Xiong, Z. J.; Privé, G. G.; Klassen, J. S. Screening Glycolipids Against Proteins in Vitro Using Picodiscs and Catch-and-Release Electrospray Ionization-Mass Spectrometry. *Anal. Chem*. **2016**, *88*, 4742–4750.

(3) Shams-Ud-Doha, K.; Kitova, E. N.; Kitov, P. I.; St-Pierre, Y.; Klassen, J. S. Human Milk Oligosaccharide Specificities of Human Galectins. Comparison of Electrospray Ionization Mass Spectrometry and Glycan Microarray Screening Results. *Anal. Chem*. **2017**, *89*, 4914–4921.

(4) Fiege, B.; Rademacher, C.; Cartmell, J.; Kitov, P. I.; Parra, F.; Peters, T. Molecular Details

of the Recognition of Blood Group Antigens by a Human Norovirus as Determined by STD NMR Spectroscopy. *Angew. Chemie - Int. Ed.* **2012**, *51*, 928–932.

(5) Mallagaray, A.; Lockhauserbäumer, J.; Hansman, G.; Uetrecht, C.; Peters, T. Attachment of Norovirus to Histo Blood Group Antigens: A Cooperative Multistep Process. *Angew. Chemie - Int. Ed.* **2015**, *54*, 12014–12019.

(6) Han, L.; Zheng, R.; Richards, M. R.; Tan, M.; Kitova, E. N.; Jiang, X.; Klassen, J. S. Quantifying the Binding Stoichiometry and Affinity of Histo-Blood Group Antigen Oligosaccharides for Human Noroviruses. *Glycobiology* **2018**, *28*, 488–498.

(7) Syedbasha, M.; Linnik, J.; Santer, D.; O'Shea, D.; Barakat, K.; Joyce, M.; Khanna, N.; Lorne Tyrrell, D.; Houghton, M.; Egli, A. An ELISA Based Binding and Competition Method to Rapidly Determine Ligand-Receptor Interactions. *J. Vis. Exp.* **2016**, *109*, 1–10.

(8) Safina, G. Application of Surface Plasmon Resonance for the Detection of Carbohydrates, Glycoconjugates, and Measurement of the Carbohydrate-Specific Interactions: A Comparison with Conventional Analytical Techniques. A Critical Review. *Anal. Chim. Acta* **2012**, *712*, 9–29.

(9) Helmerhorst, E.; Chandler, D. J.; Nussio, M.; Mamotte, C. D. Real-time and Label-free Bio-sensing of Molecular Interactions by Surface Plasmon Resonance: A Laboratory Medicine Perspective. *Clin. Biochem. Rev.* **2012**, *33*, 161–173.

(10) Han, L.; Tan, M.; Xia, M.; Kitova, E. N.; Jiang, X.; Klassen, J. S. Gangliosides are Ligands for Human Noroviruses. *J. Am. Chem. Soc.* **2014**, *136*, 12631–12637.

(11) El-Hawiet, A.; Kitova, E. N.; Klassen, J. S. Quantifying Carbohydrate-Protein Interactions by Electrospray Ionization Mass Spectrometry Analysis. *Biochemistry* **2012**, *51*, 4244–4253.

(12) Wang, Y.; Park, H.; Lin, H.; Kitova, E. N.; Klassen, J. S. Multipronged ESI-MS Approach for Studying Glycan-Binding Protein Interactions with Glycoproteins. *Anal. Chem.* **2019**, *91*, 2140–2147.

(13) Wang, W.; Kitova, E. N.; Klassen, J. S. Influence of Solution and Gas Phase Processes on Protein-Carbohydrate Binding Affinities Determined by Nanoelectrospray Fourier Transform Ion Cyclotron Resonance Mass Spectrometry. *Anal. Chem.* **2003**, *75*, 4945–4955.

(14) Yao, Y.; Shams-ud-doha, K.; Daneshfar, R.; Kitova, E. N.; Klassen, J. S. Quantifying

Protein-Carbohydrate Interactions using Liquid Sample Desorption Electrospray Ionization Mass Spectrometry. *J. Am. Soc. Mass Spectrom.* **2014**, *26*, 98–106.

(15) Wang, W.; Kitova, E. N.; Klassen, J. S. Nonspecific Protein-Carbohydrate Complexes Produced by Nanoelectrospray Ionization. Factors Influencing their Formation and Stability. *Anal. Chem.* **2005**, *77*, 3060–3071.

(16) Kitova, E. N.; El-Hawiet, A.; Schnier, P. D.; Klassen, J. S. Reliable Determinations of Protein-Ligand Interactions by Direct ESI-MS Measurements. Are We There Yet? *J. Am. Soc. Mass Spectrom.* **2012**, *23*, 431–441.

(17) Kebarle, P.; Verkcerk, U. H. Electrospray: From Ions in Solution to Ions in the Gas Phase, What We Know. *Mass Spectrom. Rev.* **2009**, *28*, 898–917.

(18) Sun, J.; Kitova, E. N.; Wang, W.; Klassen, J. S. Method for Distinguishing Specific from Nonspecific Protein-Ligand Complexes in Nanoelectrospray Ionization Mass Spectrometry. *Anal. Chem.* **2006**, *78*, 3010–3018.

(19) Shimon, L.; Sharon, M.; Horovitz, A. A Method for Removing Effects of Nonspecific Binding on the Distribution of Binding Stoichiometries: Application to Mass Spectroscopy Data. *Biophys. J.* **2010**, *99*, 1645–1649.

(20) Schmidt, A.; Karas, M.; Dülcks, T. Effect of Different Solution Flow Rates on Analyte Ion Signals in nano-ESI MS, or: When does ESI turn into nano-ESI? *J. Am. Soc. Mass Spectrom.* **2003**, *14*, 492–500.

(21) Davidson, K. L.; Oberreit, D. R.; Hogan Jr., C. J.; Bush, M. F. Nonspecific Aggregation in Native Electrokinetic Nanoelectrospray Ionization. *Int. J. Mass Spectrom.* **2017**, *420*, 35–42.

(22) Hollerbach, A.; Logsdon, D.; Iyer, K.; Li, A.; Schaber, J. A.; Graham Cooks, R. Sizing sub-Diffraction Limit Electrosprayed Droplets by Structured Illumination Microscopy. *Analyst* **2018**, *143*, 232–240.

(23) Li, Y.; Cole, R. B. Shifts in Peptide and Protein Charge State Distributions with Varying Spray Tip Orifice Diameter in Nanoelectrospray Fourier Transform Ion Cyclotron Resonance Mass Spectrometry. *Anal. Chem.* **2003**, *75*, 5739–5746.

(24) Mortensen, D. N.; Williams, E. R. Ultrafast (1 ms) Mixing and Fast Protein Folding in Nanodrops Monitored by Mass Spectrometry. *J. Am. Chem. Soc.* **2016**, *138*, 3453–3460.

(25) Xia, Z.; Williams, E. R. Effect of Droplet Lifetime on Where Ions Are Formed in

Electrospray Ionization. *Analyst* **2019**, *144*, 237–248.

(26) Yuill, E. M.; Sa, N.; Ray, S. J.; Hieftje, G. M.; Baker, L. A. Electrospray Ionization from Nanopipette Emitters with Tip Diameters of Less than 100 nm. *Anal. Chem.* **2013**, *85*, 8498–8502.

(27) Panczyk, E. M.; Gilbert, J. D.; Jagdale, G. S.; Stiving, A. Q.; Baker, L. A.; Wysocki, V. H. Ion Mobility and Surface Collisions: Submicrometer Capillaries Can Produce Native-like Protein Complexes. *Anal. Chem.* **2020**, *92*, 2460–2467.

(28) Susa, A. C.; Xia, Z.; Williams, E. R. Small Emitter Tips for Native Mass Spectrometry of Proteins and Protein Complexes from Nonvolatile Buffers That Mimic the Intracellular Environment. *Anal. Chem.* **2017**, *89*, 3116–3122.

(29) Susa, A. C.; Xia, Z.; Williams, E. R. Native Mass Spectrometry from Common Buffers with Salts That Mimic the Extracellular Environment. *Angew. Chemie - Int. Ed.* **2017**, *56*, 7912–7915.

(30) Susa, A. C.; Lippens, J. L.; Xia, Z.; Loo, J. A.; Campuzano, I. D. G.; Williams, E. R. Submicrometer Emitter ESI Tips for Native Mass Spectrometry of Membrane Proteins in Ionic and Nonionic Detergents. *J. Am. Soc. Mass Spectrom.* **2018**, *29*, 203–206.

(31) Nguyen, G. T. H.; Tran, T. N.; Podgorski, M. N.; Bell, S. G.; Supuran, C. T.; Donald, W. A. Nanoscale Ion Emitters in Native Mass Spectrometry for Measuring Ligand-Protein Binding Affinities. *ACS Cent. Sci.* **2019**, *5*, 308–318.

(32) Mitchell, D. A.; Fadden, A. J.; Drickamer, K. A Novel Mechanism of Carbohydrate Recognition by the C-Type Lectins DC-SIGN and DC-SIGNR. *J. Biol. Chem.* **2001**, *276*, 28939–28945.

(33) Kitov, P. I.; Han, L.; Kitova, E. N.; Klassen, J. S. Sliding Window Adduct Removal Method (SWARM) for Enhanced Electrospray Ionization Mass Spectrometry Binding Data. *J. Am. Soc. Mass Spectrom*, **2019**, *30*, 1446–1454.

(34) Pöhlmann, S.; Baribaud, F.; Lee, B.; Leslie, G. J.; Sanchez, M. D.; Hiebenthal-Millow, K.; Münch, J.; Kirchhoff, F.; Doms, R. W. DC-SIGN Interactions with Human Immunodeficiency Virus Type 1 and 2 and Simian Immunodeficiency Virus. *J. Virol.* **2001**, *75*, 4664–4672.

(35) Van Kooyk, Y.; Geijtenbeek, T. B. H. Escape Mechanism for Pathogens. *Nat. Rev. Immunol.* **2003**, *3*, 697–709.

(36) Feinberg, H.; Guo, Y.; Mitchell, D. A.; Drickamer, K.; Weis, W. I. Extended Neck Regions Stabilize Tetramers of the Receptors DC-SIGN and DC-SIGNR. *J. Biol. Chem.* **2005**, *280*, 1327–1335.

(37) Noll, A. J.; Yu, Y.; Lasanajak, Y.; Duska-McEwen, G.; Buck, R. H.; Smith, D. F.; Cummings, R. D. Human DC-SIGN Binds Specific Human Milk Glycans. *Biochem. J.* **2016**, *473*, 1343–1353.

(38) Feinberg, H.; Mitchell, D. A.; Drickamer, K.; Weis, W. I. Structural Basis for Selective Recognition of Oligosaccharides by DC-SIGN and DC-SIGNR. *Science* **2001**, *294*, 2163–2166.

(39) Guo, Y.; Feinberg, H.; Conroy, E.; Mitchell, D. A.; Alvarez, R.; Blixt, O.; Taylor, M. E.; Weis, W. I.; Drickamer, K. Structural Basis for Distinct Ligand-Binding and Targeting Properties of the Receptors DC-SIGN and DC-SIGNR. *Nat. Struct. Mol. Biol.* **2004**, *11*, 591–598.

(40) Snyder, G. A.; Colonna, M.; Sun, P. D. The Structure of DC-SIGNR with a Portion of Its Repeat Domain Lends Insights to Modeling of the Receptor Tetramer. *J. Mol. Biol.* **2005**, *347*, 979–989.

(41) Holla, A.; Skerra, A. Comparative Analysis Reveals Selective Recognition of Glycans by the Dendritic Cell Receptors DC-SIGN and Langerin. *Protein Eng. Des. Sel.* **2011**, *24*, 659–669.

(42) Van Liempt, E.; Bank, C. M. C.; Mehta, P.; García-Vallejo, J. J.; Kawar, Z. S.; Geyer, R.; Alvarez, R. A.; Cummings, R. D.; Van Kooyk, Y.; Van Die, I. Specificity of DC-SIGN for mannose□ and fucose□containing glycans. *FEBS Letters* **2006**, *580*, 6123-6131

(43) Valverde, P.; Delgado, S.; Martínez, J. D.; Vendeville, J. B.; Malassis, J.; Linclau, B.; Reichardt, N. C.; Cañada, F. J.; Jiménez-Barbero, J.; Ardá, A. Molecular Insights into DC-SIGN Binding to Self-Antigens: The Interaction with the Blood Group A/B Antigens. *ACS Chem. Biol.* **2019**, *14*, 1660–1671.

(44) Sindrewicz, P.; Li, X.; Yates, E. A.; Turnbull, J. E.; Lian, L.-Y.; Yu, L.-G. Intrinsic Tryptophan Fluorescence Spectroscopy Reliably Determines Galectin-Ligand Interactions. *Sci. Rep.* **2019**, *9*, 11851.

(45) Li, Q. Application of Fragment-Based Drug Discovery to Versatile Targets. *Front. Mol. Biosci.* **2020**, *7*, 180.

Chapter 3

(1) Siegel, R. L.; Miller, K. D.; Jemal, A. Cancer Statistics, 2020. *CA. Cancer J. Clin.* **2020**, *70*, 7–30.

(2) O'Reilly, J.-A. Prostate Cancer Detection: Complexities and Strategies. *J. Cancer Treat. Diagnosis* **2017**, *2*, 18–25.

(3) Guo, S.; Briza, P.; Magdolen, V.; Brandstetter, H.; Goettig, P. Activation and Activity of Glycosylated KLKs 3, 4 and 11. *Biol. Chem.* **2018**, *399*, 1009–1022.

(4) Balk, S. P.; Ko, Y. J.; Bubley, G. J. Biology of Prostate-Specific Antigen. *J. Clin. Oncol.* **2003**, *21*, 383–391.

(5) Sotiropoulou, G.; Pampalakis, G.; Diamandis, E. P. Functional Roles of Human Kallikrein-Related Peptidases. *J. Biol. Chem.* **2009**, *284*, 32989–32994.

(6) Mikolajczyk, S. D.; Marks, L. S.; Partin, A. W.; Rittenhouse, H. G. Free Prostate-Specific Antigen in Serum Is Becoming More Complex. *Urology* **2002**, *59*, 797–802.

(7) Gratacós-Mulleras, A.; Duran, A.; Asadi Shehni, A.; Ferrer-Batallé, M.; Ramírez, M.; Comet, J.; de Llorens, R.; Saldova, R.; Llop, E.; Peracaula, R. Characterisation of the Main PSA Glycoforms in Aggressive Prostate Cancer. *Sci. Rep.* **2020**, *10*, 1–14.

(8) Punnen, S.; Pavan, N.; Parekh, D. J. Finding the Wolf in Sheep's Clothing: The 4Kscore Is a Novel Blood Test That Can Accurately Identify the Risk of Aggressive Prostate Cancer. *Rev. Urol.* **2015**, *17*, 3–13.

(9) Butch, A. W.; Crary, D.; Yee, M. Analytical Performance of the Roche Total and Free PSA Assays on the Elecsys 2010 Immunoanalyzer. *Clin. Biochem.* **2002**, *35*, 143–145.

(10) Rodriguez, J. Z.; O'Kennedy, R. New Approaches for the Development of Diagnostic Systems for Prostate Cancer. *Asian Hosp. Heal. Manag.* **2017**, *36*, 18–23.

(11) Tabarés, G.; Radcliffe, C. M.; Barrabés, S.; Ramírez, M.; Aleixandre, N.; Hoesel, W.; Dwek, R. A.; Rudd, P. M.; Peracaula, R.; de Llorens, R. Different Glycan Structures in Prostate-Specific Antigen from Prostate Cancer Sera in Relation to Seminal Plasma PSA. *Glycobiology* **2006**, *16*, 132–145.

(12) Tkac, J.; Gajdosova, V.; Hroncekova, S.; Bertok, T.; Hires, M.; Jane, E.; Lorencova, L.;

Kasak, P. Prostate-Specific Antigen Glycoprofiling as Diagnostic and Prognostic Biomarker of Prostate Cancer. *Interface Focus* **2019**, *9*.

(13) Lilja, H.; Ulmert, D.; Vickers, A. J. Prostate-Specific Antigen and Prostate Cancer: Prediction, Detection and Monitoring. *Nat. Rev. Cancer* **2008**, *8*, 268–278.

(14) Crawford, E. D.; Denes, B. S.; Ventii, K. H.; Shore, N. D. Prostate Cancer: Incorporating Genomic Biomarkers in Prostate Cancer Decisions. *Clin. Pract.* **2014**, *11*, 605–612.

(15) Hatakeyama, S.; Yoneyama, T.; Tobisawa, Y.; Ohyama, C. Recent Progress and Perspectives on Prostate Cancer Biomarkers. *Int. J. Clin. Oncol.* **2017**, *22*, 214–221.

(16) De Angelis, G.; Rittenhouse, H. G.; Mikolajczyk, S. D.; Blair Shamel, L.; Semjonow, A. Twenty Years of PSA: From Prostate Antigen to Tumor Marker. *Rev. Urol.* **2007**, *9*, 113–123.

(17) Catalona, W. J.; Partin, A. W.; Slawin, K. M.; Brawer, M. K.; Flanigan, R. C.; Patel, A.; Richie, J. P.; DeKernion, J. B.; Walsh, P. C.; Scardino, P. T.; Lange, P.H.; Subong, E.N.; Parson, R.E.; Gasior. G.H.; Loveland, K.G.; Southwick, P.C. Use of the Percentage of Free Prostate-Specific Antigen to Enhance Differentiation of Prostate Cancer from Benign Prostatic Disease: A Prospective Multicenter Clinical Trial. *J. Am. Med. Assoc.* **1998**, *279*, 1542–1547.

(18) Ceylan, C.; Gazel, E.; Kele, B.; Doluolu, Ö.; Yman, M. Can the Free/Total PSA Ratio Predict the Gleason Score before Prostate Biopsy? *Curr. Urol.* **2015**, *9*, 24–27.

(19) Benson, M. C.; Ihn Seong Whang; Pantuck, A.; Ring, K.; Kaplan, S. A.; Olsson, C. A.; Cooner, W. H. Prostate Specific Antigen Density: A Means of Distinguishing Benign Prostatic Hypertrophy and Prostate Cancer. *J. Urol.* **1992**, *147*, 815–816.

(20) Sharma, P.; Zargar-Shoshtari, K.; Pow-Sang, J. M. Biomarkers for Prostate Cancer: Present Challenges and Future Opportunities. *Future Sci. OA* **2016**, *2*, FSO72.

(21) Ferro, M.; Bruzzese, D.; Perdonà, S.; Marino, A.; Mazzarella, C.; Perruolo, G.; D'Esposito, V.; Cosimato, V.; Buonerba, C.; Di Lorenzo, G.; Musi, G.; De Cobelli, O.; Chun, F.K.; Terracciano, D. Prostate Health Index (Phi) and Prostate Cancer Antigen 3 (PCA3) Significantly Improve Prostate Cancer Detection at Initial Biopsy in a Total PSA Range of 2-10 ng/ml. *PLoS One* **2013**, *8*, 1–7.

(22) Fossati, N.; Buffi, N. M.; Haese, A.; Stephan, C.; Larcher, A.; McNicholas, T.; De La Taille, A.; Freschi, M.; Lughezzani, G.; Abrate, A.; Bini, V.; Redorta, J.P.; Graefen, M.;

Guazzoni, G.; Lazzeri, M. Preoperative Prostate-Specific Antigen Isoform P2PSA and Its Derivatives, %p2PSA and Prostate Health Index, Predict Pathologic Outcomes in Patients Undergoing Radical Prostatectomy for Prostate Cancer: Results from a Multicentric European Prospective Stud. *Eur. Urol.* **2015**, *68*, 132–138.

(23) Filella, X.; Fernández-Galan, E.; Bonifacio, R. F.; Foj, L. Emerging Biomarkers in the Diagnosis of Prostate Cancer. *Pharmgenomics. Pers. Med.* **2018**, *11*, 83–94.

(24) McDonald, M. L.; Parsons, J. K. 4-Kallikrein Test and Kallikrein Markers in Prostate Cancer Screening. *Urol. Clin. North Am.* **2016**, *43*, 39–46.

(25) Cary, K. C.; Cooperberg, M. R. Biomarkers in Prostate Cancer Surveillance and Screening: Past, Present, and Future. *Ther. Adv. Urol.* **2013**, *5*, 318–329.

(26) Cui, Y.; Cao, W.; Li, Q.; Shen, H.; Liu, C.; Deng, J.; Xu, J.; Shao, Q. Evaluation of Prostate Cancer Antigen 3 for Detecting Prostate Cancer: A Systematic Review and Meta-Analysis. *Sci. Rep.* **2016**, *6*, 2–10.

(27) Taniguchi, N.; Kizuka, Y. *Glycans and Cancer: Role of N-Glycans in Cancer Biomarker, Progression and Metastasis, and Therapeutics*, 1st Edition.; Elsevier Inc., 2015; Vol. 126.

(28) Varki, A. Biological Roles of Glycans. *Glycobiology* **2017**, *27*, 3–49.

(29) Schneider, M.; Al-Shareffi, E.; Haltiwanger, R. S. Biological Functions of Fucose in Mammals. *Glycobiology* **2017**, *27*, 601–618.

(30) Pearce, O. M. T.; Läubli, H. Sialic Acids in Cancer Biology and Immunity. *Glycobiology* **2015**, *26*, 111–128.

(31) Peracaula, R.; Tabarés, G.; Royle, L.; Harvey, D. J.; Dwek, R. A.; Rudd, P. M.; de Llorens, R. Altered Glycosylation Pattern Allows the Distinction between Prostate-Specific Antigen (PSA) from Normal and Tumor Origins. *Glycobiology* **2003**, *13*, 457–470.

(32) Llop, E.; Ferrer-Batallé, M.; Barrabés, S.; Guerrero, P. E.; Ramírez, M.; Saldova, R.; Rudd, P. M.; Aleixandre, R. N.; Comet, J.; de Llorens, R.; Peracaula, R. Improvement of Prostate Cancer Diagnosis by Detecting PSA Glycosylation-Specific Changes. *Theranostics* **2016**, *6*, 1190–1204.

(33) Yoneyama, T.; Ohyama, C.; Hatakeyama, S.; Narita, S.; Habuchi, T.; Koie, T.; Mori, K.; Hidari, K. I. P. J.; Yamaguchi, M.; Suzuki, T.; Tobisawa, Y. Measurement of Aberrant Glycosylation of Prostate Specific Antigen Can Improve Specificity in Early Detection of Prostate Cancer. *Biochem. Biophys. Res. Commun.* **2014**, *448*, 390–396.

(34) Ishikawa, T.; Yoneyama, T.; Tobisawa, Y.; Hatakeyama, S.; Kurosawa, T.; Nakamura, K.; Narita, S.; Mitsuzuka, K.; Duivenvoorden, W.; Pinthus, J. H.; Hashimoto, Y.; Koie, T.; Habuchi, T.; Arai, Y.; Ohyama, C. An Automated Micro-Total Immunoassay System for Measuring Cancer-Associated α2,3-Linked Sialyl N-Glycan-Carrying Prostate-Specific Antigen May Improve the Accuracy of Prostate Cancer Diagnosis. *Int. J. Mol. Sci.* **2017**, *18*, 470.

(35) Fukushima, K.; Satoh, T.; Baba, S.; Yamashita, K. α1,2-Fucosylated and β-N-Acetylgalactosaminylated Prostate-Specific Antigen as an Efficient Marker of Prostatic Cancer. *Glycobiology* **2010**, *20*, 452–460.

(36) Hagiwara, K.; Tobisawa, Y.; Kaya, T.; Kaneko, T.; Hatakeyama, S.; Mori, K.; Hashimoto, Y.; Koie, T.; Suda, Y.; Ohyama, C.; Yoneyama, T. *Wisteria floribunda* Agglutinin and its Reactive-Glycan-Carrying Prostate-Specific Antigen as a Novel Diagnostic and Prognostic Marker of Prostate Cancer. *Int. J. Mol. Sci.* **2017**, *18*, 261

(37) Ohyama, C.; Hosono, M.; Nitta, K.; Oh-eda, M.; Yoshikawa, K.; Habuchi, T.; Arai, Y.; Fukuda, M. Carbohydrate Structure and Differential Binding of Prostate Specific Antigen to Maackia Amurensis Lectin Between Prostate Cancer and Benign Prostate Hypertrophy. *Glycobiology* **2004**, *14*, 671-679.

(38) Etxebarria, J.; Reichardt, N. C. Methods for the Absolute Quantification of N-Glycan Biomarkers. *Biochim. Biophys. Acta - Gen. Subj.* **2016**, *1860*, 1676–1687.

(39) Tajiri, M.; Ohyama, C.; Wada, Y. Oligosaccharide Profiles of the Prostate Specific Antigen in Free and Complexed Forms from the Prostate Cancer Patient Serum and in Seminal Plasma: A Glycopeptide Approach. *Glycobiology* **2008**, *18*, 2-8.

(40) Haga, Y.; Uemura, M.; Baba, S.; Inamura, K.; Takeuchi, K.; Nonomura, N.; Ueda, K. Identification of Multisialylated LacdiNAc Structures as Highly Prostate Cancer Specific Glycan Signatures on PSA. *Anal. Chem.* **2019**, *91*, 2247–2254.

(41) Wohlschlager, T.; Scheffler, K.; Forstenlehner, I.C.; Skala, W.; Senn, S.; Damoc, E.; Holzmann, J.; Huber, C.G. Native Mass Spectrometry Combined with Enzymatic Dissection Unravels Glycoform Heterogeneity of Biopharmaceuticals. *Nat. Commu.* **2018**, *9*, 1713.

(42) Banazadeh, A.; Veillon, L.; Wooding, K.M.; Zabet-moghaddam, M.; Mechref, Y. Recent

Advances in Mass Spectrometric Analysis of Glycoproteins. *Electrophoresis* **2017**, *38*, 162-189.

(43) Li, Z.; Kitov, P. I.; Han, L.; Kitova, E. N.; Mozenah, F.; Rodrigues, E.; Chapla, D. G.; Moremen, K. W.; Macauley, M. S.; Klassen, J. S. CUPRA-ZYME: An Assay for Measuring Carbohydrate-Active Enzyme Activities, Pathways, and Substrate Specificities. *Anal. Chem.*, **2020**, *92*, 3228-3236.

(44) Gerber, S.A.; Scott, C.R.; Turecek, F.; Gelb, M.H. Analysis of Rates of Multiple Enzymes in Cell Lysates by Electrospray Ionization Mass Spectrometry. *J. Am. Chem. Soc.*, **1999**, *121*, 1102-1103.

(45) Moremen, K.W.; Ramiah, A.; Stuart, M.; Steel, J.; Meng, L.; Forouhar, F.; Moniz, H.A.; Gahlay, G.; Gao, Z.; Chapla, D.; Wang, S.; Yang, J.-Y.; Prabhakar, P.K.; Johnson, R.; Dela Rosa, M.; Geisler, C.; Nairn, A.V.; Seetharaman, J.; Wu, S.-C.; Tong, L.; Gilbert, H.J.; LaBaer, J.; Jarvis, D.L. Expression System for Structural and Functional Studies of Human Glycosylation Enzymes. *Nat. Chem. Biol.*, **2018**, *14*, 156-162.

(46) Meng, L.; Forouhar, F.; Thieker, D.; Gao, Z.; Ramiah, A.; Moniz, H.; Xiang, Y.; Seetharaman, J.; Milaninia, S.; Su, M.; Bridger, R.; Veillon, L.; Azadi, P.; Kornhaber, G.; Wells, L.; Montelione, G.T.; Woods, R.J.; Tong, L.; Moremen, K.W. Enzymatic Basis for N-glycan Sialylation: Structure of Rat α2,6-sialyltransferase (ST6Gal1) Reveals Conserved and Unique Features for Glycan Sialylation. *J. Biol. Chem.*, **2013**, *288*, 34680-34698.

(47) Kitov, P. I.; Han, L.; Kitova, E. N.; Klassen, J. S. Sliding Window Adduct Removal Method (SWARM) for Enhanced Electrospray Ionization Mass Spectrometry Binding Data. *J. Am. Soc. Mass Spectrom*, **2019**, *30*, 1446–1454.

(48) Ceroni, A.; Dell, A.; Haslam, S.M. The GlycanBuilder: A Fast, Intuitive and Flexible Software Tool for Building and Displaying Glycan Structures. *Source Code for Biology and Medicine*. **2007**, *2*, 3.

(49) Gut, H.; King, S. J.; Walsh, M. A. Structural and Functional Studies of Streptococcus Pneumoniae Neuraminidase B: An Intramolecular Trans-Sialidase. *FEBS Lett.* **2008**, *582*, 3348–3352.

(50) Luo, Y.; Li, S.C.; Li, Y.T. Luo, M. The 1.8 A° Structures of Leech Intramolecular Trans-Sialidase Complexes: Evidence of its Enzymatic Mechanism. A. *J. Mol. Biol.* **1999**, *285*,

323-332.

(51) Sarrats, A.; Saldova, R.; Comet, J.; O'Donoghue, N.; de Llorens, R.; Rudd, P.M.; Peracaula, R. Glycan Characterization of PSA 2-DE Subforms from Serum and Seminal Plasma. *OMICS*, **2010**, *14*, 465-474.

(52) Anguizola, J.; Matsuda, R.; Barnaby, O.S.; Joseph, K.S.; Wa, C.; DeBolt, E.; Koke, M.; Hage, D.S. Review: Glycation of Human Serum Albumin. *Clinica Chimica Acta*. **2013**, *0*, 64-76.

(53) Tabarés, G.; Jung, K.; Reiche, J.; Stephan, C.; Lein, M.; Peracaula, R.; de Llorens, R.; Hoesel, W. Free PSA Forms in Prostatic Tissue and Sera of Prostate Cancer Patients: Analysis by 2-DE and Western Blotting of Immunopurified Samples. *Clinical Biochemistry*. **2007**, *40*, 343-350.